A tomographic approach to the statistical analysis of the large-scale structure of the Universe.

Salvador Salazar Albornoz

München 2016

A tomographic approach to the statistical analysis of the large-scale structure of the Universe.

Salvador Salazar Albornoz

Dissertation
an der Fakultät für Physik
der Ludwig–Maximilians–Universität
München

vorgelegt von
Salvador Salazar Albornoz
aus Santiago, Chile

München, den 14. März 2016

Erstgutachter: Prof. Dr. Ralf Bender

Zweitgutachter: Prof. Dr. Jochen Weller

Tag der mündlichen Prüfung: Mittwoch den 13. April 2016

To Tatiana, Javiera, and those to come....

Zusammenfassung

Beobachtungen der großskaligen Struktur des Universums, die auf einer statistischen Analyse der Galaxienverteilung, einer sogenannten Clustering-Analyse, in großen Himmelsdurchmusterungen beruhen, haben sich zu einer wichtigen Wissensquelle für unser Verständnis des Universums entwickelt. Dazu gehören zum Beispiel die Messung der Zweipunkt-Korrelationsfunktion (2PKF) oder des Leistungsdichtespektrums von Galaxien. Herkömmliche Messungen dieser Art sind jedoch mit den folgenden Herausforderungen verbunden: Erstens muss man ein bestimmtes kosmologisches Referenzmodell annehmen, um die dreidimensionalen Galaxienpositionen verwenden zu können. Zweitens mittelt man meist über ein großes kosmologisches Volumen, das sich über einen weiten Rotverschiebungsbereich erstreckt. Dabei wird die Abhängigkeit des Clustering-Signals von der Rotverschiebung vernachlässigt. In dieser Arbeit stellen wir eine alternative Herangehensweise vor, welche die genannten Schwierigkeiten umgeht.

Ziel dieser Dissertation ist die kosmologische Auswertung der Galaxienverteilung anhand eines tomographischen Ansatzes, der die winkelabhängige 2PKF, $\omega(\theta)$, in dünnen Rotverschiebungsschalen misst. Ein Vorteil gegenüber bisherigen Analyseverfahren ist, dass keine Referenzkosmologie benötigt wird, um die gemessenen Winkelpositionen und Rotverschiebungen der Galaxien in räumliche Abstände umzurechnen. Des Weiteren führt man im Gegensatz zu den herkömmlichen Methoden nicht nur eine einzige gemittelte Messung für die effektive Rotverschiebung des Galaxienkatalogs durch. Dadurch kann man untersuchen, wie sich das Clustering-Signal mit der Rotverschiebung entwickelt, wodurch die Expansionsgeschichte des Universums genauer bestimmt wird.

Wir modellieren das gemessene $\omega(\theta)$ in den verschiedenen Rotverschiebungsschalen sowie die dazugehörige Kovarianzmatrix und überprüfen diese Modellierungen anhand von synthetischen Galaxienkatalogen. Im Rahmen dieser Untersuchung zeigen wir, dass mit Hilfe der tomographischen Methode die kosmologischen Parameter unverfälscht extrahiert werden. Außerdem entwickeln wir eine Vorhersage für die Genauigkeit der Ergebnisse, die wir für die Analyse des finalen Galaxienkatalogs des Baryon Acoustic Oscillation Survey (BOSS) erwarten. Diese Vorhersage basiert auf Messdaten, die wir unter der Annahme eines Referenzmodells simulieren, das an die

Beobachtungen des kosmischen Mikrowellenhintergrunds (MWH) durch die Planck-Mission angepasst wurde. Für eine engere Einschränkung des kosmologischen Parameterraums kombinieren wir die BOSS-Analyse mit den Planck-Messungen. Wir untersuchen unsere Methode sowohl in Bezug auf das kosmologische Standardmodell (ΛCDM-Modell) als auch auf zwei mögliche Erweiterungen mit alternativen Modellen für die Dunkle Energie (DE). Dazu vergleichen wir unsere Ergebnisse mit denen, die man aus der isotropischen Messung der Baryonischen Akustischen Oszillationen (BAO) für den BOSS-Galaxienkatalog unter Verwendung der Rekonstruktions-Methode in Kombination mit Planck-Daten erhält. Für das ΛCDM-Modell können die kosmologischen Parameter mit dieser herkömmlichen BAO-Analyse genauer eingeschränkt werden. Wenn wir allerdings erlauben, dass der Zustandsgleichungsparameter der DE, w_{DE}, vom Wert -1 abweicht, kann die tomographische Analyse zu besseren Ergebnissen führen. Unter der Annahme, dass w_{DE} konstant ist, weisen beide Analysen eine vergleichbare Genauigkeit auf. Für ein zeitlich veränderliches w_{DE} erreicht man mit dem tomographischen Verfahren eine Verbesserung des Gütefaktors (Figure of Merit; FoM) in der w_0–w_a-Ebene von bis zu 15%.

Im letzten Teil der Arbeit wenden wir die tomographische Methode auf den finalen BOSS-DR12-Galaxienkatalog an. Dafür benutzen wir neuartige Ansätze zur Modellierung der nichtlinearen Gravitationsdynamik, des Galaxien-Bias und der Verzerrungen im Rotverschiebungsraum. Außerdem erweitern wir unsere Analyse dahingehend, dass sie neben den Auto- auch die Kreuzkorrelationen der unterschiedlichen Rotverschiebungsschalen beinhaltet. Ein wichtiger Schritt ist dabei, die optimale Anzahl an Rotverschiebungsschalen zu bestimmen, um eine möglichst hohe Genauigkeit für die FoM in der Ω_m–w_{DE}-Ebene zu erzielen. Anhand unserer Ergebnisse analysieren wir die Rotverschiebungs-Abhängigkeit des linearen Bias der BOSS-Galaxien. Diese Untersuchung ist mit herkömmlichen Galaxien-Clustering-Methoden nicht möglich. Außerdem bestimmen wir Einschränkungen für kosmologische Parameter, die sich aus unserer Analyse in Kombination mit Messungen des MWH und Typ-Ia-Supernova-Daten (SNIa) ergeben. Dazu betrachten wir neben dem ΛCDM-Modell eine Auswahl seiner interessantesten Erweiterungen. Zu diesen zählen Abweichungen von $w_{DE} = -1$, Neutrinos mit nicht-minimaler Masse, räumliche Krümmung und Modifizierungen der Allgemeinen Relativitätstheorie, welche durch den Wachstumsindex γ parametrisiert sind. Unsere Ergebnisse sind vergleichbar mit anderen aktuellen hochpräzisen Messungen der kosmologischen Parameter und stimmen sehr gut mit dem ΛCDM-Modell überein. Insbesondere erhalten wir für die Kombination aus $\omega(\theta)$, CMB- und SNIa-Daten einen Wert für w_{DE}, der im Einklang mit -1 ist. Die Genauigkeit der Messung ist für ein zeitlich konstantes w_{DE} besser als 5% und für ein Modell, das ein räumlich gekrümmtes Universum zulässt, besser als 6%.

Abstract

Observations of the large-scale structure of the Universe based on statistical analyses of galaxy clustering in large galaxy-surveys, such as measurements of the the correlation function or the power spectrum, have been of great importance to the advancement of our understanding of the Universe. Nevertheless, these measurements have two issues. First, they need to assume a fiducial cosmology in order to use the 3D positions of galaxies. Secondly, they usually average large cosmological volumes neglecting the redshift evolution of the galaxy-clustering signal. Here we present an alternative approach, which is able to overcome these issues.

We test the cosmological implications of studying galaxy clustering using a tomographic approach, by computing the galaxy two-point angular correlation function $\omega(\theta)$ in thin redshift shells using a spectroscopic-redshift galaxy survey. An advantage of this procedure, compared to the traditional 3D analysis, is that it is not necessary to assume a fiducial cosmology in order to transform measured angular positions and redshifts into distances. Another advantage is that it allows us to probe the redshift evolution of the galaxy clustering signal, instead of making only one measurement at the effective average redshift of the sample, which results in better constraints on the expansion history of the Universe.

We model the signal of $\omega(\theta)$ in redshift bins, and its covariance matrix, and test these models against a set of mock galaxy catalogues. We show that this technique is able to extract unbiased cosmological constraints. Also, assuming the best-fitting ΛCDM cosmology from the cosmic microwave background (CMB) measurements from the *Planck* satellite, we forecast the expected accuracy of applying this tomographic approach to constrain cosmological parameters, using the final Baryon Oscillation Spectroscopic Survey (BOSS) catalogue in combination with Planck. We show tests of the standard ΛCDM model and two extensions of alternative dark energy models. We compare these results with those expected from isotropic baryon acoustic oscillation (BAO) measurements post-reconstruction on the same galaxy catalogue combined with Planck. The standard BAO analysis is more accurate for constraining cosmo-

logical parameters for the basic ΛCDM model. Nevertheless, the tomographic technique gives better results when we allow the dark energy equation-of-state parameter, w_{DE}, to deviate from -1, resulting in a performance similar to BAOs in the case of a constant value of w_{DE}, and an improvement in the case of a time-dependent w_{DE}, increasing the value of the Figure-of-Merit (FoM) in the $w_0 - w_a$ plane by up to 15%.

Afterwards, using state-of-the-art modelling of non-linearities, bias and RSD, as well as extending the analysis to include both auto- and cross-correlation functions between redshift shells, we apply this tomographic analysis to the final BOSS DR12 galaxy sample. For this, we optimise the number of redshift shells in order to maximise the value of the FoM in the $\Omega_{\mathrm{m}} - w_{\mathrm{DE}}$ plane. We present results on the redshift evolution of the linear bias of BOSS galaxies, which cannot be obtained with traditional methods for galaxy-clustering analysis. We also obtain constraints on cosmological parameters, combining this tomographic analysis with measurements of the CMB and type Ia supernova (SNIa). We explore a number of cosmological models, including the standard ΛCDM model and its most interesting extensions, such as deviations from $w_{\mathrm{DE}} = -1$, non-minimal neutrino masses, spatial curvature and deviations from general relativity using the growth-index γ parametrisation. These results are, in general, comparable to the most precise present-day constraints on cosmological parameters, and show very good agreement with the standard model. In particular, combining CMB, $\omega(\theta)$ and SNIa, we find a value of w_{DE} consistent with -1 to a precision better than 5% when it is assumed to be constant in time, and better than 6% when we also allow for a spatially-curved Universe.

Contents

List of Figures

List of Tables

Chapter 1

Introduction

During the last century, cosmology went from a more philosophical discipline to a well established research field in physics and astronomy, today referred to as *physical cosmology*. This was supported by Albert Einstein's theory of General Relativity (Einstein, 1916) , and by key observations such as the recession of distant galaxies by Edwin Hubble (Hubble, 1929) which, assuming the cosmological principle (i.e. the Universe is homogeneous and isotropic), suggested the Universe was expanding. From the observational side though, the greatest breakthrough came years later in the second half of the 20th century. First, the discovery of the Cosmic Microwave Background (CMB) in 1964 by Arno Penzias and Robert Wilson (Penzias and Wilson, 1965), provided strong evidence in favour of the Big Bang theory, showing that the Universe must have been very hot and dense in its early stages, cooling down as it expands. Secondly, in 1998 the *Supernova Cosmology Project*(Perlmutter et al., 1998) and the *High-Z Supernova Search Team*(Riess et al., 1998) used supernovae type Ia (SNIa) up to redshift $z \lesssim 0.9$ as distance estimators (standard candles), finding that the Universe is not only expanding, but this expansion is accelerating. This marked the beginning of what today is referred to as *the age of precision cosmology*, a very active data-driven research field that studies the origin, structure and evolution of the Universe.

Besides the CMB and SNIa, a third key component in observational cosmology, which this worked is based on, are redshift surveys: large 3D maps of the large-scale structure (LSS) of the Universe traced by galaxies. Even though the firsts redshift surveys date from the early '80s, such as the CfA Redshift survey (Huchra et al., 1983), given the technological limitations at the time, it was not possible to measure more than a handful of galaxy spectra at the same time in order to obtain redshifts. This inefficiency limited the total volume of such galaxy surveys and therefore the amount of available information for cosmological studies. This changed in the '90s, when multi-

object spectroscopy techniques were developed allowing the measurement of the spectra of hundreds of galaxies per night, rapidly increasing the volume of these redshift surveys, finally unveiling the large-scale structure of the Universe at the present. The two most important examples of this new generation of galaxy redshift surveys that arose in the early 2000s, are the Sloan Digital Sky Survey (SDSS; York et al., 2000) and the 2dF Galaxy Redshift Survey (2dFGRS; Colless et al., 2001, 2003).

All of these observations and experiments set what today is known as the *standard cosmological model*, in which at very early stages the Universe was extremely hot and dense, then went through an epoch of exponential inflation that lasted a fraction of a second. After this, the Universe has been expanding at a less rapid rate, decelerating at first, and recently accelerating. This model also states that the energy budget of the universe today is largely dominated by a *dark energy* component, that makes up to about 70% of its total energy density, and drives this accelerated expansion as a mysterious repulsive force that only affects space-time, without interacting with other components. The other 30% of today's energy density budget is mostly matter, from which only about 16% ($\sim 5\%$ of the total) is in the form of known *baryonic matter*, and the rest corresponds to another *dark* component called *dark matter*, that only interacts gravitationally with other constituents, whose presence we can only infer through these interactions with baryons and light. Other components, such as photons and neutrinos, constitute a very small fraction of the total energy density of the Universe today, but where dominant at early stages of its evolution. The nature of dark energy, dark matter, and the expansion history of the Universe are the most fundamental questions cosmologists want to answer.

Observations of the CMB show that the Universe was extremely homogeneous and isotropic at early stages, with tiny fluctuations (inhomogeneities) that in the CMB appear as temperature fluctuations of the order $\delta T/T \approx 10^{-5}$. On the other hand, galaxy surveys show that today the Universe is very clumpy, formed by galaxies and clusters of galaxies, which form larger structures such as filaments, walls, and large voids. In order to explain these observations, the standard model states that these inhomogeneities arise from quantum fluctuations created in the very early Universe, that get "stretched" during inflation to scales where they are no longer in the quantum regime, and thus remain. These fluctuations are very small at the beginning, but with time, the matter density field (and hence the velocity field) starts evolving under the gravitational force induced by high-density regions, slowly collapsing into these potential minima and ultimately forming the large-scale structure we see today. Studying how these structures form and evolve in an expanding

Universe provides plenty of valuable information on the constituents and the expansion history of the Universe.

One of the most important cosmological probes of LSS is the signal of the baryon acoustic oscillations (BAO). These oscillations occurred because small primordial perturbations induced sound waves in the relativistic plasma of the early Universe (Peebles and Yu, 1970), but later on at the epoch of recombination ($z \approx 1000$), the sound speed suddenly decreased to the point that these waves stopped propagating. Since the Universe has a non-negligible fraction of baryons, cosmological theories predict that the BAO signal will also be imprinted onto the two-point statistics of the non-relativistic matter as an excess of clustering in the correlation function, or an oscillation in power in the power spectrum, at a given (fixed) scale, making it an ideal standard ruler that can be measured at different redshifts.

In 1999, motivated by the results obtained from COBE of the primary temperature anisotropy in the CMB (Bennett et al., 1996), the BAO signal was measured for the first time in the CMB, detecting the small angle anisotropies in the CMB angular power spectrum, confirming the cosmological predictions (Torbet et al. 1999; Miller et al. 1999). Later on in 2005, the BAO signal was measured simultaneously in the SDSS by Eisenstein et al. (2005) using the spatial correlation function of a spectroscopic subsample of luminous red galaxies (LRGs), finding the BAO peak at $r \approx 100$ h^{-1}Mpc; and in the 2dFGRS, where Cole et al. (2005) also found the BAO signal using the power spectrum. Supported by the increasing amount of data from current and future large galaxy-surveys, such as the Baryon Oscillation Spectroscopic Survey (BOSS; Dawson et al., 2013), WiggleZ (Drinkwater et al., 2010), the Dark Energy Survey (DES; The Dark Energy Survey Collaboration, 2005), the Hobby-Eberly Telescope Dark Energy Experiment (HETDEX; Hill et al., 2008), the Dark Energy Spectroscopic Instrument (DESI; Levi et al., 2013), the Large Synoptic Survey Telescope (LSST; LSST Science Collaboration et al., 2009) and the *Euclid* mission (Laureijs et al., 2011), substantial work has been devoted to modelling and detecting the BAO signal in two-point statistics and use it for cosmological constraints (e.g. Hütsi 2006; Percival et al. 2007; Spergel et al. 2007; Reid et al. 2010; Blake et al. 2011; Sánchez et al. 2009, 2013, 2014; Samushia et al. 2013; Anderson et al. 2014b).

There are two important issues related to the traditional study of LSS that need to be considered. First, in order to use the 3D positions of galaxies, it is necessary to assume a fiducial cosmological model in order to transform the measured angular positions on the sky and redshifts of galaxies into co-moving coordinates or distances, a process which could bias the parameter constraints if not treated carefully (see e.g. Eisenstein et al. 2005 and Sánchez

et al. 2009). Secondly, in order to obtain a precise measurement of either the correlation function or the power spectrum, usually the whole galaxy sample is used to obtain one measurement, typically averaging over a wide redshift range and assuming that the measurement at the mean redshift is representative of the entire sample, washing out information on the redshift evolution of the structures. Even when these two issues are well understood and under control within certain conditions, a simple way to avoid them is to use two-point statistics based only on direct observables, i.e. only angular positions and/or redshifts, such as the angular correlation function $\omega(\theta)$ or the angular power spectrum C_ℓ. This is done by dividing the sample into redshift bins, or shells, in order to recover information along the line of sight, which otherwise would be lost due to projection effects.

This thesis is based on this idea. In chapter 2 we start by presenting the background and the tools required for the statistical analysis of the large-scale structure of the Universe, including the theoretical models we use for the analysis of the galaxy clustering measurements and observational effects that need to be taken into account for their correct analysis. In chapter 3 we introduce what we call the *clustering tomography* technique, where we model the angular galaxy clustering signal in thin redshift bins, show what is the information they provide, and test its cosmological implications. In chapter 4, we proceed to analyse the final BOSS galaxy sample, explore the evolution of the galaxy bias of this sample, and obtain constraints on different cosmological models combining this clustering tomography technique with the latest measurements of the CMB and SNIa available. Final conclusions are in chapter 5. Appendix A provides an overview of the mathematical formalism behind the statistical tools we use. Finally, appendix B contains the summary tables from chapter 4, including those of the cosmological parameters explored, that have been removed from the body of this work for readability.

Chapter 2

Inhomogeneities in an Expanding Universe

Since we are interested in the regime where matter is pressure-less and non-relativistic, and the relevant scales are much less than the curvature radius of the Universe, it is possible to describe the dynamics of the matter density fluctuations using Eulerian hydrodynamics and Newtonian gravity. Let us start by defining the matter density contrast field as the fractional difference with respect to the mean density $\langle \rho \rangle = \bar{\rho}$,

$$\delta(\mathbf{x}, t) = \frac{\rho(\mathbf{x}, t) - \bar{\rho}(t)}{\bar{\rho}(t)}, \tag{2.1}$$

where the position and time dependence is shown explicitly here, but for simplicity we will drop it hereafter. The equations governing the dynamics of this density contrast field in an expanding Universe are, the mass conservation equation

$$\frac{\partial \delta}{\partial t} + \frac{1}{a} \nabla \cdot [(1 + \delta)\mathbf{v}] = 0, \tag{2.2}$$

the momentum conservation equation

$$\frac{\partial \mathbf{v}}{\partial t} + \frac{1}{a}(\mathbf{v} \cdot \nabla)\mathbf{v} + H\mathbf{v} = -\frac{1}{a}\nabla\Phi, \tag{2.3}$$

and the Poisson equation

$$\nabla^2 \Phi = 4\pi G a^2 \bar{\rho}\delta; \tag{2.4}$$

where a is the scale factor that gives the relative expansion of the Universe as a function of time, $H \equiv \dot{a}/a$ is the Hubble function, which has units of velocity over distance (usually km s^{-1}Mpc^{-1}), $\mathbf{v}$ and Φ are respectively the (peculiar) velocity and gravitational fields associated with δ, and G is the gravitational constant.

2.1   The Linear regime

In general, this system of equations is impossible to solve analytically, but if we restrict the analysis to the regime where $\delta \ll 1$ and $|\mathbf{v}| \ll 1$, the mass and momentum conservation equations can be linearised as

$$\frac{\partial \delta}{\partial t} + \frac{1}{a}\nabla \cdot \mathbf{v} = 0, \tag{2.5}$$

$$\frac{\partial \mathbf{v}}{\partial t} + H\mathbf{v} = -\frac{1}{a}\nabla \Phi. \tag{2.6}$$

Taking the time derivative of the first equation, the divergence of the second, and combining them along with (2.4), we obtain a second-order differential equation that, considering the gravitational force in the linear regime acting only locally (thus making the whole equation local), can be turned into a second-order ordinary differential equation given by

$$\ddot{\delta} + 2H\dot{\delta} = 4\pi G\bar{\rho}\delta, \tag{2.7}$$

which describes the evolution of density fluctuations that *grow in place*. The solutions of this equation can be written as

$$\delta(\mathbf{x}, t) = A(\mathbf{x})D_+(t) + B(\mathbf{x})D_-(t), \tag{2.8}$$

where $D_+(t)$ and $D_-(t)$ are usually referred as the growing and decaying modes, respectively.

In practice, given that the initial perturbations are small, and that at early times the expansion of the Universe slows down the gravitational growth of density fluctuations, this linear approximation works well up until late times, specially for large scales.

2.2   Statistics of the matter density field

The matter density field can be thought of as a random field, which means that it is possible to learn from it by applying statistical tools for such purposes. Traditionally, this has been done through two-point statistics (the second-order central moments), such as the **correlation function** $\xi(r)$ in configuration space, and the **power spectrum** $P(k)$ in Fourier space.

The correlation function can be defined as the excess probability density of finding a pair of objects separated by a distance r, with respect to that of a homogeneous random distribution. That is, given two volume elements, dV_1

and dV_2, separated by r, the probability (density) of finding an object in each of these volume elements is given by

$$dP_{1,2} = \bar{\rho}(1 + \xi(r))dV_1 dV_2, \qquad (2.9)$$

where $\bar{\rho}$ is the mean density of such objects in the field. Here, we have assumed that the random field under study is homogeneous and isotropic, and for this reason $\xi(r)$ is only a function of the magnitude of the separation vector $\mathbf{r}$. An equivalent definition, considering a zero-mean random field (such as the density contrast δ), is given by

$$\xi(r) \equiv \langle \delta(x)\delta(x + r)\rangle, \qquad (2.10)$$

where $\langle\cdot\rangle$ stands for the expected value.

Similarly, in two dimensions we can define the **angular correlation function**, $\omega(\theta)$, as the excess probability density of finding and object in two different solid-angle elements $d\Omega_1$ and $d\Omega_2$, separated by an angular separation θ, i.e.

$$dP_{1,2} = \bar{n}(1 + \omega(\theta))d\Omega_1 d\Omega_2, \qquad (2.11)$$

where in this case $\bar{n}$ is the projected mean density.

The power spectrum is defined as

$$\langle \delta(k)\delta^*(k')\rangle \equiv (2\pi)^3 P(k)\delta_D(k - k'), \qquad (2.12)$$

where δ_D is the Dirac delta function and, again, assuming homogeneity and isotropy implies that $P(k)$ is only a function of the magnitude of the wave-vector $\mathbf{k}$. The power spectrum is the Fourier pair of the correlation function, thus it can also be defined in terms of ξ as

$$\xi(r) = 4\pi \int_0^\infty \frac{k^2 dk}{(2\pi)^3} \ P(k)\frac{\sin(kr)}{kr}. \qquad (2.13)$$

Both, the correlation function and the power spectrum, have shown to be excellent tools for the analysis of the large-scale structure of the Universe, as a measure of the clustering of galaxies. In the following, we will concentrate on how to model this clustering signal in terms of the matter and galaxy density fields. A more detailed description of the statistical tools defined above, as well as an overview of the mathematical formalism behind them, can be found in appendix A.

2.3   The linear power spectrum

Since the matter density field is expected to be a real-valued homogeneous and isotropic (Gaussian) random field, the density contrast is a **real-valued, zero-mean, homogeneous and isotropic** random field. From the statistical point of view, this implies that we can apply the spectral representation theorem (see appendix A) to the field $\delta(\mathbf{x})$, where its Fourier pair $\tilde{\delta}(\mathbf{k})$ is an independent (i.e. uncorrelated) random variable; and that its correlation function, and the associated power spectrum, are respectively functions of the magnitudes r and k only. It is important to bear in mind that the Gaussianity condition is only true in the linear regime, but at late times gravitational interactions make the density field (thus, the velocity and gravitational fields as well) non-Gaussian.

Since (in the linear regime) the Fourier components of the density contrast field are independent, it is easier to work with them and study their evolution. For this purpose, the power spectrum is the standard tool used to characterise the statistical properties of the density contrast, which we will describe here, by its different components.

2.3.1   The primordial power spectrum

Standard models of (inflationary) cosmology predict that the initial power spectrum of perturbations is a nearly scale-invariant power-law function of the wavenumber

$$\mathcal{P}(k) \propto k^{n_\mathrm{s}}, \tag{2.14}$$

where n_s is known as the spectral index. Most models of inflation predict n_s between 0.9 and 1. A value of $n_\mathrm{s} = 1$ corresponds to a perfectly scale-invariant power spectrum, also known as the Harrison-Zeldovich spectrum, and for any value different from $n_\mathrm{s} = 1$ the spectrum is said to be *tilted*. Based on present-day CMB measurements from the Planck satellite (Planck Collaboration XIII, 2015), the value of the spectral index is constrained to $n_\mathrm{s} \approx 0.96$, with $n_\mathrm{s} = 1$ disfavoured by a significance of $> 5\sigma$ (assuming that n_s is scale-invariant).

2.3.2   The transfer function

This primordial power spectrum, however, is not observable. The reason is that the initial fluctuations are affected by interactions between the different energy components of the Universe. The way in which the power spectrum at different scales (or k-modes) is influenced by this interactions depends on when these scales re-enter (after inflation) the Hubble horizon. In the linear regime, the Fourier components of the density contrast evolve independently,

and if we assume that they appear at some very early time t_i, we can neglect the decaying mode $D_-(t)$ in equation (2.8) and write their time evolution as

$$\tilde{\delta}(k,t) = \frac{D(t)}{D(t_i)} T(k) \tilde{\delta}(k, t_i),$$ (2.15)

where $D(t) \equiv D_+(t)$ from equation (2.8), and $T(k)$ is the transfer function, which describes how the different Fourier modes grow as they re-enter the horizon, considering the interaction between different constituents of the Universe. The exact computation of the transfer function is a complicated task involving the integration of the Boltzmann equation for the various interactions. Approximate fitting formulas for the transfer function were proposed by Bond and Efstathiou (1984) and Eisenstein and Hu (1999), but they are not accurate enough for present-day clustering analyses. Nevertheless, today a few fast and accurate *Boltzmann codes* are publicly available, such as CAMB (Lewis et al., 2000) and CLASS (Blas et al., 2011), which compute the transfer function numerically in a few seconds with extremely high precision.

Taking the expression in (2.15) to compute the power spectrum as in equation (2.12), and considering that $\langle \tilde{\delta}(k,t_i)\tilde{\delta}^*(k,t_i)\rangle = \mathcal{P}(k)$ given in equation (2.14), the time-dependent linear (matter) power spectrum can be obtained as,

$$P_{\mathrm{L}}(k,t) = \left(\frac{D(t)}{D(t_i)}\right)^2 T^2(k)\mathcal{P}(k).$$ (2.16)

If we replace $\mathcal{P}(k)$ for k^{n_s} as in (2.14), we still need a constant of proportionality, or normalisation. In practice this normalisation is determined from observations, with respect to a pivot value k_0, and is usually called the spectral amplitude A_s. With this, the final expression for the linear power spectrum is given by

$$P_{\mathrm{L}}(k,t) = \left(\frac{D(t)}{D(t_i)}\right)^2 T^2(k) A_s \left(\frac{k}{k_0}\right)^{n_s}.$$ (2.17)

2.4   Baryon acoustic oscillations

So far, we have considered matter as a single component, but in fact, the matter content of the Universe is given by *normal* baryonic matter and another (unknown, non-baryonic) *dark matter* component. This has a critical consequence for the shape of the matter power spectrum (and, of course, $\xi(r)$), because, unlike dark matter (in standard cosmological models), baryons interact with photons.
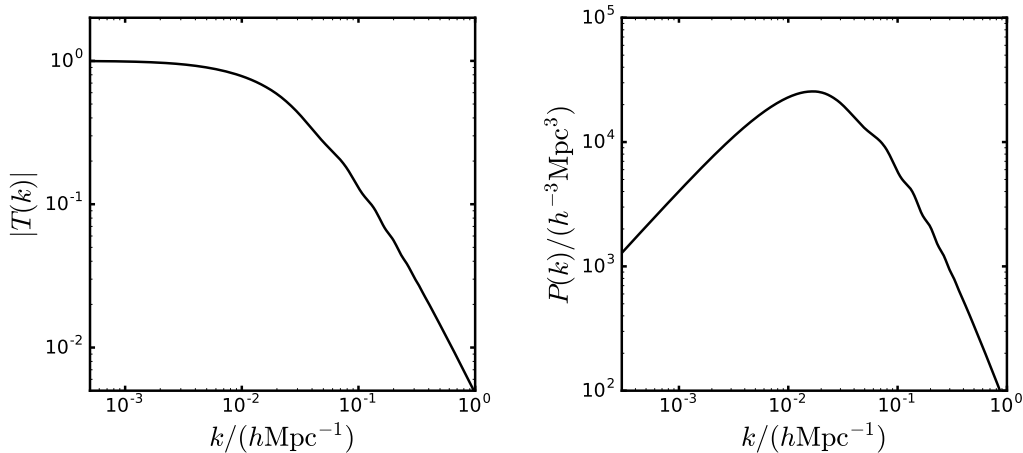
Figure 2.1: *Left panel*: The absolute value of the normalised transfer function. *Right panel*: Linear matter power spectrum. Both have been computed using CAMB, assuming the best-fitting ΛCDM model to the CMB temperature fluctuation power spectrum measured by the Planck satellite. The baryon acoustic oscillations (BAO) can be seen around $k \sim 10^{-1}h/$Mpc in both panels.

Before recombination, when the Universe was very hot ($T > 3000$K), baryons and photons were tightly coupled in a so called baryon-photon plasma, where electrons interact with photons via Thomson scattering, and with protons and Helium nuclei by Coulomb interaction. Even though dark matter only interacts with photons and baryons through gravity, its role is to be the largest contributor to the gravitational potential. In one moment in this hot primordial soup, baryons try to collapse towards the gravitational potential minima, and this force is equilibrated by an increase in radiation pressure by photons. The result of this opposing forces creates a spherical density wave (or sound wave) that travels outwards from the density peaks, until the moment that the Universe is cold enough ($T \lesssim 3000$K) for the electrons to combine with protons and He nuclei. This ceases the coupling of baryons and photons, finally stopping the propagation of this density wave (considering matter being pressure-less), leaving an excess of clustering at the scale of the sound horizon.

To illustrate this, it is possible to show that taking the Fourier equivalent of the linearised equations for perturbations (2.5), (2.6) and (2.4) in terms $\tilde{\delta}(k)$ for each component (dark matter, baryons and photons), and assuming that the coupling between baryons and photons is very efficient, thus $\mathbf{v}_b \approx \mathbf{v}_\gamma$, one can obtain an equation for the evolution of baryon fluctuations given by

$$\ddot{\delta}_b + H\frac{1+2R}{1+R}\dot{\delta}_b + \frac{1}{3(1+R)}\frac{k^2}{a^2}\delta_\gamma = \frac{k^2}{a^2}\Phi, \qquad (2.18)$$

where we have dropped the $\tilde{}$ symbol for simplicity, and $R \equiv \frac{3\bar{\rho}_{\mathrm{b}}}{4\bar{\rho}_\gamma}$ is the baryon-to-photon energy density ratio. This is a wave-like equation, whose oscillatory solution is know as the **baryon acoustic oscillations** (BAO) and has a frequency of kr_{s}, where r_{s} is the **sound horizon**

$$r_{\mathrm{s}}(t) = \int_0^t dt \frac{c_{\mathrm{s}}(a)}{a}, \qquad (2.19)$$

and c_{s} is the sound speed that, before decoupling, has a value of $c_{\mathrm{s}}^2 = \frac{c}{3(1+R)}$. The moment in time at which this sound wave stops is known as the *drag* time, t_{d}, or the *drag* redshift, z_{d}, when dealing with observations. Figure 2.1 shows how these wiggles look like in the transfer function (left-hand side) and in the linear matter power spectrum (right-hand side), for the best-fitting Λ cold dark matter (CDM) model to the CMB temperature fluctuations power spectrum measured by the Planck satellite. It can be seen that these oscillations are small. This is because after decoupling baryons fall back to the dark matter density peaks, but dark matter also follows baryons without erasing the oscillations completely. This means that, on one hand if there were no dark matter, these wiggles would be much stronger; and on the other hand, the amplitude of the oscillations encodes information of the baryon fraction.

This result is of great importance, because the sound horizon scale imprinted onto two-point statistics can be used as a standard ruler. Thus, measuring the BAO scale at different epochs, it is possible to obtain accurate constraints on the expansion history of the Universe. If we know the sound horizon scale $r_{\mathrm{s}}(z_{\mathrm{d}})$, and we measure the apparent size of the BAO scale at a given redshift, along and perpendicular to the line of sight, we can relate this to the angular diameter distance, $D_{\mathrm{A}}(z)$, and the Hubble parameter, $H(z)$, as

$$\Delta\theta_{\mathrm{BAO}} = \frac{r_{\mathrm{s}}}{(1+z)D_{\mathrm{A}}(z)}, \qquad (2.20)$$

$$\Delta z_{\mathrm{BAO}} = \frac{r_{\mathrm{s}}H(z)}{c}. \qquad (2.21)$$

Measuring the redshift-distance relation from BAO measurements has become a standard and very powerful tool in the field of observational cosmology over the last 10 years, after the first measurements on galaxy catalogs by Cole et al. (2005) and Eisenstein et al. (2005). Figure 2.2, reproduced from Anderson et al. (2014b), shows measurements on different galaxy surveys of the spherically-averaged distance defined as

$$D_{\mathrm{V}}(z) = \left((1+z)^2 D_{\mathrm{A}}^2(z) \frac{cz}{H(z)} \right)^{\frac{1}{3}}, \qquad (2.22)$$
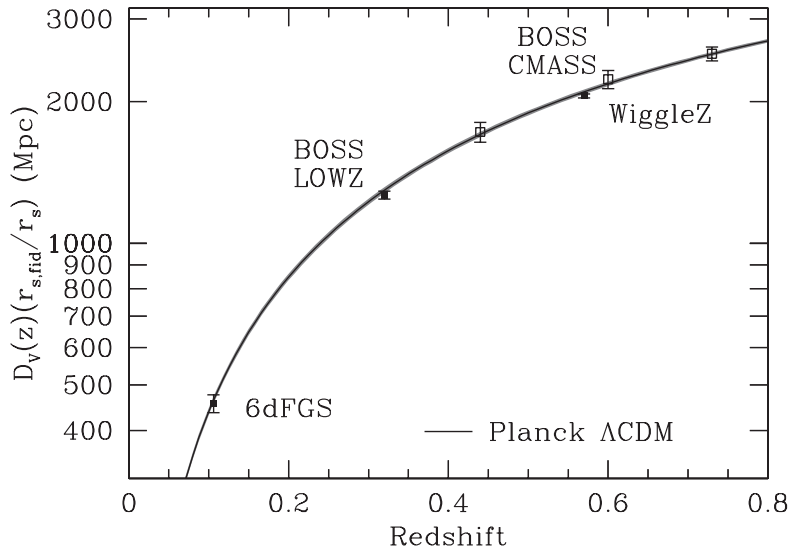
Figure 2.2: The distance-redshift relation from BAO measurements on galaxy surveys, reproduced from Anderson et al. (2014b). It shows the (normalised) spherically-averaged distance $D_{\mathrm{V}}(r_{\mathrm{s}}^{\mathrm{fid}}/r_{\mathrm{s}})$ as a function of redshift as measured on the DR11 BOSS survey (Anderson et al., 2014b), WiggleZ survey (Blake et al., 2011; Kazin et al., 2014), and 6dFGS survey (Beutler et al., 2011). The grey band corresponds to the prediction for D_{V} from Planck Collaboration XVI (2014) results assuming a ΛCDM cosmology.

as a function of redshift, normalised by the ratio between the real sound-horizon scale and the one corresponding to the fiducial cosmology used to perform the clustering measurements. Also shown, by a grey band, is the prediction from the best-fitting ΛCDM model from Planck Collaboration XVI (2014).

2.5　Galaxies as biased tracers of the density field

A useful theoretical framework in structure formation to describe the statistical properties of the galaxy distribution is the *halo model* (Scherrer and Bertschinger, 1991; Seljak, 2000; Peacock and Smith, 2000), where peaks (or maxima) in the density field, and matter around them, collapse into massive virialised structures called halos, and all galaxies form and live inside them. Large massive halos can host several galaxies, and there can be small halos with no galaxies. These halos represent an inhomogeneous Poisson process

that traces the high density regions of the underlying matter density field. With these assumptions, the halo model states that the statistics of the density field can be split into two components: (i) on small scales it is dominated by the internal structure of halos, and the distribution of halos is not relevant (the 1-halo term); and (ii), at scales larger than the typical size of a halo, it is dominated by their distribution (the 2-halo term), where the distribution of galaxies inside halos has a subdominant contribution.

In general, the halo field is biased with respect to the matter density field, and this bias depends mainly on the mass of the halo and the redshift. Assuming that the halo bias is a local function only (i.e. it only depends on the potential at that point), the halo density field can be expanded in terms of powers of the matter density field as

$$\delta_h(m, z) = \sum_{p=1} \frac{b_p(m, z)}{p!} \delta^p, \qquad (2.23)$$

where b_p are the (local) bias parameters. At the lowest level approximation, $\delta_h \approx b_1 \delta$, which implies that the correlation function of halos of masses m_1 and m_2 (for a fixed z), is related to that of the matter by

$$\xi_{hh}(r|m_1, m_2) = b_1(m_1)b_1(m_2)\xi(r), \qquad (2.24)$$

where b_1 is known as the linear bias.

If each halo had only one galaxy sitting at its centre (and so moving as the halo centre of mass), then the galaxy correlation function would be that of the halos, but as we mentioned above, this is not the case. Nevertheless, on scales sufficiently large to neglect the separation of galaxies within a halo, and their internal structure in general, we can modify the first order approximation in equation (2.24) as

$$\xi_g(r) = b_{g,1}^2 \xi(r), \qquad (2.25)$$

with the linear galaxy bias $b_{g,1}$ given by

$$b_{g,1} = \int dm \; n(m)b_1(m)\frac{\langle N_g|m\rangle}{\langle n_g\rangle}, \qquad (2.26)$$

where $n(m)$ is the number density of halos of a given mass m, $\langle N_g|m\rangle$ is the expected number of galaxies inside a halo of mass m, and

$$\langle n_g\rangle = \int dm \; n(m)\langle N_g|m\rangle, \qquad (2.27)$$

is the mean number density of galaxies.
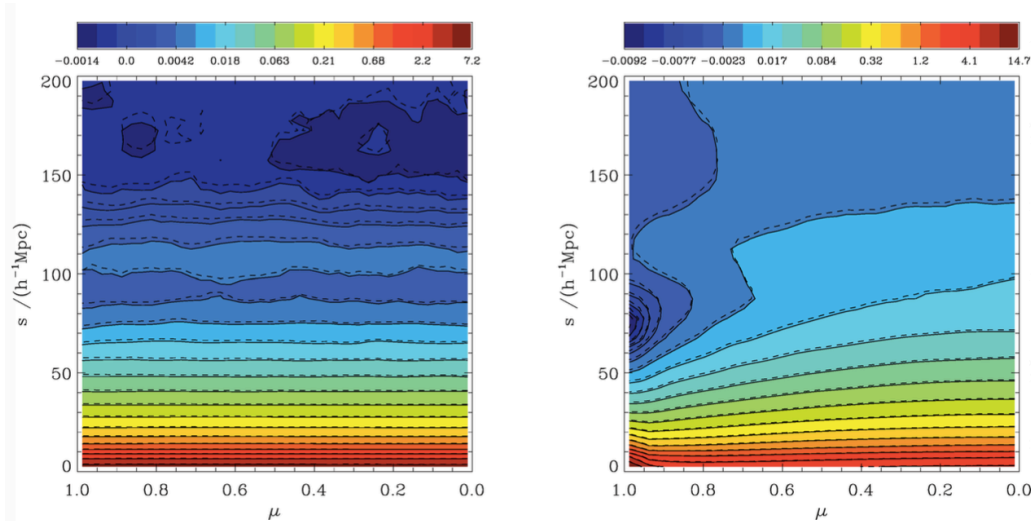
Figure 2.3: Mean anisotropic correlation function $\xi(s, \mu_s)$ measured from Las-Damas mock catalogues (McBride et al., 2009), reproduced from Kazin et al. (2012). The left panel is measured using the real-space positions of galaxies, while the right panel is in redshift-space.

As we look at smaller scales, still larger than the typical size of a halo, but small enough to be comparable to the separation between galaxies inside one of them, the contribution of higher-order bias factors and non-local biasing (i.e. as a function of the matter density field around a given point) becomes more important. These two will be treated later in §2.7.2. Moreover, different environmental effects that influence galaxy formation will also have an impact on the galaxy bias, introducing what is known as *stochastic biasing*.

In practice, since our understanding of the many processes that influence how galaxies form and populate halos is not accurate enough for cosmological studies, the biases are usually treated as free parameters in the modelling of the galaxy clustering signal.

2.6 Redshift-space distortions

So far, we have been treating the matter density field $\delta(\mathbf{x})$, and galaxies as tracers of it, assuming that we know their real three-dimensional position. In reality, we cannot observe the real positions of galaxies, but rather their angular coordinates in the sky and their redshift z, and even knowing the correct distance-redshift relation, the distances inferred from the measured z are not the true distances to the observed galaxies. This is due to the fact that the

observed redshifts are not only a consequence of the cosmological recession velocity driven by the expansion of the Universe, but have an additional contribution from the peculiar velocity $\mathbf{v}$ of each object. That is, for $v = |\mathbf{v}| \ll c$

$$cz = rH + \mathbf{v} \cdot \hat{\mathbf{n}} \quad \rightarrow \quad \mathbf{s} = \mathbf{r} + \frac{\mathbf{v} \cdot \hat{\mathbf{n}}}{H} \hat{\mathbf{n}}, \tag{2.28}$$

where $\hat{\mathbf{n}} = \mathbf{r}/r$, and $\mathbf{s}$ is the redshift-space distance to an object at real-space distance $\mathbf{r}$. The effect of this distortions is that galaxies with peculiar velocities moving toward us will appear to be closer than they really are, while the opposite applies for galaxies moving away from us, breaking the isotropy of the density field along the line-of-sight but not in the transverse direction. Figure 2.3 shows the effect of redshift-space distortions on the correlation function. The real-space ξ is shown in the left panel, as a function of the magnitude of the separation vector, s, and μ_s, the cosine of the angle between this vector and the line of sight. Naturally, ξ in real-space does not depend on μ_s, as opposed to its redshift-space counterpart shown in the right panel. Here, it can be seen that the signal perpendicular to the line of sight ($\mu \lesssim 0.5$) gets stretched, decreasing the slope of ξ at small scales, while the opposite happens along the line of sight ($\mu \gtrsim 0.5$), where even an anti-correlation is developed at intermediate scales $s \sim 70h^{-1}\mathrm{Mpc}$.

Since the velocity field is given by the gradient of the potential, these distortions are tightly connected to the density field. They are usually described by two components, a (linear) large-scale coherent flow towards dense regions called the *Kaiser* effect (Kaiser, 1987), and a small-scale random motion within virialised structures (i.e. clusters of galaxies) called the *Fingers-of-God* (FoG) effect. The latter is very difficult to model, and a phenomenological description is normally used (see §2.7.2).

To illustrate the linear effect, let us show how the evolution of δ is related to $\mathbf{v}$. In the linear regime we had that $\delta \propto D(t)$, thus

$$\frac{\partial \delta}{\partial t} = \frac{\partial \delta}{\partial a} \frac{da}{dt} = \delta \frac{\dot{a}}{a} \frac{\partial \ln D}{\partial \ln a}. \tag{2.29}$$

Replacing this in the mass conservation equation (2.5), and recalling that $H(a) \equiv \frac{\dot{a}}{a}$, we have

$$H(a)f(a)\delta = -\frac{1}{a}\nabla \cdot \mathbf{v}, \tag{2.30}$$

where $f(a) \equiv \frac{\partial \ln D}{\partial \ln a}$ is the growth rate factor. For the galaxy density field, in the linear regime we have $\delta_g = b_1 \delta$ (dropping the subscript g in the bias). If we assume no velocity bias, that is $\mathbf{v}_g = \mathbf{v}$, equation (2.30) can be written as

$$H(a)\beta\delta_g = -\frac{1}{a}\nabla \cdot \mathbf{v}, \tag{2.31}$$

where $\beta \equiv \frac{f}{b}$. Therefore, even when at first these distortions could appear to be a problem, they are in fact another source of information, since they are caused by the velocity field, which at the same time is linked to the growth of structures through f.

While solving (2.31) in configuration space to get an expression for $\delta_g(\mathbf{s})$ requires an integral operator (see Hamilton, 1998), in Fourier space this relation is significantly simpler. Following Kaiser (1987), in the plane-parallel approximation, which assumes that the observed galaxies are far away (or separated by a small angle), it is possible to show that

$$\tilde{\delta}_g^s(\mathbf{k}) = (1 + \beta\mu_k^2)\tilde{\delta}_g^r(\mathbf{k}), \tag{2.32}$$

where the r and s superscripts are for real- and redshift-space, and $\mu_k = \hat{\mathbf{n}} \cdot \hat{\mathbf{k}}$ is the cosine of the angle between the line of sight and the wave vector. This allows us to write the (linear) **anisotropic** galaxy power spectrum as

$$P_g(k, \mu_k) = b_1^2(1 + \beta\mu_k^2)^2 P(k), \tag{2.33}$$

where $(1 + \beta\mu_k^2)^2$ is usually known as *the Kaiser factor*.

Note that the Kaiser factor can be expanded in terms of three Legendre polynomials as

$$\begin{aligned}(1 + \beta\mu_k^2)^2 = &\left(1 + \frac{2}{3}\beta + \frac{1}{5}\beta^2\right) L_0(\mu_k) \\ &+ \left(\frac{4}{3}\beta + \frac{4}{7}\beta^2\right) L_2(\mu_k) + \frac{8}{35}\beta^2 L_4(\mu_k),\end{aligned} \tag{2.34}$$

where $L_\ell(\mu)$ are the Legendre polynomials of ℓ-th order. It is useful then to expand the anisotropic power spectrum as

$$P(k, \mu_k) = \sum_{\ell=0,2,4} P_\ell(k) L_\ell(\mu_k), \tag{2.35}$$

where $P_\ell(k)$ are the first three non-zero power spectrum multipoles: the monopole, quadrupole and hexadecapole. These multipoles are given by

$$P_\ell(k) = \frac{2\ell + 1}{2} \int d\mu_k \; P(k, \mu_k) L_\ell(\mu_k), \tag{2.36}$$

and even though, in theory, this expansion runs over an infinite number of even multipoles, from equation (2.34) it can be seen that in the linear regime the information is enclosed in only three of them, and the multipoles of order $\ell \geq 6$ cancel out.

Redshift-space distortions do not break homogeneity, thus $P(k, \mu_k)$ also determines the anisotropic correlation function $\xi(s, \mu_s)$. It is convenient to expand the two-dimensional spatial correlation function $\xi(s, \mu_s)$ analogously to equation (2.35) as

$$\xi(s, \mu_s) = \xi_0(s) + L_2(\mu_s)\xi_2(s) + L_4(\mu_s)\xi_4(s), \qquad (2.37)$$

where $\xi_0(s)$, $\xi_2(s)$ and $\xi_4(s)$ are the monopole, quadrupole and the hexadecapole of $\xi(s, \mu_s)$ respectively. These multipoles can be derived from those of the power spectrum as

$$\xi_\ell(s) = \frac{i^\ell}{2\pi^2} \int dk \ k^2 P_\ell(k) j_\ell(ks). \qquad (2.38)$$

where $j_\ell(x)$ is the spherical Bessel function of ℓ-th order (Hamilton, 1997).

2.7 The non-linear redshift-space power spectrum

Although linear theory has proved to be a very useful theoretical tool for the study of the large-scale structure of the Universe, non-linear effects are much more important today, especially at low redshift, as statistical errors of the state-of-the-art measurements on galaxy catalogs become smaller. This can be seen in figure 2.4, where measurements on a set of 100 N-body simulations (blue band), dubbed MINERVA (Grieb et al., 2016), are compared to the corresponding linear-theory prediction (dashed lines), and the two non-linear approaches used in this work. It is clear that, already at $k \sim 0.1h/\text{Mpc}$, linear theory does not give a good description of the matter power spectrum.

Non-linearities occur because the effect of gravity is not only local as we assumed before, thus not only amplifies the initial density peaks in place, but also affects others in their environment. The effect that non-linearities have on two-point statistics is a coupling between small and large k-modes, that in the power spectrum corresponds basically to a transfer of power from small values of k to large ones.

Non-linearities also have a damping effect on the BAO signal, that in the case of ξ results in a broadening of the acoustic bump and a slight shift of its centroid towards smaller scales (Crocce and Scoccimarro, 2008). This means that if the non-linear evolution of the density field is not properly taken into account, it could lead to biased measurements of the redshift-distance relation in (2.20) and (2.21).
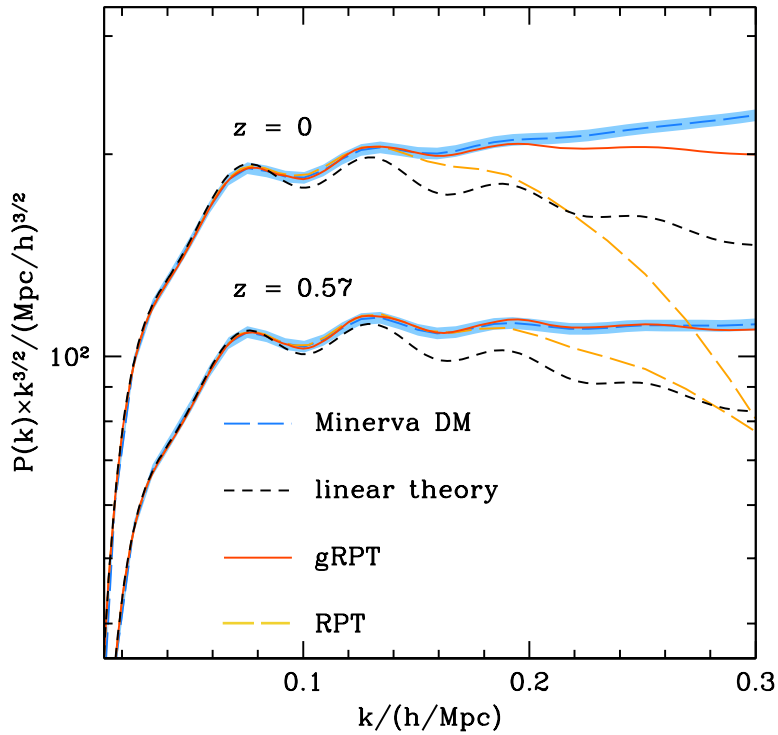
Figure 2.4: Non-linear matter power spectrum at redshift $z = 0$ and $z = 0.57$. The dashed yellow line corresponds to the prediction by 2-loop RPT, while the solid red line corresponds to that of 1-loop gRPT. These two models are compared to linear theory (black dashed line). The blue dashed line and light blue band correspond to the mean and 2% error measurements from a set of 100 N-body simulations dubbed MINERVA (Grieb et al., 2016).

There are many approaches to model the non-linear evolution of density fluctuations, from perturbation theory (in Eulerian and Lagrangian coordinates) and effective field theory of large-scale structure (EFTofLSS; Carrasco et al., 2012; Angulo et al., 2015a,b), to numerical approaches using N-body simulations to derive recipes of how these non-linearities depend on different cosmological models (Smith et al., 2003; Heitmann et al., 2009, 2010). In this work, we use two different perturbative approaches: one based on **Renormalised Perturbation Theory** (RPT; Crocce and Scoccimarro, 2006) in chapter 3, and a similar approach called **gRPT** (Blas, Crocce & Scoccimarro, in prerp) in chapter 4. We will describe these two here.

2.7.1 The Non-linear Matter Power Spectrum in real space

In Standard Perturbation Theory (SPT), the idea is to express the non-linear evolution of $\tilde{\delta}$ as a perturbative expansion over powers of the linear solution in the following manner,

$$\tilde{\delta} = \sum_{p=1}^{\infty} \tilde{\delta}^{(p)}, \tag{2.39}$$

where $\tilde{\delta}^{(p)} \propto \left(\tilde{\delta}_L\right)^p$, and $\tilde{\delta}_L$ corresponds to the Fourier transform of the linearised solution in equation (2.8). Then, the two-point covariance function (the power spectrum), is given by

$$\langle \tilde{\delta}\tilde{\delta} \rangle = \langle \tilde{\delta}^{(1)}\tilde{\delta}^{(1)} \rangle + \langle \tilde{\delta}^{(1)}\tilde{\delta}^{(3)} \rangle + \langle \tilde{\delta}^{(3)}\tilde{\delta}^{(1)} \rangle + \langle \tilde{\delta}^{(2)}\tilde{\delta}^{(2)} \rangle + \cdots, \tag{2.40}$$

where this effectively yields

$$P(k) = \sum_{p=1}^{\infty} P^{(p)}(k), \tag{2.41}$$

where $P^{(p)}(k) \propto (P_L(k))^p$ are known as the ℓ-loop corrections, with $\ell = (p-1)$, for $p > 1$ ($p = 1$ corresponds to $P_L(k)$, which would be the "0-loop"). The issue with SPT is that many ℓ-loop corrections contribute equally to a given scale k, making it extremely difficult to know where to truncate the series of corrections and to physically interpret each correction.

Renormalised perturbation theory consists in a way of reorganising the (infinite) terms of SPT in two sums, where the first one adds up to a defined function $G(k)$ called the *propagator*, which is very well approximated by an exponential factor and measures how initial conditions are erased, through

gravitational effects, as a function of k. The remaining (infinite) terms are reorganised in a well-defined expansion of ℓ-loop corrections that account for the effects of $(\ell + 1)$-mode-coupling, thus effectively defining the non-linear matter power spectrum as

$$P_{NL}(k) = P_L(k)G^2(k) + \sum_{\ell} P_{\mathrm{MC}}^{(\ell)}(k). \tag{2.42}$$

Unlike SPT, each $\ell-$loop correction dominates over a narrow range of scales, which makes it much easier to know how many terms are required to get the non-linear power spectrum up to a given scale k_{max}.

A practical issue of RPT is that its ℓ-loop terms start to crowd as ℓ increases, progressively requiring more and more terms to go to higher values of k. However, Crocce and Scoccimarro (2006) proposed that there are symmetries (e.g. Galilean invariance) that could be used to connect the resummation of the mode-coupling series with that of the propagator, which one might be able to take advantage of. This idea has recently been put into practice by Blas, Crocce and Scoccimarro (in prep).

In a new approach, dubbed gRPT, they use Galilean invariance (invariance under translations) to reorganise the mode-coupling terms of RPT in such a way that already the 1-loop contribution gives the non-linear corrections that would require many terms in RPT. Figure 2.4 shows a comparison between RPT (left) and gRPT(right), against measurements on MINERVA, where a significant improvement can be seen at the 1-loop correction level.

2.7.2 The Non-linear Galaxy Power Spectrum in redshift space

In general, the non-linear redshift-space galaxy power spectrum can be written as

$$P(k, \mu_k) = F(ifk\mu_k)P_{\mathrm{nonvir}}(k, \mu_k), \tag{2.43}$$

where $P_{\mathrm{nonvir}}(k, \mu_k)$ represents the *non-virial* power spectrum, normally the non-linear $P(k)$ plus the coherent part of RSD, and $F(ifk\mu_k)$ is a function that accounts for the FoG effect.

RPT-based model

For our first approach, based on RPT, since we are only interested in performing a simple proof of concept in chapter 3, it is sufficient to consider the linear galaxy bias only, as in equation (2.33), and replace the linear matter power

spectrum with the non-linear one in order to model $P_{\mathrm{nonvir}}(k, \mu_k)$. That is, the non-virial part of the redshift-space power spectrum can be written as

$$P_{\mathrm{nonvir}}(k, \mu_k) = b_1^2 (1 + \beta \mu_k^2)^2 P_{NL}(k), \tag{2.44}$$

where in this case, we parametrise the non-linear real-space galaxy power spectrum as

$$P_{NL}(k) = P_L(k) \mathrm{e}^{-(k\sigma_{\mathrm{v}})^2} + A_{\mathrm{MC}} P_{\mathrm{MC}}(k), \tag{2.45}$$

where $\mathrm{e}^{-(k\sigma_{\mathrm{v}})^2}$ corresponds to our approximation of the propagator, σ_{v} is the (one-dimensional) linear velocity dispersion, A_{MC} is a constant that modulates the amplitude of the mode-coupling part, and the (infinite series of) mode-coupling corrections are well approximated, up to $k \sim 0.15 h/\mathrm{Mpc}$, by

$$P_{\mathrm{MC}}(k) = \frac{1}{4\pi^3} \int d^3q \left[|F_2(\mathbf{k} - \mathbf{q}, \mathbf{q})|^2 \, P_L(|\mathbf{k} - \mathbf{q}|) P_L(q) \right], \tag{2.46}$$

where $F_2(\mathbf{k}, \mathbf{q})$ is the standard second order kernel of perturbation theory (Crocce et al., 2012) given by

$$F_2(\mathbf{q}_1, \mathbf{q}_2) = \frac{5}{7} + \frac{1}{2} \frac{\mathbf{q}_1 \cdot \mathbf{q}_2}{q_1 q_2} \left(\frac{q_1}{q_2} + \frac{q_2}{q_1} \right) + \frac{2}{7} \left(\frac{\mathbf{q}_1 \cdot \mathbf{q}_2}{q_1 q_2} \right)^2. \tag{2.47}$$

In this approach, we model the FoG effect by a Lorentzian pre-factor given by

$$F(\lambda) = \left(\frac{1}{1 - \lambda^2 \sigma_{\mathrm{v}}^2} \right)^2 \tag{2.48}$$

that gives a very good description of the *Fingers-of-God* damping effect, assuming an exponential galaxy velocity distribution function (Park et al. 1994; Cole et al. 1995). This last component defines then the RPT-based non-linear redshift-space galaxy power spectrum as

$$P(k, \mu_k) = b_1^2 \left(\frac{1}{1 + (k f \sigma_{\mathrm{v}} \mu_k)^2} \right)^2 \left(1 + \beta \mu_k^2 \right)^2 P_{NL}(k). \tag{2.49}$$

This model, that effectively has three nuisance parameters, b_1, σ_{v} and A_{MC}, has been shown to give a very good description of non-linear evolution and RSD in measurements of both N-body simulations (Sánchez et al., 2008; Montesano et al., 2010) and real galaxy samples (Sánchez et al., 2009, 2012, 2013, 2014; Montesano et al., 2012), up to scales of $k \sim 0.15 h/\mathrm{Mpc}$.

gRPT-based model

In chapter 4, the goal is to push the analysis to the smallest possible scales, and for this we drop the simple model described above, and use gRPT. In this case we include non-linear and non-local biasing and RSD, and extend the modelling of the clustering signal to the smallest possible scales.

Expanding the galaxy density field δ_g up to second order as (Chan et al., 2012; Chan and Scoccimarro, 2012)

$$\delta_g \approx b_1\delta + \frac{b_2}{2}\delta^2 + \gamma_2\mathcal{G}_2(\Phi_{\mathrm{v}}) + \gamma_3^-\Delta_3\mathcal{G} + \cdots, \qquad (2.50)$$

where Φ_{v} is the velocity potential, γ_2 and γ_3^- are non-local bias parameters, and the Galileon operators $\mathcal{G}_2$ and $\Delta_3\mathcal{G}$ are given by

$$\mathcal{G}_2(\Phi) = (\nabla\Phi)^2 - (\nabla^2\Phi)^2, \qquad \Delta_3\mathcal{G} = \mathcal{G}_2(\Phi) - \mathcal{G}_2(\Phi_{\mathrm{v}}); \qquad (2.51)$$

the non-virial part of the power spectrum, $P_{\mathrm{nonvir}}(k, \mu_k)$, can be expressed at 1-loop as the sum of three contributions, i.e.

$$P_{\mathrm{nonvir}}(k, \mu_k) = P^{(1)}(k, \mu_k) + P^{(2)}(k, \mu_k) + P^{(3)}(k, \mu_k). \qquad (2.52)$$

The first term, $P^{(1)}(k, \mu_k)$, is given by

$$P^{(1)}(k, \mu_k) = P_{gg}(k) + 2f\mu_k^2 P_{g\theta}(k) + f^2\mu_k^4 P_{\theta\theta}(k), \qquad (2.53)$$

where P_{gg}, $P_{g\theta}$ and $P_{\theta\theta}$ are the galaxy-galaxy, galaxy-velocity (divergence) and velocity-velocity power spectra, respectively. Each of these terms has contributions from cross-spectra of terms of the expansion in equation (2.50), and corresponds to the non-linear version of the Kaiser power spectrum in equation (2.33). Similarly, the second term is

$$P^{(2)}(k, \mu_k) = \int d^3q\frac{q_z}{q^2}\left[B_{\theta D_s D_s'}(\mathbf{q}, \mathbf{k} - \mathbf{q}, -\mathbf{k}) + B_{\theta D_s D_s'}(\mathbf{q}, -\mathbf{k}, \mathbf{k} - \mathbf{q})\right], \qquad (2.54)$$

where $B_{\theta D_s D_s'}$ is the **Bispectrum** (the third-order covariance function in Fourier space), $D_s \equiv \delta_g + \nabla_z u_z$ and $\mathbf{u} = \mathbf{v}/a$ is the (comoving) peculiar velocity. Finally, the third term is given by

$$P^{(3)}(k, \mu_k) = \int d^3q\frac{q_z}{q^2}\frac{k_z - q_z}{(\mathbf{k} - \mathbf{q})^2}(b_1 + f\mu_q^2)(b_1 + f\mu_{k-q}^2)P_{\delta\theta}(k - q)P_{\delta\theta}(q). \qquad (2.55)$$

Assuming that the bias is local in Lagrangian coordinates, the non-local bias parameters (in Eulerian coordinates) γ_2 and γ_3^- can be set as a function of the linear bias as

$$\gamma_2 = -\frac{2}{7}(b_1 - 1), \qquad \gamma_3^- = \frac{1}{42}(b_1 - 1). \qquad (2.56)$$
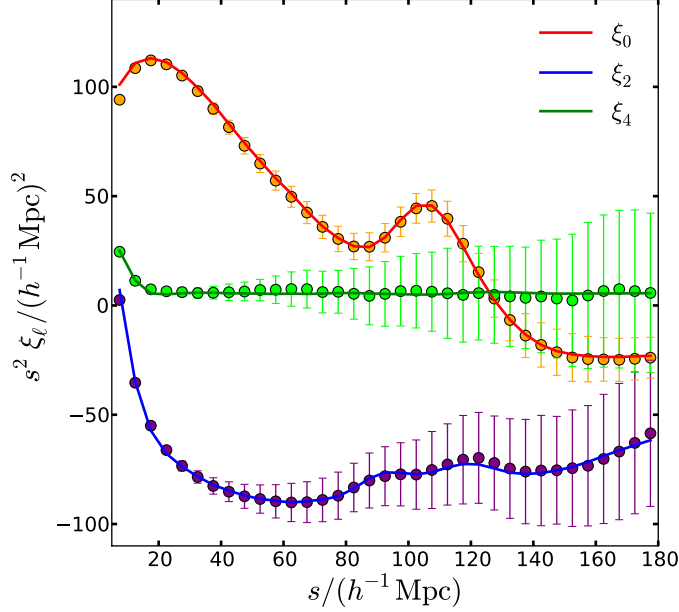
Figure 2.5: Mean monopole, quadrupole and hexadecapole, shown by symbols, measured from 100 mock galaxy catalogs made from the MINERVA simulations. The errors correspond to those expected from a single realisation. The solid lines show the prediction from the gRPT+bias+RSD model used for the analysis in chapter 4.

The virial part in this gRPT-based model, corresponding to a description of the FoG effect in the large-scale limit, is given by

$$W_\infty(\lambda) = \frac{1}{\sqrt{1 - \lambda^2 a_{\mathrm{vir}}^2}} \exp\left(\frac{\lambda^2 \sigma_{\mathrm{v}}^2}{1 - \lambda^2 a_{\mathrm{vir}}^2}\right), \qquad (2.57)$$

where a_{vir} is a free parameter that characterises the kurtosis of the velocity distribution within virialised structures, and the linear velocity dispersion is not a free parameter as in the previous model, but given by $\sigma_{\mathrm{v}} = \psi_\perp(0)$, where $\psi_\perp(r) = (I_0 + I_2)/3$ and

$$I_\ell(r) \equiv \int d^3k \, j_\ell(kr) \frac{P_L(k)}{k}. \qquad (2.58)$$

This model provides a significant improvement with respect to the previous RPT-based model, and is able to describe the non-linear evolution and RSD up to very small scales remarkably well (Sánchez et al., in prep; Grieb et al., in prep), setting γ_2 to the local-Lagrangian relation, and treating b_1, b_2, γ_3^- and a_{vir} as nuisance parameters. Figure 2.5 shows a comparison of the monopole,

quadrupole and hexadecapole of $\xi(s, \mu_s)$ measured from mock galaxies in the MINERVA simulations, against the prediction of our gRPT+bias+RSD model, showing an excellent agreement up to scales well into the so called *quasi-linear* regime ($s \gtrsim 15h^{-1}\mathrm{Mpc}$).

As a final comment, state-of-the-art dark-matter only methods to account for non-linear effects are reaching their limit. Baryonic effects are increasingly becoming more important in order to include smaller scales (larger values of k) into the analysis. For instance, in figure 2.4, the prediction by gRPT in the right panel gives a very good description of the (dark) matter power spectrum up to $k \sim 0.2h/\mathrm{Mpc}$ at $z = 0$ and $k \sim 0.3h/\mathrm{Mpc}$ at $z = 0.57$. The latter is the scale where the power spectrum, measured from hydrodynamical simulations that include baryonic processes (e.g. cooling and feedback), starts to differ from that of dark matter only simulations, with this deviation already being significant at $k \sim 0.5h/\mathrm{Mpc}$, and reaching a maximum at $k \sim 2h/\mathrm{Mpc}$ (see e.g Schneider and Teyssier, 2015). New theoretical frameworks considering the non-linear growth of perturbations in various components, and the coupling between them, will be necessary in the near future.

Chapter 3

Clustering Tomography

There are two important issues related to the traditional analysis of LSS that need to be considered. First, in order to use the 3D positions of galaxies, it is necessary to assume a fiducial cosmological model in order to transform the measured angular positions on the sky and redshifts of galaxies into comoving coordinates or distances, a process which could bias the parameter constraints if not treated carefully (see e.g. Eisenstein et al. 2005 and Sánchez et al. 2009). Secondly, in order to obtain a precise measurement of either the correlation function or the power spectrum, usually the whole galaxy sample is used to obtain one measurement, typically averaging over a wide redshift range assuming that the measurement at the mean redshift is representative of the entire sample, washing out information on the redshift evolution of the structures.

Even when these two issues are well understood and under control within certain conditions, a simple way to avoid them is by using two-point statistics based only on direct observables, i.e. only angular positions and/or redshifts, such as the angular correlation function $\omega(\theta)$ or the angular power spectrum C_ℓ. This is done by dividing the sample into redshift bins, or shells, in order to recover information along the line of sight, which would otherwise be lost due to projection effects. In the last few years there have been several studies modelling and analysing large galaxy catalogues using angular two-point statistics. Although most of these focus mainly on photometric-redshift galaxy surveys (Crocce et al. 2011a,b, Padmanabhan et al. 2007, Ross et al. 2011, Sánchez et al. 2011, de Simoni et al. 2013), this approach has also been considered for spectroscopic-redshift samples (Asorey et al. 2012, 2014, Di Dio et al. 2014, Salazar-Albornoz et al. 2014). Here we focus on the cosmological implications of applying this tomographic approach to a BOSS-like spectroscopic-redshift galaxy survey, computing $\omega(\theta)$ in redshift-shells and using this information to obtain constraints on cosmological parameters.

There are three main advantages of this tomographic approach: (i) com-

pared to that of photometric redshifts (photo-z), the higher accuracy of spectroscopic redshifts significantly reduces the overlap between redshift shells, allowing us to assume that there is no correlation between them due to these uncertainties, and to use thinner shells. Compared to the traditional 3D analysis, (ii) by using direct observables we do not need to assume a cosmological model in order to compute spatial separations between galaxies, their angular separations will remain unaffected independently of the cosmological model being tested; (iii) By measuring the angular scale of the BAO peak imprinted on $\omega(\theta)$ at many different redshifts, we are basically measuring the angular diameter distance $D_A(z)$ at several redshifts instead of just one more precise measurement of the average distance $D_V(\bar{z})$ at the mean redshift of the sample, giving us more information about the rate at which D_A evolves, putting stronger constraints on the expansion history of the Universe. This chapter is based on Salazar-Albornoz et al. (2014).

3.1 Angular Correlation Functions in redshift shells

3.1.1 LasDamas Mock Catalogues

We used a set of 160 spectroscopic luminous red galaxies (LRGs) mock catalogues from LasDamas[1] (McBride et al., 2009), constructed from a set of 40 dark-matter only N-body simulations, all of them following the same ΛCDM cosmological model and using the same initial power spectrum but a different random seed. The specifications of these simulations are outlined in Table 3.1. From each realisation, a halo catalogue is extracted using a friends-of-friends algorithm (FoF; Davis et al., 1985), and populated with mock galaxies following a halo occupation distribution (HOD; Peacock and Smith, 2000; Berlind and Weinberg, 2002) in order to reproduce the SDSS DR7 (Abazajian et al., 2009) clustering signal. Each realisation provides 4 catalogues without overlap, reproducing the SDSS DR7 geometry (northern Galactic cap only), containing an average of 91137 galaxies per catalogue within the redshift range $[0.16, 0.44]$, and including redshift-space distortions (RSD) from peculiar velocities. These catalogues, and the corresponding random field (which contains 50 times more objects than one of these catalogues) needed to measure the correlation functions, were modified to follow the radial number density $n(z)$ of the SDSS DR7 LRGs (see figure 1 in Montesano et al. 2012).

    We divided each mock catalogue and the random field into redshift shells

---

[1]http://lss.phy.vanderbilt.edu/lasdamas
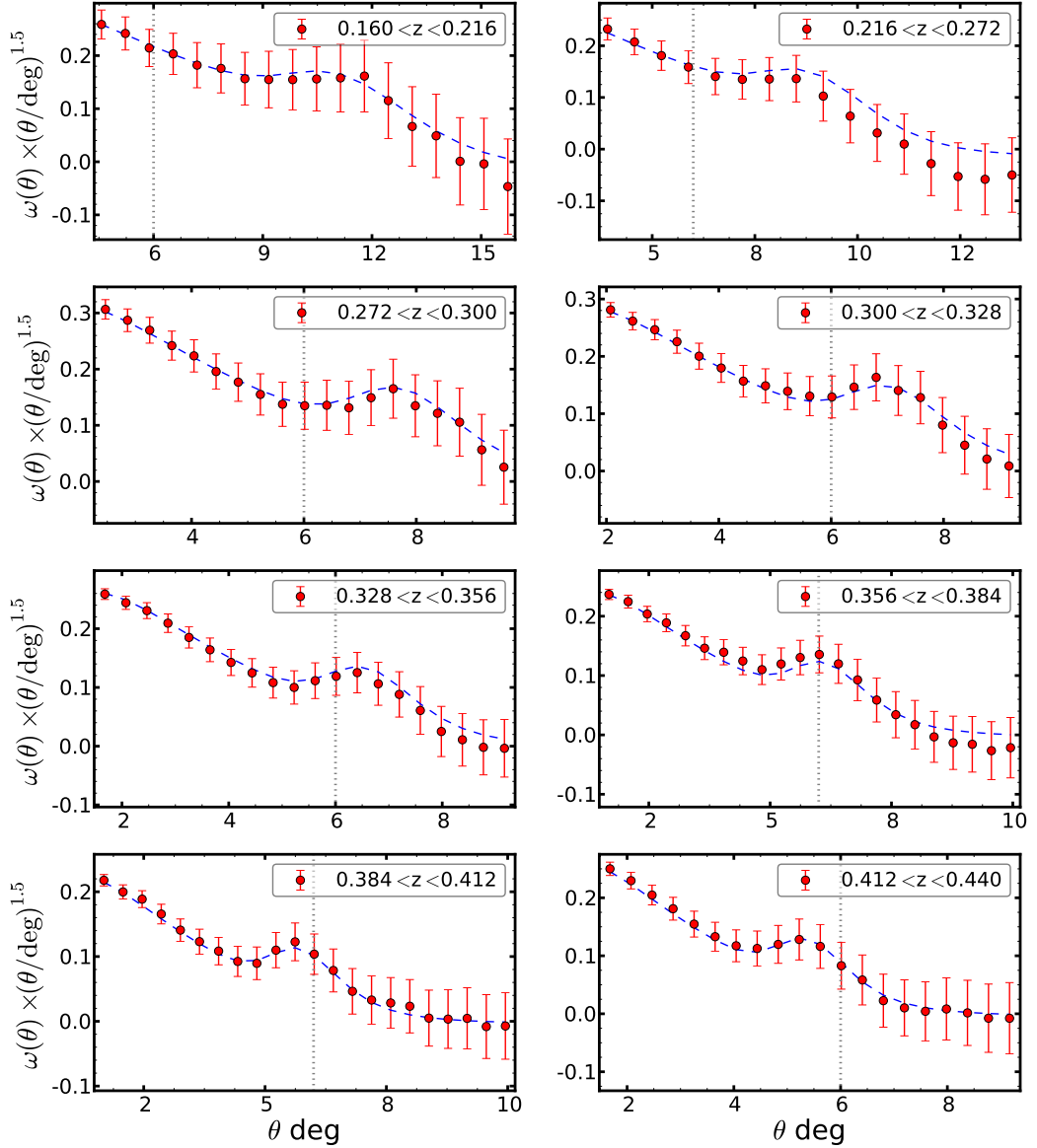
Figure 3.1: Mean $\omega(\theta)$ measured on the mock catalogues for 8 redshift-shells, amplified by $(\theta/deg)^{1.5}$ to highlight the BAO peak. The errorbars correspond to the error in the mean. The blue dashed lines show the best-fitting model, described in §3.2.1 and §3.2.2, for the cosmology of LasDamas, which simultaneously reproduces $\omega(\theta)$ for every shell. The vertical dotted line is a reference located at 6 deg., drawn to show how the BAO peak moves relative to a fixed scale depending on the redshift.

Cosmological constant density parameter	Ω_Λ	0.75
Matter density parameter	$\Omega_{\rm M}$	0.25
Baryonic density parameter	$\Omega_{\rm b}$	0.04
Dark energy equation of state	w_{DE}	-1.0
Hubble constant $\left({\rm km\ s^{-1} Mpc^{-1}}\right)$	H_0	70
Amplitude of density fluctuations	σ_8	0.8
Scalar spectral index	$n_{\rm s}$	1.0
Number of particles	N_p	1280^3
Box size $(h^{-1}{\rm Mpc})$	L	2400
Particle mass $(10^{10} M_\odot)$	M_p	45.73
Softening length $(h^{-1}{\rm kpc})$	ϵ	53

Table 3.1: Cosmological parameters and specifications of the LasDamas simulation.

to perform our analysis. Thicker shells lower the signal of the BAO peak, because it is projected over an increasingly wide range of angular scales given by the deeper sample. Thinner shells increase the BAO signal, but decrease the projected number density and therefore decrease the accuracy of the measurements, while increasing the correlation between shells due to RSD effects and the clustering itself. Using a spectroscopic-redshift sample, any overlap between redshift-shells due to redshift uncertainties can be safely neglected as long as their width is much larger than these uncertainties. We tested a number of configurations in order to estimate the optimal redshift bin size, considering the strength of the BAO signal and the uncertainty in measuring $\omega(\theta)$. For simplicity we ignored any correlation between shells, but, as discussed by Asorey et al. (2012) and Di Dio et al. (2014), and later on in §4.2.4, cross-correlations add extra information. The final configuration for LasDamas consists of 8 shells: 2 low redshift shells of $\Delta z = 0.056$ covering the redshift range $[0.16, 0.272]$, and 6 higher redshift shells of $\Delta z = 0.028$ covering the redshift range $[0.272, 0.44]$.

We use the estimator proposed by Landy and Szalay (1993) to compute the angular auto-correlation function of a given redshift shell as

$$\omega(\theta_i) = \frac{DD_i - 2DR_i + RR_i}{RR_i}, \qquad (3.1)$$

where DD_i, DR_i and RR_i are the data-data, data-random and random-random pair counts in the θ_i bin, respectively. We computed the angular correlation

function $\omega(\theta)$ in every shell of each mock catalogue and used these measurements to compute the mean $\omega(\theta)$ of each shell and to estimate its associated covariance matrix. These measurements only depend on direct observables (angular positions and redshifts) and do not require the assumption of a fiducial cosmological model to be computed and thus will remain invariant when considering the constraints on cosmological parameters. Figure 3.1 shows the mean $\omega(\theta)$ measured from the 8 shells, amplified by $\theta^{1.5}$ in order to highlight the BAO feature, and where the error bars correspond to the error in the mean. The dashed lines show the best-fitting model (described in §3.2.1 and §3.2.2) for the cosmology of LasDamas, which simultaneously reproduces $\omega(\theta)$ for every shell.

3.1.2 Measuring distances using $\omega(\theta)$ in redshift-shells

If we look again carefully at figure 3.1, it can be seen that the BAO peak in $\omega(\theta)$ is located at different angular scales depending on the redshift shell, i.e. depending on the distance to that shell; this is the key feature that we want to exploit. Let us say that we are only measuring the angular position θ_s of the BAO peak, then for a given redshift z_i we have

$$\theta_s(z_i) = r_s(z_d)/D_{\mathrm{M}}(z_i), \tag{3.2}$$

where $r_s(z_d)$ is the (comoving) sound horizon at the drag redshift, and D_{M} is the angular diameter distance. Using the fact that the sound horizon corresponds to a fixed scale, in linear theory we can relate its angular scale as $\theta_s(z_i) = \alpha_{ij}\theta_s(z_j)$, where α_{ij} is defined as

$$\alpha_{ij} \equiv \frac{D_{\mathrm{M}}(z_j)}{D_{\mathrm{M}}(z_i)}. \tag{3.3}$$

Then, we can extend this relation to the angular correlation function of two different shells as

$$\omega(\theta, z_i) \simeq \omega(\alpha_{ij}\theta, z_j). \tag{3.4}$$

In figure 3.2 we show the mean $\omega(\theta)$ measured in three different redshift-shells of LasDamas, where two of them have been rescaled using as reference the third one following equation (3.4), computing D_{M} at their mean redshift. The error bars have been omitted for clarity. It can be seen that they match remarkably well on applying the simple relation in equation (3.4), despite the fact that there are some small differences in their shape due to the non-linear evolution of the density field and RSD, which are discussed in §3.2.

The technique discussed in this work is based on the following idea: if we have N measurements of $\omega(\theta)$ in different redshift shells, in practice we have
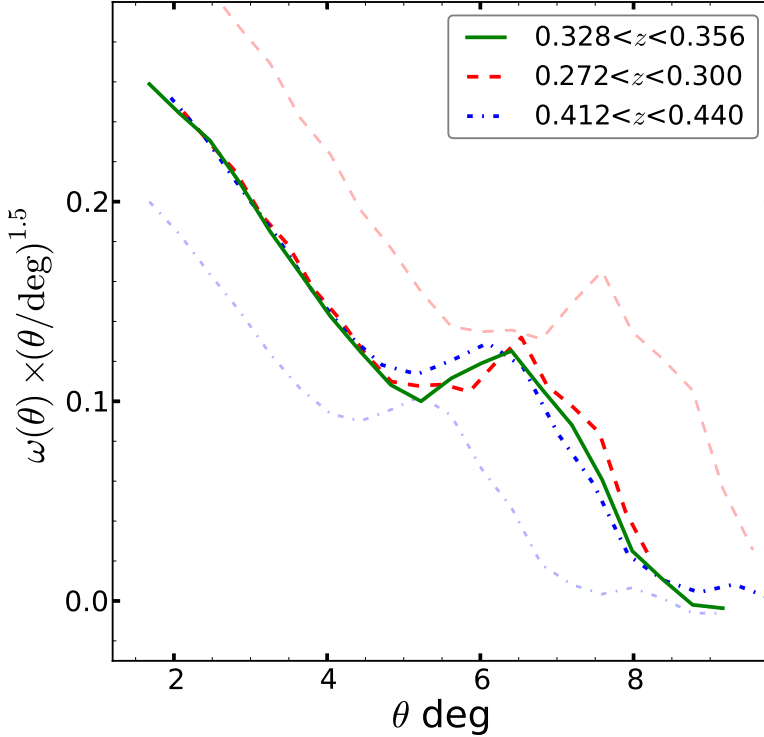
Figure 3.2: The mean $\omega(\theta)$ measured on LasDamas for three different shells, amplified by $(\theta/deg)^{1.5}$. Two of them have been rescaled following equation (3.4) (dashed and dash-dotted lines) using the third one as reference (solid line), from their original position (faint-colour version).

$N - 1$ measurements of $D_{\mathrm{M}}(z_i)/D_{\mathrm{M}}(z_j)$ for $i \neq j$, constraining the rate at which the angular diameter distance can evolve over the redshift range being tested.

3.2   Modelling $\omega(\theta)$ and its covariance matrix

Here we describe our model of the two-point angular correlation function used to extract information from the full shape of $\omega(\theta)$ without introducing systematic errors, starting in §3.2.1 from the description of its analytical model in thin redshift shells and the distortion effects that have to be taken into account, then going on to describe in §3.2.2 how to include such effects by modelling the anisotropic two-point spatial correlation function. In §3.2.3 we briefly describe the model for the covariance matrix of $\omega(\theta)$ and compare it with the ones measured from the mock catalogues.

3.2.1 Angular clustering in redshift shells

The projection of the spatial density fluctuation field along the line of sight, in a certain direction $\hat{\mathbf{n}}$ in the sky, is given by

$$\delta(\hat{\mathbf{n}}) = \int dz\phi(z)\delta(r\hat{\mathbf{n}}), \tag{3.5}$$

where $\phi(z)$ is the radial selection function normalised to unity within a redshift-shell, which for this work is defined as

$$\phi(z) = \frac{\frac{dN_g}{dz}\vartheta(z)}{\int dz\,\frac{dN_g}{dz}\vartheta(z)}, \tag{3.6}$$

where $\frac{dN_g}{dz}$ is the number of galaxies per unit redshift, and $\vartheta(z)$, in terms of the redshift range of each shell $[z_i, z_f]$, is given by

$$\vartheta(z) = \begin{cases} 1 & z_i < z < z_f \\ 0 & \text{otherwise} \end{cases}. \tag{3.7}$$

Similarly, the angular two-point correlation function, which is nothing other than $\langle\delta(\hat{\mathbf{n}})\delta(\hat{\mathbf{n}}')\rangle$, can be obtained from the projection of its spatial counterpart ξ (Peebles, 1973). That is,

$$\omega(\theta) = \int\int dz_1 dz_2\phi(z_1)\phi(z_2)\xi(s), \tag{3.8}$$

where s is the comoving pair separation, and θ is the angular separation on the sky.

When working on thin redshift shells, it is essential to include non-linear and redshift-space distortion effects in the modelling of $\omega(\theta)$ (Nock et al. 2010; Ross et al. 2011; Fosalba et al. 2015). This is shown in figure 3.3, where different approaches, applying corrections for these effects or not, are compared to the measurements made on the mock catalogues. It can be seen that the RSD corrections have the strongest effects on the full shape of $\omega(\theta)$, but are not enough to describe the damping effects on the BAO peak without including non-linear corrections, which also slightly move the centroid of the peak towards smaller scales. In order to fully describe the shape of $\omega(\theta)$ including these effects, we replaced the isotropic spatial correlation function in equation (3.8) by the anisotropic two-dimensional spatial correlation function described in §3.2.2. Using this, the model for $\omega(\theta)$ is given by

$$\omega(\theta) = \int\int dz_1 dz_2\phi(z_1)\phi(z_2)\xi(s,\mu_s), \tag{3.9}$$

where μ_s is the cosine of the angle between the separation vector **s** and the line of sight.

The last ingredient to model $\omega(\theta)$ are expressions for the comoving separation s and $\mu_s \equiv \cos\varphi$, the cosine of the angle φ between the separation vector and the line of sight, as a function of $\{z_1, z_2, \theta\}$.

Assuming that the geometry of the Universe is described by the FRW metric, the line-of-sight comoving distance to a given redshift z is given by,

$$D_C(z) = D_H \chi(z), \tag{3.10}$$

where $D_H \equiv \frac{c}{H_0}$ is the Hubble distance, H_0 is the value of the Hubble constant today, and $\chi(z)$ is given by

$$\chi(z) = \int_0^z \frac{dz'}{E(z')}, \tag{3.11}$$

defining $E(z) \equiv \frac{H(z)}{H_0}$. On the other hand, the transverse comoving distance, defined as the comoving distance we would infer between two objects at the same redshift knowing their angular and comoving separation, is given by,

$$D_M(z) = \begin{cases} \frac{D_H}{\sqrt{|\Omega_K|}} S_K\left[\chi(z)\right] & \Omega_K \neq 0 \\ \\ D_H S_K\left[\chi(z)\right] & \Omega_K = 0 \end{cases}, \tag{3.12}$$

where $\Omega_K \equiv \frac{-K}{H_0^2}$ is the curvature density parameter today, with $K = \{-1, 0, +1\}$, and $S_K\left[\chi(z)\right]$ is defined as

$$S_K\left[\chi(z)\right] = \begin{cases} \sinh\left(\sqrt{\Omega_K}\chi(z)\right) & \Omega_K > 0 \\ \\ \chi(z) & \Omega_K = 0 \\ \\ \sin\left(\sqrt{|\Omega_K|}\chi(z)\right) & \Omega_K < 0 \end{cases}. \tag{3.13}$$

With this, the comoving separation between two objects (galaxies) at different redshifts with an angular separation θ on the sky, $s(z_1, z_2, \theta)$, is given by

$$s(z_1, z_2, \theta) = \begin{cases} \frac{D_H}{\sqrt{|\Omega_K|}} S_K\left[\chi_{(1,2)}\right] & \Omega_K \neq 0 \\ \\ D_H S_K\left[\chi_{(1,2)}\right] & \Omega_K = 0 \end{cases}, \tag{3.14}$$

where $S_{\mathrm{K}}\left[\chi_{(1,2)}\right]$ can be obtained from the spherical cosine rule (generalised for positive and negative curvature) as (Peacock, 1999; Liske, 2000),

$$
\begin{aligned}
S_{\mathrm{K}}^2\left[\chi_{(1,2)}\right] = {} & S_{\mathrm{K}}^2\left[\chi(z_1)\right] C_{\mathrm{K}}^2\left[\chi(z_2)\right] + S_{\mathrm{K}}^2\left[\chi(z_2)\right] C_{\mathrm{K}}^2\left[\chi(z_1)\right] \\
& + \mathrm{K} S_{\mathrm{K}}^2\left[\chi(z_1)\right] S_{\mathrm{K}}^2\left[\chi(z_2)\right] \sin^2\theta \\
& - 2 S_{\mathrm{K}}\left[\chi(z_1)\right] S_{\mathrm{K}}\left[\chi(z_2)\right] C_{\mathrm{K}}\left[\chi(z_1)\right] C_{\mathrm{K}}\left[\chi(z_2)\right] \cos\theta,
\end{aligned}
\tag{3.15}
$$

defining $C_{\mathrm{K}}\left[\chi(z)\right] \equiv \sqrt{1 - \mathrm{K} S_{\mathrm{K}}^2\left[\chi(z)\right]}$, or equivalently,

$$
C_{\mathrm{K}}\left[\chi(z)\right] = \begin{cases}
\cosh\left(\sqrt{\Omega_{\mathrm{K}}}\chi(z)\right) & \Omega_{\mathrm{K}} > 0 \\
\\
1 & \Omega_{\mathrm{K}} = 0 \\
\\
\cos\left(\sqrt{|\Omega_{\mathrm{K}}|}\chi(z)\right) & \Omega_{\mathrm{K}} < 0
\end{cases} .
\tag{3.16}
$$

Note that when $\Omega_{\mathrm{K}} = 0$, equation (3.14) reduces to the well known Euclidean expression,

$$
s(z_1, z_2, \theta) = \sqrt{D_{\mathrm{C}}^2(z_1) + D_{\mathrm{C}}^2(z_2) - 2 D_{\mathrm{C}}(z_1) D_{\mathrm{C}}(z_2) \cos\theta}.
\tag{3.17}
$$

The difference in using equation (3.14), compared to equation (3.17) with the correct form of D_{M}, is of the order of few per-cent when $\Omega_{\mathrm{K}} \neq 0$. This difference translates directly into a shift of the same order on the estimation of the BAO position.

Similarly, using the (generalised) spherical sine rule, we can find a simple expression for $\sin\varphi$, the sine of the angle between the separation vector and the line of sight, which is given by

$$
\sin\varphi = \frac{S_{\mathrm{K}}\left[\chi(z_1)\right] S_{\mathrm{K}}\left[\chi(z_2)\right] \sin\theta}{S_{\mathrm{K}}\left[\chi_{(1,2)}\right] S_{\mathrm{K}}\left[\chi'\right]},
\tag{3.18}
$$

where $D_{\mathrm{H}}\chi'$ is the line-of-sight comoving distance between the observer and the mid-point of the separation vector. Now, we only need $S_{\mathrm{K}}\left[\chi'\right]$ to calculate $\sin\varphi$, and then take[2] $\mu_s = \sqrt{1 - \sin^2\varphi}$. Since $S_{\mathrm{K}}\left[\chi'\right]$ is the median of the spherical triangle defined by z_1, z_2, θ and the observer, using Stewart's theorem we have the relation

$$
C_{\mathrm{K}}\left[\chi'\right] = \frac{C_{\mathrm{K}}\left[\chi(z_1)\right] + C_{\mathrm{K}}\left[\chi(z_2)\right]}{2 C_{\mathrm{K}}\left[\frac{\chi_{(1,2)}}{2}\right]}.
\tag{3.19}
$$

---

[2]Note that we can drop the $\pm$, and take the positive solution, since RSD are symmetric around the line-of-sight.

Note that this relation only works for $\Omega_K \neq 0$, and gives a trivial solution for a flat geometry. In the case when $\Omega_K = 0$, we should use

$$\mu_s = \frac{D_M^2(z_2) - D_M^2(z_1)}{s \sqrt{D_M^2(z_1) + D_M^2(z_2) + 2D_M(z_1)D_M(z_2)\cos\theta}}. \tag{3.20}$$

The difference between deriving μ_s using (3.18) for $\Omega_K \neq 0$, compared to using equation (3.20) with the correct form of D_M for any value of Ω_K, is less than 0.2% for the range of angular and redshift separations we are considering, while the second case is significantly faster to compute. For this reason, we compute μ_s using equation (3.20) in our analysis later on.

When comparing the model for $\omega(\theta)$ with measurements, it is important to take into account the effect of the binning in θ. Measurements are not done over a single angle θ, but correspond to the average over a bin centred on θ with a bin-width $\Delta\theta$. In order to avoid systematic effects such as a shift in the BAO peak determination, we consider in our analysis the bin-averaged angular correlation function, evaluated at the bin θ_i, given by

$$\omega(\theta_i) = \frac{1}{\Delta\Omega_i} \int_{\Delta\Omega_i} d\Omega \ \omega(\theta), \tag{3.21}$$

where $\Delta\Omega_i$ is the solid angle given by

$$\Delta\Omega_i = 2\pi \int_{\theta_i - \Delta\theta/2}^{\theta_i + \Delta\theta/2} d\theta' \sin\theta'. \tag{3.22}$$

3.2.2 Anisotropic clustering in redshift-space

Our first goal is to test the validity and potential of our tomographic clustering analysis. For this reason we use the simple model based on RPT given in equation (2.49). We will explain here how to include the redshift evolution of the clustering signal in the context of this model for the non-linear evolution of the density field.

Unlike the traditional 3D analysis, where it is assumed that evolving quantities, such as galaxy bias, are constant within the sample, in our analysis we need to allow for their evolution. Nevertheless, since each shell is covering a small redshift range, we can neglect the evolution of the density field within a shell, allowing us to evaluate terms such as b_1 and the growth factor $D(z)$ at the mean redshift of the shell $\bar{z}_{\mathrm{shell}}$. We emphasise that this does not mean that the evolution of the whole sample is negligible, it needs to be considered from shell to shell. With this in mind, starting from the linear galaxy bias b_1 in the mock catalogues, since theoretical models favour smooth variations in
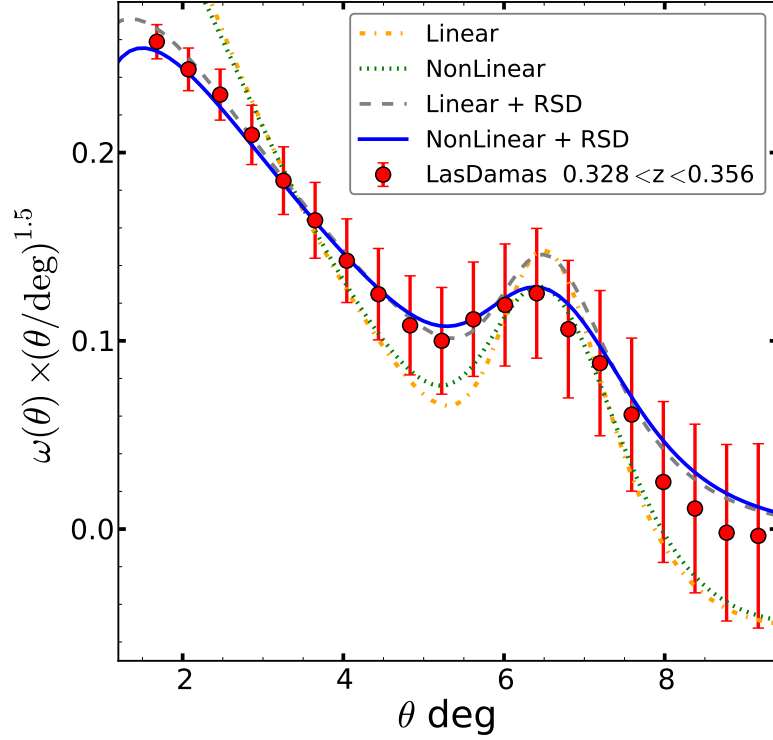
Figure 3.3: The mean $\omega(\theta)$ amplified by $(\theta/deg)^{1.5}$ for LasDamas (red points) in the redshift shell $0.328 < z < 0.356$, and the resulting models obtained including or not non-linear growth and redshift-space distortions (RSD) for the same shell. The green dotted line shows the impact of including non-linear growth effects on the basic linear model (yellow dash-dotted line), while the grey dashed line shows the effect of including RSD in the same linear model. The blue solid line is the final model which includes both effects. The models that do not include RSD are arbitrarily normalised to match the amplitude of the measurements. The error bars correspond to the error in the mean.

b_1 as a function of redshift for galaxy samples with a fixed selection (Baugh et al. 1999; Kauffmann et al. 1999), we assume a linear redshift evolution in which the value of b_1 for a given shell is

$$b_1 = b_* + b' \left(\bar{z}_{\text{shell}} - z_{\text{ref}} \right), \tag{3.23}$$

where now b_* and b' are our free parameters for the linear galaxy bias, and z_{ref} is some reference redshift. We also adopt a redshift evolution for σ_{v} given by

$$\sigma_{\text{v}} = \sigma_{\text{v}}^* \frac{D(\bar{z}_{\text{shell}})}{D(z_{\text{ref}})}, \tag{3.24}$$

where σ_{v}^* is now the free parameter. The amplitude of the linear power spectrum in a given shell is related to that of the reference redshift as

$$P_L(k, \bar{z}_{\text{shell}}) = \left(\frac{D(\bar{z}_{\text{shell}})}{D(z_{\text{ref}})} \right)^2 P_L(k, z_{\text{ref}}), \tag{3.25}$$

which implies that the mode-coupling contribution in equation (2.46), P_{MC}, scales as

$$P_{\text{MC}}(k, \bar{z}_{\text{shell}}) = \left(\frac{D(\bar{z}_{\text{shell}})}{D(z_{\text{ref}})} \right)^4 P_{\text{MC}}(k, z_{\text{ref}}). \tag{3.26}$$

We do not assume any redshift evolution for A_{MC}. With these considerations, the set of free parameters of our model, i.e. $\{b_*, b', \sigma_{\text{v}}^*, A_{\text{MC}}\}$, are fitted to z_{ref}, and the specific value of b_1 and σ_{v} in each shell is given by equation (3.23) and (3.24), relating every shell to a single set of values for these free parameters, which in practice means that we are able to simultaneously describe $P_{NL}(k, \bar{z}_{\text{shell}})$, therefore $\omega(\theta, \bar{z}_{\text{shell}})$, for every shell.

3.2.3 The Covariance Matrix of $\omega(\theta)$

Noise in covariance matrix estimates from mock catalogs propagates to the recovered likelihood of cosmological parameters, leading to an increase in the final errors in those parameters (Dodelson and Schneider, 2013; Taylor et al., 2013; Taylor and Joachimi, 2014; Percival et al., 2014)). These uncertainties, and so their correction, depend on the number of mock catalogs used to estimate the covariance matrix, the number of bins in the data vector and the number of parameters to be constrained using this matrix. Since the set of mock catalogues from LasDamas consists of only 160 realisations, a direct estimation of the full covariance matrix of $\omega(\theta)$ in redshift-shells would be extremely noisy. That is why we use an analytical model instead, following the
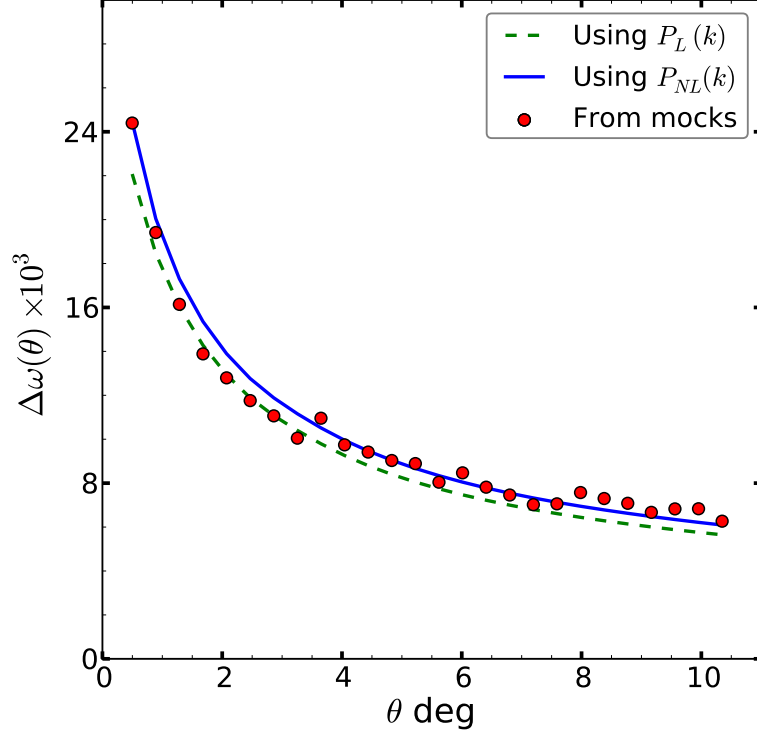
Figure 3.4: The square root of the variance of $\omega(\theta)$ amplified by 10^3, as a function of the angular separation, measured on LasDamas in the redshift shell $0.412 < z < 0.44$ (red points); and the analytical prediction obtained using both, $P_L(k)$ (green dashed line) and $P_{NL}(k)$ (blue solid line), in the modelling.

recipe of Crocce et al. (2011a). Here we briefly describe the more important steps, and refer the reader to their article for a more detailed description.

The angular galaxy power spectrum C_ℓ in redshift-space for a redshift shell is given by

$$C_\ell = \frac{2}{\pi} b^2 D^2(\bar{z}_{\text{shell}}) \int dk \ k^2 P(k) \left(\Psi_\ell(k) + \beta \Psi_\ell^r(k) \right)^2, \qquad (3.27)$$

where Ψ_ℓ and Ψ_ℓ^r are the real- and redshift-space contributions to the kernel function given by

$$\Psi_\ell(k) = \int dz \phi(z) j_\ell(kr), \qquad (3.28)$$
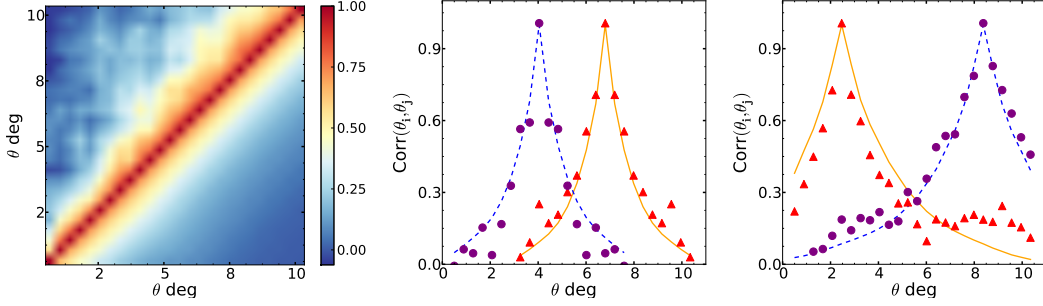
Figure 3.5: Left: correlation matrix of $\omega(\theta)$ measured on LasDamas in the redshift shell $0.412 < z < 0.44$ (upper-triangular) and its analytical prediction using $P_{NL}(k)$ (lower-triangular). Centre: two anti-diagonals of the same matrix, where the purple circles and red triangles are the measurements on LasDamas and the dashed blue and solid yellow lines correspond to the analytical matrix, respectively. Right: two horizontal cuts of the same matrix, following the same symbology as the central panel.

and

$$
\Psi_\ell^r(k) = \int dz \phi(z) \left[\frac{2\ell^2 + 2\ell - 1}{(2\ell + 3)(2\ell - 1)} j_\ell(kr) \right.
$$
$$
- \frac{\ell^2 - \ell}{(2\ell - 1)(2\ell + 1)} j_{\ell-2}(kr)
$$
$$
\left. - \frac{(\ell + 1)(\ell + 2)}{(2\ell + 1)(2\ell + 3)} j_{\ell+2}(kr) \right].
$$

(3.29)

Then, the covariance matrix, $\mathrm{Cov}_{\theta_i \theta_j} = \langle \omega(\theta_i) \omega(\theta_j) \rangle$, can be computed as

$$
\mathrm{Cov}_{\theta_i \theta_j} = \frac{2}{f_{\mathrm{sky}}} \sum_{\ell \geq 2} \frac{2\ell + 1}{(4\pi)^2} L_\ell \left(\cos \theta_i \right) L_\ell \left(\cos \theta_i \right) \left(\mathrm{C}_\ell + \frac{1}{\bar{\mathrm{n}}} \right)^2 ,
$$

(3.30)

f_{sky} is the fraction of the sky observed, and $\bar{n}$ is the mean number of objects per steradian.

As with $\omega(\theta)$, the covariance matrix is also affected by the fact that measurements are done over a bin in θ, reducing the covariance between bins (Cohn 2006, Sánchez et al. 2008, Smith et al. 2008). We consider the bin-averaged covariance matrix obtained from averaging over $\Delta\Omega_i$ and $\Delta\Omega_j$. Each of these integrals only affect the Legendre polynomials evaluated at $\cos\theta_i$ and $\cos\theta_j$

respectively. Defining

$$
\begin{aligned}
\hat{L}_\ell(\cos\theta_\mathrm{i}) =& \frac{1}{\Delta\Omega_\mathrm{i}} \int_{\Delta\Omega_\mathrm{i}} d\Omega L_\ell(\cos\theta_\mathrm{i}) \\
=& \frac{2\pi}{\Delta\Omega_i} \frac{1}{2\ell+1} \left[L_{\ell-1}\left(\cos(\theta_\mathrm{i}+\Delta\theta/2)\right) \right. \\
& - L_{\ell+1}\left(\cos(\theta_\mathrm{i}+\Delta\theta/2)\right) - L_{\ell-1}\left(\cos(\theta_\mathrm{i}-\Delta\theta/2)\right) \\
& \left. + L_{\ell+1}\left(\cos(\theta_\mathrm{i}-\Delta\theta/2)\right) \right],
\end{aligned}
\tag{3.31}
$$

the bin-averaged covariance matrix is then given by

$$
\mathrm{Cov}_{\theta_\mathrm{i}\theta_\mathrm{j}} = \frac{2}{f_\mathrm{sky}} \sum_{\ell\geq 2} \frac{2\ell+1}{(4\pi)^2} \hat{L}_\ell\left(\cos\theta_\mathrm{i}\right) \hat{L}_\ell\left(\cos\theta_\mathrm{j}\right) \left(\mathrm{C}_\ell + \frac{1}{\bar{\mathrm{n}}} \right)^2 .
\tag{3.32}
$$

We tested this model for the covariance matrix, using in equation (3.27) both $P_L(k)$ and $P_{NL}(k)$ with the best-fitting values of $\{b_*, b'\}$, and $\{\sigma_\mathrm{v}^*, A_\mathrm{MC}\}$ in the non-linear case, for the cosmology of LasDamas, and compared the results with the estimated matrix from the mock catalogues. figure 3.4 shows the square root of the diagonal elements of the covariance matrix for the shell within $0.412 < z < 0.44$, which is the dispersion of $\omega(\theta)$ in this shell, estimated from the mock catalogues (red points), the prediction using the linear power spectrum (green dashed line), and the prediction using the non-linear power spectrum (blue solid line). It can be seen that both approaches give a very good description of the variance of the angular correlation function for the scales in which we are interested. Hereafter we will only use the non-linear approach.

The left panel of figure 3.5 shows the reduced covariance matrix, or correlation matrix, defined as

$$
\mathrm{Corr}_{\theta_\mathrm{i}\theta_\mathrm{j}} = \frac{\mathrm{Cov}_{\theta_\mathrm{i}\theta_\mathrm{j}}}{\sqrt{\mathrm{Cov}_{\theta_\mathrm{i}\theta_\mathrm{i}} \mathrm{Cov}_{\theta_\mathrm{j}\theta_\mathrm{j}}}},
\tag{3.33}
$$

for the same shell as figure 3.4, where the upper-triangular part is the estimation from the mock catalogues and the lower-triangular part corresponds to the theoretical model. The central panel shows two anti-diagonals of the correlation matrix estimated from the mock catalogues (points), and of the predicted matrix (solid lines). The same symbols apply for the right panel, where two horizontal cuts of these matrices are shown.

We computed the theoretical matrix for every shell using $P_{NL}(k)$, and used them to test our technique.
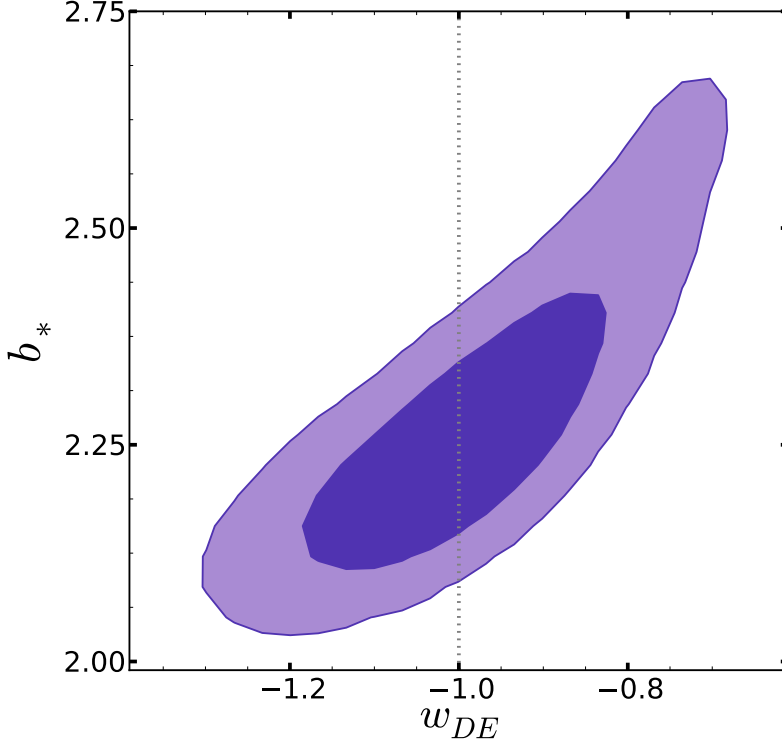
Figure 3.6: The marginalised 68 and 95 per cent confidence levels in the $w_{DE} - b_*$ plane for our test. Here we find $w_{DE} = -0.99 \pm 0.12$ in excellent agreement with the correct value used to construct the mock catalogues (dotted line).

3.2.4 Testing the model for $\omega(\theta)$

In order to test the model for the angular correlation function, we implemented a Markov chain Monte Carlo (MCMC) analysis taking the same ΛCDM cosmology of LasDamas (see Table 3.1) and exploring the following parameter space:

$$\mathbb{P}_{\text{test}} \equiv \{w_{DE}, b_*, b', \sigma_v^*, A_{\text{MC}}\}, \tag{3.34}$$

where w_{DE} is the constant dark energy equation of state parameter, and the rest are the free parameters of our model for $\omega(\theta)$. We estimate the likelihood function as $\mathcal{L}(\mathbf{P}_{\text{test}}) \propto \exp\left(-\chi^2(\mathbf{P}_{\text{test}})/2\right)$, where

$$\chi^2\left(\mathbf{P}_{\text{test}}\right) = \sum_{\text{shells}} (\mathbf{M}_i - \mathbf{D}_i)^T \widehat{\mathsf{Cov}_i}^{-1} (\mathbf{M}_i - \mathbf{D}_i), \tag{3.35}$$

$\mathbf{P}_{\text{test}}$ is a vector with the parameter values, $\mathbf{M}_i$ is the model of the shell i given $\mathbf{P}_{\text{test}}$, $\mathbf{D}_i$ is the mean $\omega(\theta)$ measured in the shell i, and $\widehat{\mathsf{Cov}_i}$ is the corresponding covariance matrix for the same shell divided by $\sqrt{N_{\text{mocks}}}$, which

represents the covariance matrix for a volume equal to the total volume of the ensemble, allowing us to detect any bias in the constraints. To compute the models for $\omega(\theta)$, the linear power spectrum $P_L(k)$ is calculated using CAMB (Lewis et al., 2000).

The goal here is to test if we are able to recover the correct value of w_{DE} using this model and the measurements made on LasDamas. Since our model does not have any free parameter to adjust the position of the BAO peak on $\omega(\theta)$, and moreover, it reproduces this angular scale simultaneously for every shell, recovering the correct value of w_{DE} basically means that we are able to correctly measure the distance to every single redshift-shell, describing the expansion history of the Universe.

Figure 3.6 shows the resulting marginalised constraints in the $w_{DE} - b_*$ plane, where the contours are the 68 and 95 per cent confidence levels. For this test we found $w_{DE} = -0.99 \pm 0.12$, which is in excellent agreement with the true value of LasDamas, showing that this technique is able to extract unbiased constraints on w_{DE}.

3.3 A test case: Forecast for BOSS

We tested the implications of applying this technique to the final SDSS-III BOSS catalogue (DR12), in combination with Planck, for three different flat cosmological models, and compared this with what would result from the combination of Planck and isotropic BAO measurements post-reconstruction on BOSS (CMASS and LOWZ). To do so, we characterised the BOSS catalogue by assuming the best fit of the base ΛCDM model from Planck plus WMAP polarisation (WP) as our true cosmology (Planck Collaboration XVI, 2014), an area in the sky of 10000 deg^2, a constant $n(z) = 3 \times 10^{-4} h^3 \text{Mpc}^{-3}$, and a galaxy bias based on Fry (1996) given by

$$b_1 = 1 + \frac{(b_0 - 1)}{D(\bar{z}_{\text{shell}})}, \tag{3.36}$$

which describes its redshift evolution for the CMASS sample (Guo et al., 2013). Also, since the effect of massive neutrinos is not negligible in the Hubble expansion rate $H(a)$, we adopted the exact treatment in Komatsu et al. (2011) given by

$$
\begin{aligned}
H(a) = H_0 \Bigg(& \frac{\Omega_{\text{b}} + \Omega_{\text{cdm}}}{a^3} + \frac{\Omega_\gamma}{a^4} \left(1 + 0.2271 N_{\text{eff}} f(m_\nu a/T_{\nu 0})\right) \\
& + \frac{\Omega_{\text{k}}}{a^2} + \frac{\Omega_\Lambda}{a^{3(1+w_{DE}(a))}} \Bigg),
\end{aligned} \tag{3.37}
$$

where a is the scale factor, $m_\nu a/T_{\nu 0} = (1.87 \times 10^5/(1+z))\,\Omega_\nu h^2$, the photon density parameter is $\Omega_\gamma = 2.469 \times 10^{-5} h^{-2}$ for $T_{\rm cmb} = 2.725{\rm K}$, and $f(y)$ can be approximated by the fitting formula

$$f(y) \approx \left(1 + (Ay)^p\right)^{\frac{1}{p}}, \qquad (3.38)$$

where $A = 180\zeta(3)/(7\pi^4)$, $\zeta(3) \simeq 1.202$ is the Riemann zeta function, and $p = 1.83$.

Using the model for $\omega(\theta)$ and its covariance matrix described in §3.2.1 and §3.2.3 respectively, we constructed a synthetic dataset consisting of 16 shells of width $\Delta z = 0.025$, ranging from $z = 0.2$ up to $z = 0.6$. The fiducial values for the free parameters of the model are $b_0 = 1.55$, $\sigma_{\rm v}^* = 4.29$, and $A_{\rm MC} = 1.5$. The result of this synthetic dataset can be seen in figure 3.7.

For the CMB data we used the distance priors based on Wang and Wang (2013) which summarises the CMB information from Planck in a set of parameters and its covariance matrix, where we have included the spectral amplitude $A_{\rm s}$. The resulting set is

$$\mathbb{P}_{\rm CMB} \equiv \{\ell_A, R, \omega_{\rm b}, A_{\rm s}, n_{\rm s}\}, \qquad (3.39)$$

where in practice the first 2 parameters, the CMB angular scale ℓ_A and the shift parameter R, are derived from the other explored parameters in our analysis, which are described below in this section, following the equations in Wang and Wang (2013).

To reproduce the isotropic BAO measurements post-reconstruction on BOSS, for our fiducial cosmology we took the ratio

$$x(z_m) = \frac{D_{\rm V}(z_m)}{r_{\rm s}(z_d)}, \qquad (3.40)$$

at $z_m^1 = 0.32$ with an error of 2% for LOWZ and at $z_m^2 = 0.57$ with an error of 1% for CMASS (Anderson et al., 2014a), where $D_{\rm V}(z)$ is the spherically-averaged distance, defined in equation (2.22), from the mean redshift z_m.

With these three ingredients we performed an MCMC analysis with the aim of forecasting the expected accuracy of constraining cosmological parameters, by applying this technique to the final BOSS catalogue. The base model for the analysis is the flat ΛCDM model, where baryons, cold dark matter (CDM) and dark energy (vacuum energy or a cosmological constant Λ) are the main contributors to the total energy of the Universe; and with Gaussian, adiabatic primordial scalar density fluctuations following a power-law spectrum for the amplitudes in Fourier space. This model can be characterised by the following parameter space:

$$\mathbb{P}_{\Lambda{\rm CDM}} \equiv \{\omega_{\rm b}, \omega_{\rm cdm}, \omega_{\rm de}, A_{\rm s}, n_{\rm s}\}, \qquad (3.41)$$
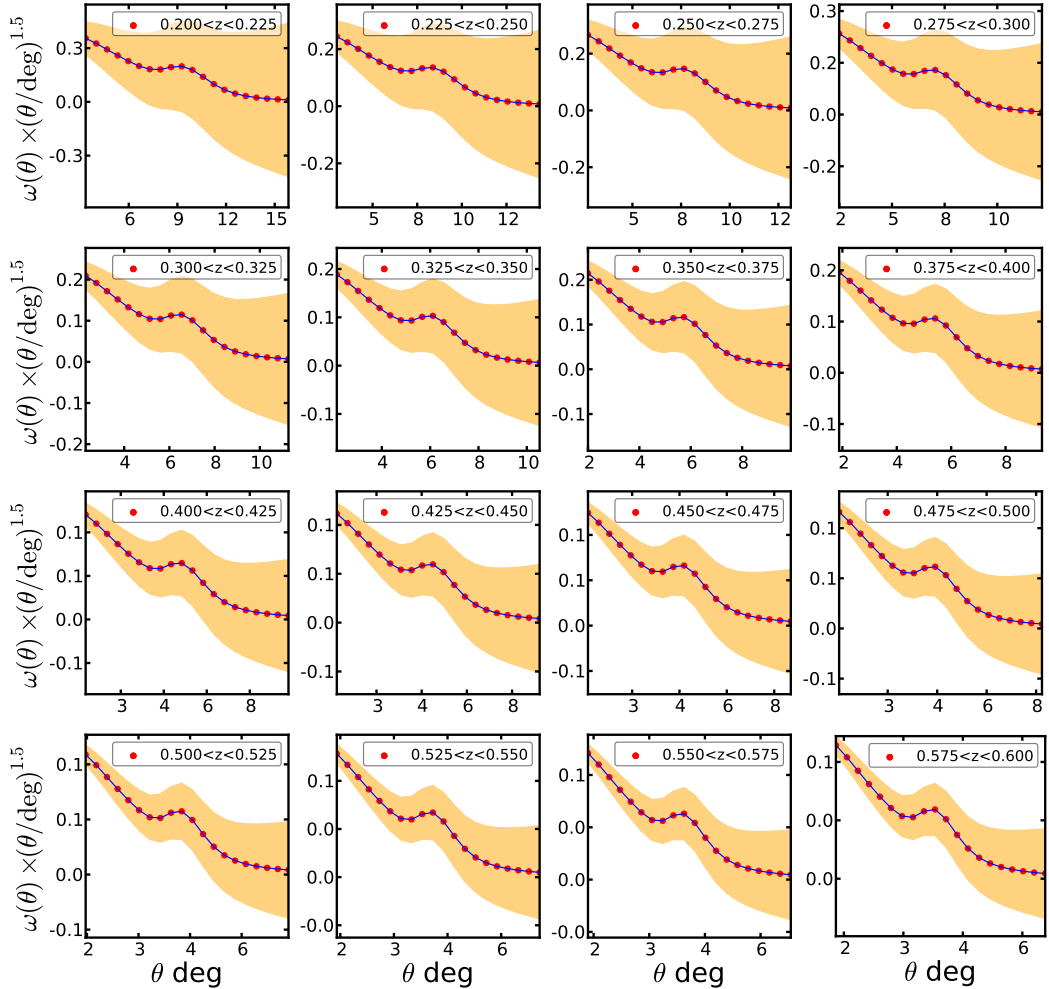
Figure 3.7: Synthetic dataset constructed with the models of $\omega(\theta)$ and its covariance matrix, taking the best-fit ΛCDM cosmology from Planck. It consists of 16 redshift shells of $\Delta z = 0.025$ within the redshift range $0.2 < z < 0.6$. We used this dataset to forecast the results of combining Planck and the technique discussed in this paper applied to the final BOSS. We have characterised the BOSS catalogue by assuming an area in the sky of 10000 deg^2, a constant $n(z) = 3 \times 10^{-4} h^3 \text{Mpc}^{-3}$, and a galaxy bias based on Fry (1996).

where ω_{b}, ω_{cdm} and ω_{de} are the baryon, cold dark matter and dark energy densities respectively; here $\omega_X \equiv \Omega_X h^2$. The primordial power spectrum is characterised by its amplitude A_{s} and its spectral index n_{s}, both defined at the pivot wavenumber $k_p = 0.05\,\mathrm{Mpc}^{-1}$. We also extended the base model allowing variations in the dark energy equation of state parameter w_{DE}, considering $w_{DE}(a) = w_0$ constant in time, and also a time dependence given by the standard linear parametrisation of Chevallier and Polarski (2001) and Linder (2003)

$$w_{DE}(a) = w_0 + w_a(1 - a). \tag{3.42}$$

Then, the two cases of the extended parameter space are

$$\mathbb{P}_{w\mathrm{CDM}} \equiv \{\omega_{\mathrm{b}}, \omega_{\mathrm{cdm}}, \omega_{\mathrm{de}}, A_{\mathrm{s}}, n_{\mathrm{s}}, w_0[, w_a]\}, \tag{3.43}$$

where $[, w_a]$ denotes the variation (or not) of w_a. It is also necessary to include the free parameters of our model with the sets in equation (3.41) and (3.43), in order to compare the constraints obtained from the use of $\omega(\theta)$ and the other dataset combinations. We consider a case where we use the correct bias evolution in equation (3.36), treating b_0 as a free parameter, giving us three nuisance parameters for our model (b_0, A_{MC} and σ_{v}^*), and a second case where we do not assume that we know the functional form of the bias evolution, using the linear model in equation (3.23) giving us four nuisance parameters for our model for $\omega(\theta)$ (b_*, b', A_{MC} and σ_{v}^*). We do not consider more flexible parametrisations for the bias evolution, since it is expected that the galaxy bias has a smooth variation as a function of redshift, specially for passively evolving galaxy populations such as LRGs (Baugh et al. 1999; Kauffmann et al. 1999; Almeida et al. 2008).

We estimate the likelihoods as in §3.2.4, computing the χ^2 for $\omega(\theta)$ as in equation (3.35) using the full covariance matrix, and where the argument vector now is $\mathbf{P}$ which has values of the parameter-space corresponding to the cosmology being tested. The χ^2 for the CMB is given by

$$\chi^2_{\mathrm{cmb}}(\mathbf{P}) = \left(\mathbf{V}_{\mathrm{cmb}} - \mathbf{V}_{\mathrm{cmb}}^f\right)^T \mathsf{Cov}_{\mathrm{cmb}}^{-1} \left(\mathbf{V}_{\mathrm{cmb}} - \mathbf{V}_{\mathrm{cmb}}^f\right), \tag{3.44}$$

where $\mathbf{V}_{\mathrm{cmb}}$ is a vector with the values of $\mathbb{P}_{\mathrm{CMB}}$ as a function of $\mathbf{P}$, $\mathbf{V}_{\mathrm{cmb}}^f$ is the vector with the correct values for our fiducial cosmology, and $\mathsf{Cov}_{\mathrm{cmb}}$ is the covariance matrix for these CMB parameters. For the BAOs, we calculate the χ^2 as follows,

$$\chi^2_{\mathrm{bao}} = \left(\frac{x(z_m^1) - x^f(z_m^1)}{\sigma_{z_m^1}}\right)^2 + \left(\frac{x(z_m^2) - x^f(z_m^2)}{\sigma_{z_m^2}}\right)^2 \tag{3.45}$$
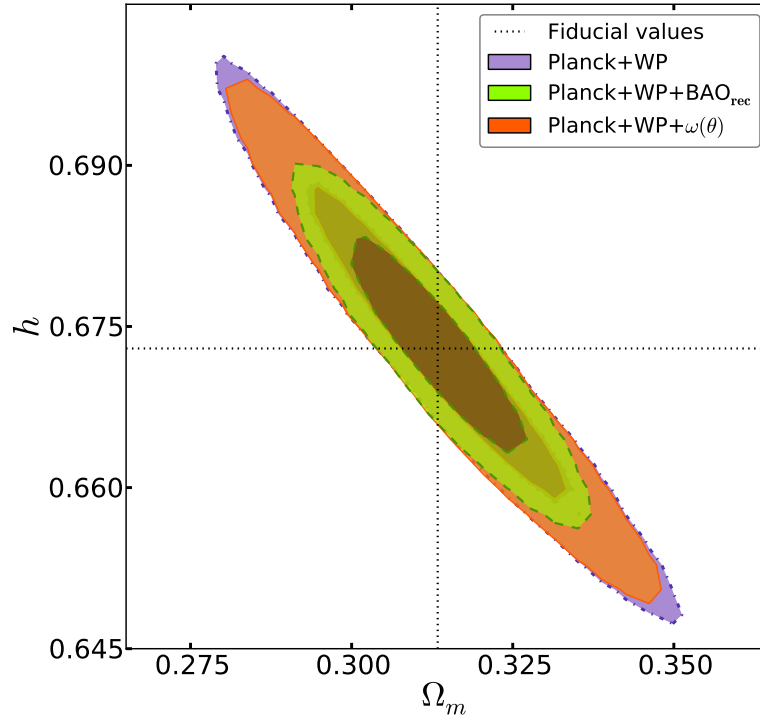
Figure 3.8: The marginalised 68 and 95 per cent confidence levels in the $\Omega_M - h$ plane for the base ΛCDM model case. The dash-dotted lines (purple contours) correspond to the constraints derived from the use of Planck+WP only. The dashed lines (green contours) are the constraints obtained by combining Planck+WP and BAO measurements post-reconstruction, while the solid lines (orange contours) are those derived from the combination of Planck+WP and $\omega(\theta)$ without any reconstruction. The dotted lines correspond to the fiducial values assumed to make our forecast.

where $x(z_m^i)$ is the expression in equation (3.40) at z_m^i as a function of $\mathbf{P}$, $x^f(z_m^i)$ is the same expression at z_m^i evaluated in our fiducial cosmology, and $\sigma_{z_m^i}$ is the assumed error for the BAO measurement at z_m^i.

In the case of the base ΛCDM model, figure 3.8 shows the marginalised constraints in the $\Omega_M - h$ plane for the different combinations of datasets, where the contours correspond to the 68 and 95 per cent confidence levels. From the combination of Planck+WP and $\omega(\theta)$ we find a mean value of $\Omega_M = 0.314 \pm 0.013$ (68%C.L.) and $h = 0.673 \pm 0.010$ (68%C.L.) for the correct bias model, with negligible variation for the linear bias model ($< 3\%$), in remarkable agreement with the fiducial cosmology, tightening the constraints derived from the CMB only. Although, it can be seen that, in this case, the combination of Planck+WP and BAO measurements post-reconstruction does
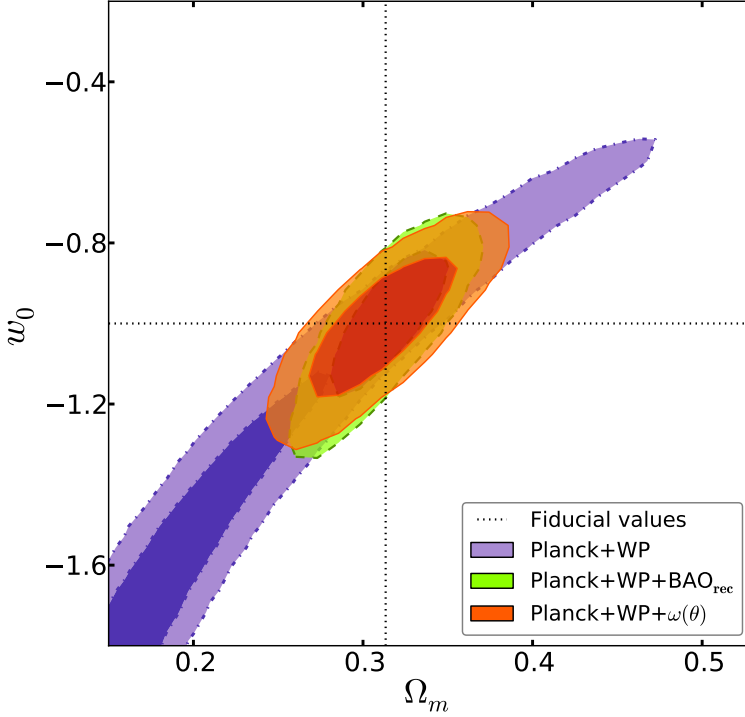
Figure 3.9: The marginalised 68 and 95 per cent confidence levels on the $\Omega_M - w_0$ plane for the extended ΛCDM model case with constant $w_{DE} = w_0$. The dash-dotted lines (purple contours) correspond to the constraints derived from the use of Planck+WP only. The dashed lines (green contours) are the constraints obtained by combining Planck+WP and BAO measurements post-reconstruction, while the solid lines (orange contours) are those derived from the combination of Planck+WP and $\omega(\theta)$ without any reconstruction. The dotted lines correspond to the fiducial values assumed to make our forecast.

somewhat better. Nevertheless, once we allow w_{DE} to take a constant value different from -1, the constraints from combining Planck+WP and $\omega(\theta)$ are now as good as those obtained from the combination of Planck+WP and BAO measurements post-reconstruction. This can be seen in figure 3.9, where the contours correspond to the marginalised constraints in the $\Omega_M - w_0$ plane showing the 68 and 95 per cent confidence levels. In this case we find a mean value of $\Omega_M = 0.311\pm0.028$ (68%C.L.) and $w_0 = -1.00\pm0.11$ (68%C.L.) for the correct bias model, and $\Omega_M = 0.308 \pm 0.032$ (68%C.L.) and $w_0 = -1.01 \pm 0.14$ (68%C.L.) for the linear bias model, again in excellent agreement with our true cosmology.

If we now allow w_{DE} to vary over time following the parametrisation given in equation (3.42), the constraints obtained from the combination of

Planck+WP and $\omega(\theta)$ in this case are more accurate than those obtained from combining Planck+WP and BAOs. Figure 3.10 shows the 68 and 95 per cent confidence level marginalised constraints in the $w_0 - w_a$ plane for the different combinations of datasets, where this accuracy improvement can be seen. From Planck+WP+$\omega(\theta)$ we find a mean value of $w_0 = -1.03 \pm 0.25$ (68%C.L.) and $w_a = 0.008^{+0.76}_{-0.74}$ (68%C.L.) for the correct bias model, and $w_0 = -1.05 \pm .33$ (68%C.L.) and $w_a = 0.015^{+0.91}_{-0.89}$ (68%C.L.) for the linear bias model, again in perfect agreement with our fiducial cosmology just like the two previous cases. To quantify the constraints obtained in this case using different dataset combinations, we used the Figure-of-Merit (FoM) defined as (Albrecht et al. 2006; Wang 2008)

$$\text{FoM} = \det \left[\text{Cov}(\text{w}_0, \text{w}_\text{a}) \right]^{-1/2}, \qquad (3.46)$$

where $\text{Cov}(\text{w}_0, \text{w}_\text{a})$ is the 2×2 covariance matrix of w_0 and w_a. The higher the FoM, the more accurate are the constraints made by a particular dataset combination. From the combination of Planck+WP and BAOs the FoM= 9.17, while from the combination of Planck+WP+$\omega(\theta)$ we obtain a value of 10.54, increasing the FoM by 15% for the correct bias model. Using the linear bias model, we obtain a FoM of 8.24, 10% lower compared to the BAO post-reconstruction technique.

What can be concluded from these tests is: (i) The choice of different models for the galaxy bias evolution has an impact on the accuracy with which we can constrain cosmological parameters, but a sensible choice can still result in unbiased constraints; (ii) The more freedom we allow for the expansion history in a given model, the better performance this tomographic approach has compared to the traditional BAO technique. This can be explained mainly by two factors. First, while BAOs only take into account the position of the BAO feature measuring the quantity in equation (3.40), the full shape of the correlation function is also sensitive to other combinations of cosmological parameters, such as ω_b and ω_cdm. Secondly, as we mentioned in §3.1.2, measuring $\omega(\theta)$ in several redshift bins basically gives several measurements of $\theta_s(z)$, constraining the ratio at which the angular diameter distance can evolve over the redshift range being tested. Then if we include the extra information of the full shape of $\omega(\theta)$ mentioned before, we end up with a very powerful tool to probe the expansion history of the Universe.
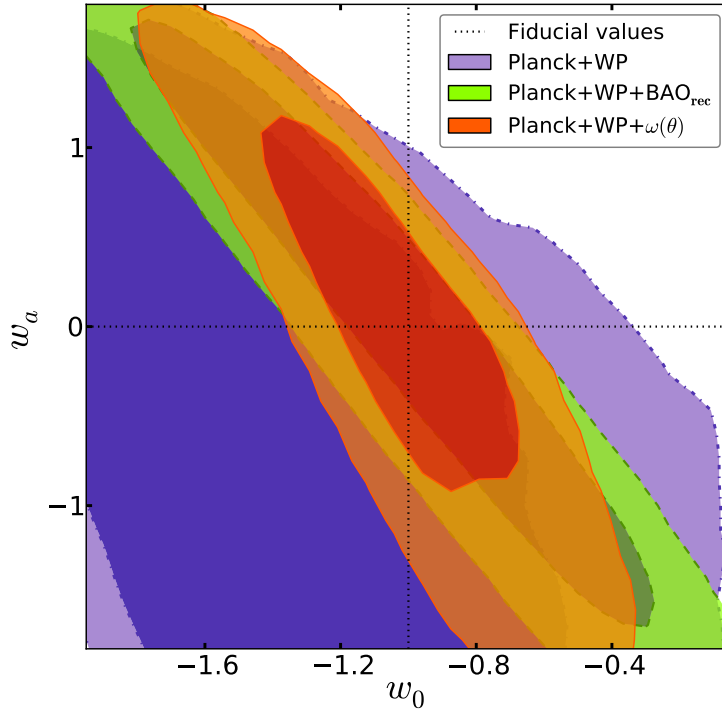
Figure 3.10: The marginalised 68 and 95 per cent confidence levels in the $w_0 - w_a$ plane for the extended ΛCDM model case, with a time-dependent w_{DE} parametrised as in equation (3.42). The dash-dotted lines (purple contours) correspond to the constraints derived from the use of Planck+WP only. The dashed lines (green contours) are the constraints obtained by combining Planck+WP and BAO measurements post-reconstruction, while the solid lines (orange contours) are those derived from the combination of Planck+WP and $\omega(\theta)$ without any reconstruction. The dotted lines correspond to the fiducial values assumed to make our forecast.

Chapter 4

Clustering Tomography on the final BOSS galaxy catalogue

4.1 The Data

4.1.1 The Baryon Oscillation Spectroscopic Survey

For our galaxy clustering measurements we use the combined sample of BOSS (Dawson et al., 2013) from the final SDSS-III (Eisenstein et al., 2011) data release (DR12; Alam et al., 2015), which consists of the combination of the LOWZ and CMASS samples, used separately in previous studies (e.g. Anderson et al., 2014b; Sánchez et al., 2013, 2014; Beutler et al., 2014; Reid et al., 2010; Samushia et al., 2014; Cuesta et al., 2016), adding up to a sample of over a million galaxies. BOSS galaxies were selected for spectroscopic follow up on the basis of the multi-colour SDSS observations (Gunn et al., 2006), covering the redshift range $0.15 < z < 0.75$ over an area of ~ 10000 square degrees. The motivation for the target selection and the algorithms used are described in Reid et al. (2016). For each target, spectra were obtained using the double-armed BOSS spectrographs (Smee et al., 2013), in order to extract redshifts applying a template-fitting method described in Bolton et al. (2012).

We used the estimator by Landy and Szalay (1993) to estimate the angular auto-correlation function of a given redshift shell (denoted now explicitly with p) as

$$\omega^{(p,p)}(\theta_i) = \frac{\mathrm{DD}_i^{(p,p)} - 2\mathrm{DR}_i^{(p,p)} + \mathrm{RR}_i^{(p,p)}}{\mathrm{RR}_i^{(p,p)}}, \qquad (4.1)$$

where DD_i, DR_i and RR_i are the data-data, data-random and random-random pair counts in the i-th bin in θ, respectively. Similarly, we estimate the angular

Cosmological constant density parameter	Ω_Λ	0.69
Matter density parameter	Ω_M	0.31
Baryonic density parameter	Ω_b	0.048
Dark energy equation of state	w_{DE}	-1.0
Hubble constant $\left(\mathrm{km\ s^{-1}\,Mpc^{-1}}\right)$	H_0	67.6

Table 4.1: Cosmological parameters of the BOSS fiducial ΛCDM cosmology.

cross-correlation function between the redshift shells p and q as

$$\omega^{(p,q)}(\theta_i) = \frac{\mathrm{DD}_i^{(p,q)} - \mathrm{DR}_i^{(p,q)} - \mathrm{DR}_i^{(q,p)} + \mathrm{RR}_i^{(p,q)}}{\mathrm{RR}_i^{(p,q)}}. \qquad (4.2)$$

When computing these pair counts, we apply a series of angular weights to account for observational systematic-effects, such as redshift failures, fibre collisions, local stellar density and seeing. These weights are described in detail in Ross et al. (in prep.). Each correlation function is measured to a maximum angular separation $\theta_\mathrm{max}(\bar{z}^{(p,q)})$ corresponding to a physical separation of ~ 180 Mpc/h at the mean redshift of the shell, $\bar{z}^{(p,q)}$, in the fiducial BOSS DR12 cosmology (see table 4.1) used in analyses based on this galaxy sample (Alam et al., in prep; Beutler et al., in prep.; Grieb et al., in prep.; Ross et al., in prep.; Sánchez et al., in prep.). We emphasise that the choice of θ_max is arbitrary and has no other impact on our angular clustering measurements.

For illustration, figure 4.1 shows two measurements on the combined sample (symbols), one auto-correlation function and one cross-correlation function in the top and bottom panels respectively, for different redshift shells (see key). The blue solid lines correspond to the best-fitting prediction of the model described in §4.2.1 and §4.2.2, assuming the best-fitting ΛCDM model from the latest CMB measurements made by the *Planck* satellite (Planck Collaboration XIII, 2015).

To test our models for the angular correlation function and its full covariance matrix, we use a set of 1000 MD-PATCHY mock catalogues (Kitaura et al., 2016), which are designed to match the characteristics of the final BOSS galaxy sample, following its angular and radial selection function. These mock catalogues also include light-cone effects, such as galaxy bias and velocity field redshift-evolution, a crucial characteristic for this analysis.
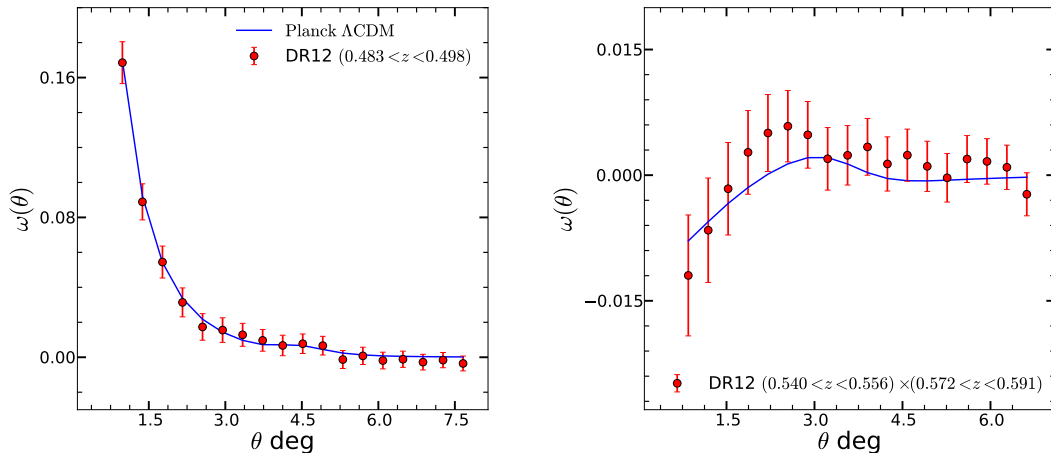
Figure 4.1: An auto-correlation function (left) and a cross-correlation function (right) between different redshift bins (see key) from the final BOSS galaxy sample. Measurements are shown by red symbols, while the blue line shows the prediction of our model described in §4.2.1 and §4.2.2, assuming the best-fitting ΛCDM cosmology from the CMB temperature-anisotropy power spectrum as measured by the *Planck* satellite.

4.1.2 Additional data sets

In order to improve the cosmological constraints obtained in this analysis, in §4.3 and §4.4 we combine the information contained in the full shape of $\omega(\theta)$ and its redshift evolution with additional data sets.

We use high-ℓ ($\ell = 50 - 2500$) CMB temperature plus the low-ℓ ($\ell = 2-29$) temperature+polarisation power spectrum, from the latest data release of the *Planck* satellite, corresponding to the "*Planck* TT+lowP" case in Planck Collaboration XIII (2015). We refer to this data set simply as "Planck", and to its combination with our $\omega(\theta)$ measurements on BOSS as "Planck + $\omega(\theta)$".

In addition, we use the luminosity-distance relation information from Type Ia supernova (SNIa). To this end, we use the *joint light-curve analysis* compilation (JLA; Betoule et al., 2014), which includes SNIa data from the full SDSS-II (Frieman et al., 2008; Kessler et al., 2009; Campbell et al., 2013) survey and the compilation in Conley et al. (2011), comprising data from the Supernova Legacy Survey (Astier et al., 2006; Sullivan et al., 2011), the *Hubble* space telescope (Riess et al., 2007; Suzuki et al., 2012) and several nearby experiments. We only use this data set in combination with the other two, thus whenever it is included, this is referred to as "Planck + $\omega(\theta)$ + SNIa".

4.2   Methodology

4.2.1   Modelling $\omega(\theta)$

We follow the same modelling as in §3.2.1, extended for the inclusion of cross-correlations between different shells. Given the redshift shells p and q, the angular auto-/cross-correlation function is given by,

$$\omega^{(p,q)}(\theta) = \int dz_1 \phi^p(z_1) \int dz_2 \phi^q(z_2)\xi(s,\mu_s), \qquad (4.3)$$

where $\phi^p(z)$ and $\phi^q(z)$ are the normalised selection functions of the shells p and q respectively, and $\xi(s,\mu_s)$ is the full 2D anisotropic spatial correlation function at the mean redshift $\bar{z}^{(p,q)}$.

4.2.2   Modelling the anisotropic galaxy clustering in BOSS

To analyse the final BOSS galaxy sample, we use the gRPT-based modelling of $\xi(s,\mu_s)$, including bias and RSD, which is described in §2.7.2. Similar to what we do in chapter 3, in order to correctly model $\omega^{(p,q)}(\theta)$ we need to compute the line-of-sight projection of $\xi(s,\mu_s; \bar{z}^{(p,q)})$ as in equation (4.3). For this, we need to consider that the galaxy bias evolves with redshift, as well as the signal of the RSD and the non-linear growth of structures. In practice, this means that the nuisance parameters of our model, $\{b_1, b_2, \gamma_3^-, a_{\mathrm{vir}}\}$, will have different values at different redshifts. We also need to linearly evolve the input (linear) $P(k)$ with redshift as in equation (3.25).

For the linear galaxy bias parameter b_1, we test three well motivated models. The vast majority of galaxies in BOSS are old passively-evolving galaxies (Leauthaud et al., 2016), this motivates the use of the model in Fry (1996) (hereafter F96), given by

$$b_1\left(\bar{z}^{(p,q)}\right) = 1 + (b_1 - 1)\frac{D(z_{\mathrm{ref}})}{D\left(\bar{z}^{(p,q)}\right)}. \qquad (4.4)$$

On the other hand, it has been shown empirically that the clustering amplitude of CMASS galaxies does not evolve significantly with redshift (Reid et al., 2014; Saito et al., 2015). If the amplitude of the matter density fluctuations evolves (in the linear regime) with the linear growth factor, then the galaxy bias needs to evolve as

$$b_1\left(\bar{z}^{(p,q)}\right) = b_1\frac{D(z_{\mathrm{ref}})}{D\left(\bar{z}^{(p,q)}\right)}, \qquad (4.5)$$

in order to keep the amplitude of the galaxy-clustering signal constant. This model is referred to as the constant galaxy-clustering model (hereafter CGC).

These two models relate the evolution of the galaxy bias with the linear growth factor, which could lead to biases in the cosmological parameters if the models are not correct. For this reason, we also test a simple linear model that does not depend on the cosmology, given by

$$b_1\left(\bar{z}^{(p,q)}\right) = b_1 + b'\left(\bar{z}^{(p,q)} - z_{\mathrm{ref}}\right), \qquad (4.6)$$

where b' is an extra nuisance parameter to be fit when using this model. We do not expect a redshift dependence of the quadratic bias parameter b_2.

The redshift evolution for the non-local bias parameter is given by

$$\gamma_3^-\left(\bar{z}^{(p,q)}\right) = \gamma_3^- \frac{D(z_{\mathrm{ref}})}{D\left(\bar{z}^{(p,q)}\right)}, \qquad (4.7)$$

while a_{vir}, the parameter accounting for the kurtosis of the velocity distribution within virialised structures, evolves with redshift as

$$a_{\mathrm{vir}}\left(\bar{z}^{(p,q)}\right) = a_{\mathrm{vir}}\left(\frac{D\left(\bar{z}^{(p,q)}\right)}{D(z_{\mathrm{ref}})}\right)^2. \qquad (4.8)$$

Figure 4.2 shows a comparison between the best-fitting model (blue solid line) and the mean of the 1000 MD-PATCHY (symbols). Here we use the bias model in eq. (4.4), and the true underlying linear matter power spectrum $P(k)$. The upper panel shows one of the auto-correlation functions measured, and the lower panel a cross-correlation function. In both panels the colour band shows the dispersion corresponding to a single realisation.

4.2.3   Analytical model for the full covariance matrix

As we did for the angular correlation function, we extend the model for the full covariance matrix of our ensemble of $\omega(\theta)$ measurements, including cross-correlations between redshift shells and the covariance between any two different measurements. Assuming that the density field is a Gaussian random field, the full bin-averaged covariance matrix can be obtained as

$$\mathrm{Cov}_{i,j}^{(m,n),(p,q)} = \sum_{\ell,\ell'\geq 2}\left(\frac{2\ell+1}{4\pi}\right)^2 \hat{L}_\ell\left(\cos\theta_i\right)\hat{L}_{\ell'}\left(\cos\theta_j\right)\mathrm{Cov}_{\ell,\ell'}^{(m,n),(p,q)}, \qquad (4.9)$$

where $\{m,n,p,q\}$ denote for every redshift shell in our configuration, $L_\ell\left(\cos\theta_i\right)$ is the bin-averaged Legendre polynomial of ℓ-th order in the solid angle $\Delta\Omega_i$
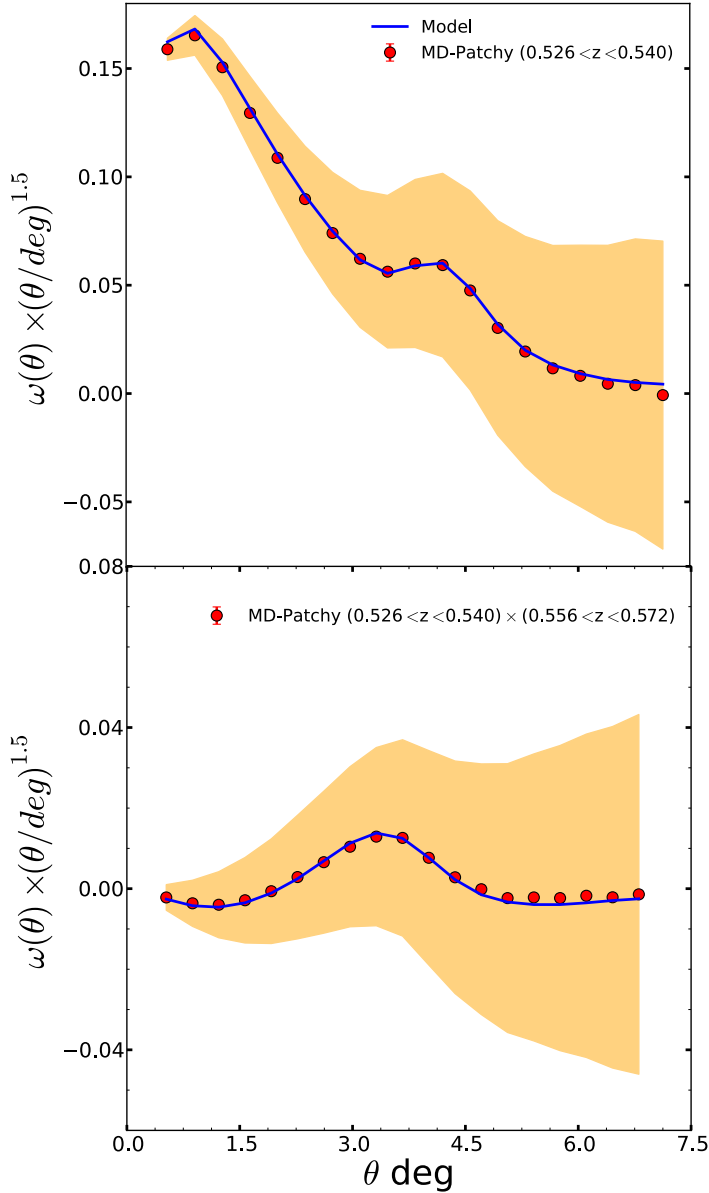
Figure 4.2: Comparison between the best-fitting model (blue solid line) and the mean of the 1000 MD-PATCHY (symbols). The top panel shows an auto-correlation function, and the bottom panel a cross-correlation function. In both panels the colour band shows the dispersion corresponding to a single realisation.

defined by the angular bin θ_i, and $\mathrm{Cov}_{\ell,\ell'}^{(m,n),(p,q)}$ is the covariance matrix of the angular power spectrum C_ℓ, given by

$$\mathrm{Cov}_{\ell,\ell'}^{(m,n),(p,q)} = \delta_{\ell\ell'} \frac{\hat{C}_\ell^{(m,p)}\hat{C}_\ell^{(n,q)} + \hat{C}_\ell^{(m,q)}\hat{C}_\ell^{(n,p)}}{f_{\mathrm{sky}}(2\ell+1)}. \tag{4.10}$$

Here, δ_{xy} is the kronecker delta function, and $\hat{C}_\ell$ is the observed angular galaxy-power-spectrum

$$\hat{C}_\ell^{(p,q)} = C_\ell^{(p,q)} + \frac{\delta_{pq}}{\bar{n}^p}, \tag{4.11}$$

where $\bar{n}^p$ is the mean number of galaxies per steradian in the redshift shell p.

Assuming the BOSS fiducial cosmology, we compute the redshift-space galaxy $C_\ell^{(p,q)}$ using the CLASS code (Blas et al., 2011), taking into account the specific radial selection, and a linear bias evolution that fits that of the data (see §4.3), normalised to the corresponding σ_8 in this cosmology.

For consistency, since we do not know a priori the true cosmology of the Universe, we use this covariance matrix for the data analysis and all the tests performed on our mock catalogues, irrespective of their true fiducial cosmology. For illustration, figure 4.3 shows a comparison of some sections of the covariance-matrix model (dashed and solid lines) against one estimated from the mocks (symbols). The upper panel shows the square root of the diagonal of two sub-matrices corresponding to one auto-correlation and one cross-correlation function measurement (see key), and the bottom panel shows the square root of vertical cuts of the same sub-matrices at a fixed θ_j bin.

4.2.4 Redshift binning optimisation

The binning scheme in redshift shells is a significant variable to consider for our analysis. As we already mention in the previous chapter, thinner shells result in a sharper BAO feature, at the expense of increasing the statistical uncertainties (due to the smaller number of objects) and increasing the correlation between different shells. Thicker shells on the other hand, improve the statistical errors, while lowering the BAO signal because it is projected over an increasingly wide range of angular scales.

To maximise the constraining power of our analysis, we optimise the number and the width of the redshift shells we use. Our optimisation is based on the binning strategy in Di Dio et al. (2014), which defines the width Δz of each shell in such a way that all of them have the same number of galaxies. This results in a constant shot-noise in all our measurements, which is the main contributor to the covariance matrix in a sample with the number density of BOSS. In this procedure we use a smoothed version of the radial number
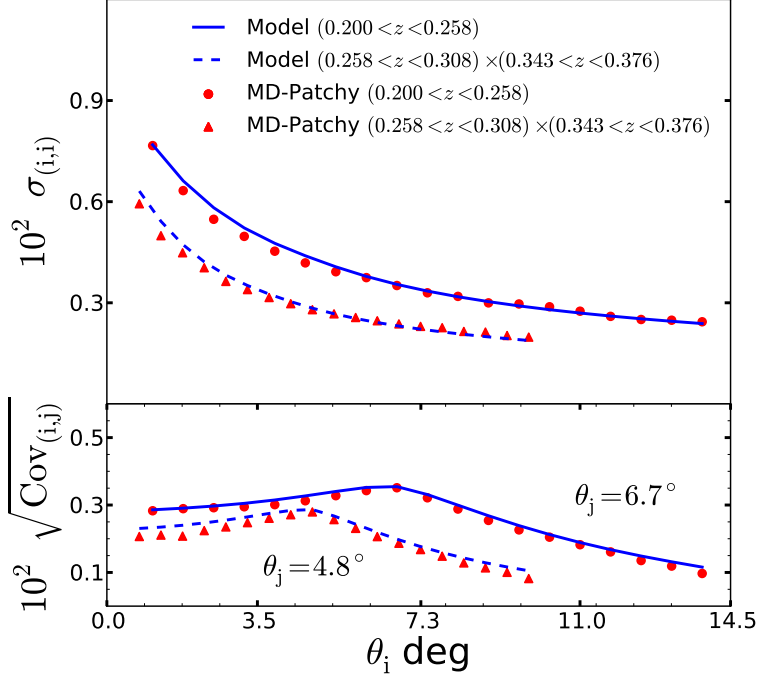
Figure 4.3: Comparison between sections of the model (dashed and solid lines) and the estimate from the mock catalogues (symbols). The upper panel shows the square root of the diagonal of two sub-matrices corresponding to one auto-correlation and one cross-correlation function measurement (see key). The bottom panel shows the square root of vertical cuts of the same sub-matrices at a fixed θ_j bin.

counts, $N(z)$, in order to avoid our binning to be affected by the clustering itself.

    The criteria to define the optimal binning scheme is to maximise the Figure-of-Merit (FoM) in the $\Omega_\mathrm{m} - w_\mathrm{DE}$ plane, defined as

$$\mathrm{FoM}_{w_\mathrm{DE}, \Omega_\mathrm{m}} = \frac{1}{\sqrt{\det[\mathrm{Cov}(w_\mathrm{DE}, \Omega_\mathrm{m})]}}, \qquad (4.12)$$

where $\det[\mathrm{Cov}(w_\mathrm{DE}, \Omega_\mathrm{m})]$ is the determinant of the covariance matrix between the two parameters being constrained. We only use the cosmological information encoded in the full shape of $\omega(\theta)$ for this purpose.

    First, we test our optimisation procedure using only auto-correlations, exploring two different methods to compute the FoM for a given configuration:
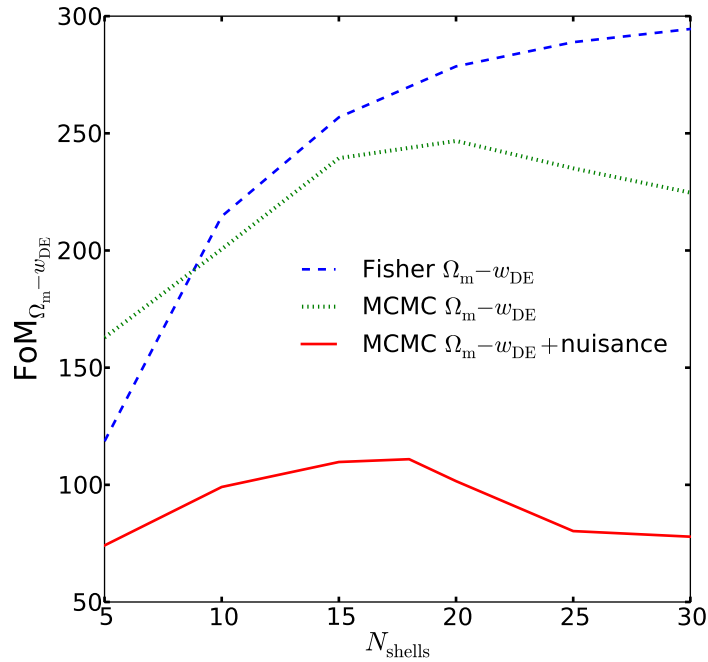
Figure 4.4: Figure-of-Merit constraining $\Omega_m - w_{DE}$ as a function of the number of shells for the combined BOSS sample. The blue dashed line shows the prediction using the Fisher matrix-information technique, the green dashed line shows the prediction from the MCMC analysis when only the cosmological parameters are allowed to vary, and the red solid line shows that of the case where we also include the model nuisance-parameters in the MCMC analysis.

(i) a Fisher information-matrix analysis,

(ii) a Markov chain Monte Carlo (MCMC) analysis, based on chapter 3, using synthetic data.

Both methods are performed using our model of the full covariance matrix of $\omega(\theta)$, and taking into account the specific characteristics of BOSS (i.e. angular and radial selection function). Thus, the optimal binning scheme found here is specific for BOSS, and does not apply to other galaxy surveys.

We perform two versions of the MCMC analysis: one varying only the cosmological parameters, and another one where we also include the nuisance parameters of our model. Figure 4.4 shows the obtained values of the FoM for these tests, as a function of the number of redshift shells, N_{shells}. The blue dashed line corresponds to the predictions from the Fisher matrix analysis, the green dashed line shows the predictions from the MCMC analysis when only w_{DE} and Ω_m are allowed to vary, and the red solid line shows the results of

the case where we also include the model nuisance-parameters in the MCMC analysis. While the Fisher analysis always predicts a monotonically higher FoM as the number of shells increases, none of the MCMC analyses shows this behaviour, where the value of the FoM has a maximum and then decays. This might be explained by the fact that the Fisher matrix analysis approximates the shape of the posterior distribution by a multivariate Gaussian, which in reality is not correct for this combination of parameters. Thus, as N_{shells} increases, the reduction of the posterior-distribution surface (which is what the FoM is actually estimating) is not equal for both methods. This, in the Fisher analysis case, could compensate the lost of information in the regime where the shot noise dominates (high N_{shells}).

Regarding the two different MCMC analysis, it is clear that the inclusion of the nuisance parameters also changes the optimal value of N_{shells}. For this reason, in the following we only use the "$w_{\mathrm{DE}} - \Omega_{\mathrm{m}}$+nuisance" method.

Next, we extend the analysis of the optimal binning-scheme by including the cross-correlations between different redshift shells, imposing two conditions:

(i) as before, each redshift shell must contain the same number of galaxies and,

(ii) for each redshift shell, we include as many cross-correlations with subsequent redshift-shells as necessary to reach at least $120\mathrm{Mpc}/h$ (in the BOSS fiducial cosmology), i.e. past the BAO scale in the line-of-sight direction.

In this case we also find that the maximum is consistent with the previous tests, but the value of the FoM increases by a factor ~ 2, with respect to the case where we only use auto-correlations.

As a result, the optimal binning scheme for the combined sample of BOSS is set to 18 redshift-shells, each of them with ~ 70000 objects. The redshift limits of the optimal binning for the combined sample are listed in table B.10. In §4.3 we show that, in order to obtain robust cosmological constraints, we need to exclude the last three redshift shells at $z \gtrsim 0.6$. For this reason, the final configuration consists of 40 measurements in total, 15 auto-correlation functions and 25 cross-correlation functions, as shown in table B.11 in matrix form.

4.2.5   Model performance on mock catalogues

We test our model for $\omega(\theta)$ and its full covariance matrix against the combined sample MD-PATCHY mock catalogues. We measure the angular clustering us-
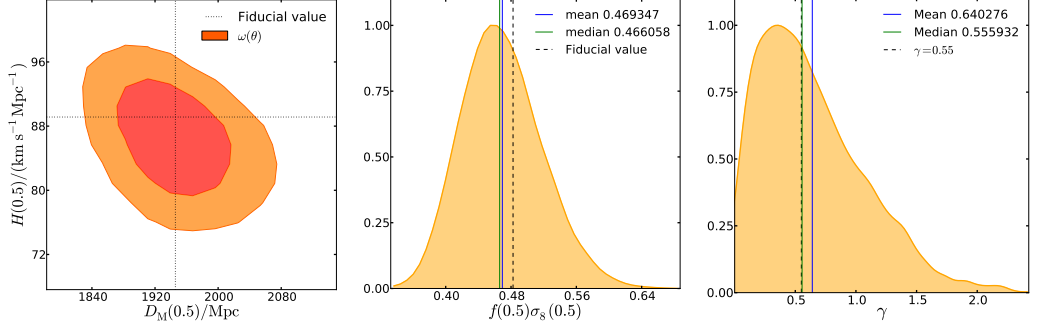
Figure 4.5: Results from the tests, described in §4.2.5, of our tomographic technique applied to the mean of 1000 MD-PATCHY mock catalogs. The left panel shows derived constraints on $D_{\mathrm{M}}(z = 0.5)$ and $H(z = 0.5)$. The central panel shows derived constrains on $f\sigma_8$ at $z = 0.5$. The right panel shows constraints on the growth index γ.

ing the binning scheme described in §4.2.4, and perform fits to the mean of 1000 realisations and to a subsample of 100 realisations individually. Through MCMC analyses, we explore four parameter spaces that are extensions of the standard ΛCDM model, allowing for curvature and a free dark energy equation of state parameter, w_{DE}, constant in time; keeping the spectral index n_{s} and the baryon fraction f_{b} fixed to their fiducial value.

The first parameter space consists of

$$\mathbb{P}_1 = \{\Omega_{\mathrm{K}}, \Omega_\Lambda h^2, w_{\mathrm{DE}}, \ln(10^{10} A_{\mathrm{s}}), b_1, b_2, \gamma_3^-, a_{\mathrm{vir}}\}, \qquad (4.13)$$

using the F96 bias-model in equation (4.4), and the CGC bias-model in equation (4.5). The second parameter space is given by

$$\mathbb{P}_2 = \mathbb{P}_1 \cup \{b'\}, \qquad (4.14)$$

using the redshift evolution of the linear galaxy bias as in equation (4.6). The other two parameter spaces are defined as

$$\mathbb{P}_3 = \mathbb{P}_1 \cup \{\gamma\}, \qquad (4.15)$$

$$\mathbb{P}_4 = \mathbb{P}_2 \cup \{\gamma\}, \qquad (4.16)$$

where γ is the growth index, such that the growth rate factor, $f = \frac{\partial \ln D}{\partial \ln a}$, is approximated by (Linder, 2005)

$$f(a) \approx \Omega_{\mathrm{m}}^\gamma(a), \qquad (4.17)$$

and consequently the linear growth factor is

$$\ln D(a) \approx \int_{a_0}^{a} \frac{da}{a} \Omega_{\mathrm{m}}^{\gamma}(a), \tag{4.18}$$

imposing the border condition $\frac{D(a_0)}{a_0} = 1$ at some a_0 in the matter-dominated epoch. The value of $\gamma = 0.55$ recovers the predictions of General Relativity (GR) for $D(a)$ and $f(a)$, and any deviation from it (in the real data) would suggest a that the clustering measurements are in tension with GR. We assume a Gaussian likelihood function of the form $\mathcal{L}(\mathbf{P}) \propto \exp\left(-\chi^2(\mathbf{P})/2\right)$, where

$$\chi^2(\mathbf{P}) = [\mathbf{m}(\mathbf{P}) - \mathbf{d}]^T \, \mathsf{Cov}^{-1} \, [\mathbf{m}(\mathbf{P}) - \mathbf{d}], \tag{4.19}$$

$\mathbf{P}$ is a vector with the parameter values, $\mathbf{d}$ is the full data vector containing all the measurements of $\omega^{(p,q)}(\theta)$, $\mathbf{m}(\mathbf{P})$ is the model vector given $\mathbf{P}$, and Cov is the full covariance matrix described in §4.2.3.

For each test we derive values of $D_{\mathrm{M}}(z_{\mathrm{ref}})$, $H(z_{\mathrm{ref}})$, $f(z_{\mathrm{ref}})$ and $\sigma_8(z_{\mathrm{ref}})$ from the cosmological parameters, at the reference redshift $z_{\mathrm{ref}} = 0.5$. These quantities are more familiar in galaxy clustering analyses, and easier to refer to. We emphasise though, that these are derived quantities, and we are not measuring them at that particular redshift, but rather constraining the cosmological parameters through the full shape of $\omega(\theta)$ and its redshift evolution.

We performed tests constraining $\mathbb{P}_1$ using (4.4) and $\mathbb{P}_2$ for different minimum angular scales, $\theta_{\min}(\bar{z}^{(p,q)})$, using the mean of the mocks. We find that using smaller angular scales than $\theta_{\min}(\bar{z}^{(p,q)}) = 20\mathrm{Mpc}/h$ (in the BOSS fiducial cosmology) results in biased constraints, while larger values only increase the errors without changing the mean. In the rest of this analysis, we use this minimum scale.

The CGC model for the galaxy-bias evolution, given by equation (4.5), does not describe $b(z)$ of the mock catalogs, resulting in biased constraints, of $\gtrsim 1\sigma$, in all the tests.

Figure 4.5 shows the results obtained using the mean of the mocks for different tests. The left panel shows constraints on $D_{\mathrm{M}}(z_{\mathrm{ref}})$ and $H(z_{\mathrm{ref}})$ on $\mathbb{P}_2$, i.e. using the linear bias in equation (4.6). We do not see any significant deviation in this case, finding 0.1σ and 0.3σ for $D_{\mathrm{M}}(z_{\mathrm{ref}})$ and $H(z_{\mathrm{ref}})$ respectively. These deviations are somewhat smaller, and the errors tighter, in the test on $\mathbb{P}_1$ using the F96 bias model in equation (4.4). The middle panel shows constraints on $f(z_{\mathrm{ref}})\sigma_8(z_{\mathrm{ref}})$ on $\mathbb{P}_2$, and the right panel shows the constraints on the growth index γ on $\mathbb{P}_4$. In these two cases, the results on $\mathbb{P}_1$ and $\mathbb{P}_3$, using the F96 model, are also unbiased and the errors smaller. In all three panels, the fiducial values, shown by the dashed lines, are those corresponding to the true cosmology of the MD-PATCHY mock catalogues.
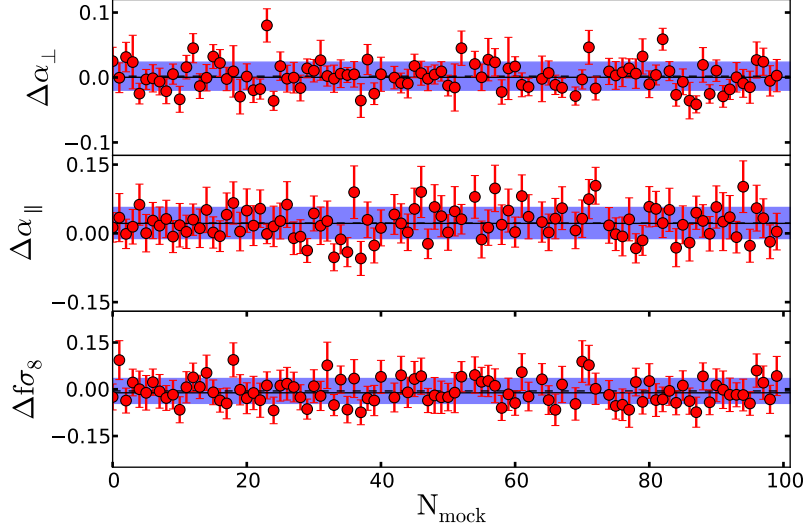
Figure 4.6: Deviations between the true and the obtained values for the derived parameters $\alpha_\perp$, $\alpha_\parallel$ and $f\sigma_8$ at $z = 0.5$, from the individual fits (symbols) on a subset of 100 MD-PATCHY mock catalogues. Error bars correspond to the estimated error on each fit, while the blue bands show the sample standard deviation. The upper panel shows the deviations on $\alpha_\perp$, the middle panel shows the deviations on $\alpha_\parallel$, and the lower panel shows those of $f\sigma_8$.

Figure 4.6 shows the results of the same test, this time fitting the subset of 100 mocks individually, constraining $\mathbb{P}_2$. The upper panel shows the deviations from the true values on

$$\alpha_\perp = \frac{D_\mathrm{M}(z) r_\mathrm{s}^\mathrm{fid}(z_\mathrm{d})}{D_\mathrm{M}^\mathrm{fid}(z) r_\mathrm{s}(z_\mathrm{d})}, \tag{4.20}$$

the middle panel shows those of

$$\alpha_\parallel = \frac{H^\mathrm{fid}(z) r_\mathrm{s}(z_\mathrm{d})}{H(z) r_\mathrm{s}^\mathrm{fid}(z_\mathrm{d})}, \tag{4.21}$$

and the lower panel the deviations on $f\sigma_8$ at z_ref, where $r_\mathrm{s}(z_\mathrm{d})$ is the sound horizon at the drag redshift, and "fid" stands for the fiducial values in the mock's cosmology. The error bars correspond to the error from the individual fits, and the blue band corresponds to the standard deviation of the sample. The solid and dashed lines are the median and the mean of the distribution respectively, which are practically indistinguishable because the individual values are normally distributed.

Overall, these tests show that, through the redshift evolution of the full shape of $\omega(\theta)$, we can recover an expansion history and RSD information that

is in very good agreement with the fiducial cosmology of the mocks, with the 0.3σ deviation in $H(z)$ being the largest one. These tests also confirm the importance of a sensible choice of a model for the galaxy-bias evolution (see e.g. Clerkin et al., 2015), and show that our simple linear model in eq. (4.6) is flexible enough for the description of the redshift evolution of the linear bias of the BOSS galaxy sample.

4.3   The linear bias of the BOSS galaxy sample

Assuming the best-fitting ΛCDM cosmology from Planck, we measure the linear galaxy bias in each redshift shell in two ways. First, we fit all auto correlations independently (shell by shell), fitting b_1 and marginalising over b_2 and σ_8, the amplitude of (linear-theory) density fluctuations in spheres of $R = 8$ Mpc/h, given by

$$\sigma^2(R) = \int_0^\infty \frac{dk}{k} \frac{k^3}{2\pi^2} P_L(k) W^2(kR), \qquad (4.22)$$

where

$$W(x) = 3\left(\frac{\sin(x) - x\cos(x)}{x^3}\right) \qquad (4.23)$$

is the Fourier transform of a spherical top-hat window function of radius R. We impose a prior on σ_8 from Planck. Secondly, we fit all redshift shells simultaneously, using each of our three models for $b(z)$ (Linear, F96 and CGC), and marginalising over the other three nuisance parameters of our model for $\omega(\theta)$. For comparison, we repeated the first test on the mean of the MD-PATCHY mocks, using the correct $P_L(k)$ and σ_8 for the mocks cosmology.

4.3.1   The redshift evolution of the linear bias of BOSS galaxies

None of the models for the redshift evolution of the linear galaxy-bias used in this analysis is able to simultaneously fit, within the errors, the first 16 measurements and the two high-redshift ones. A possible explanation for this is that, above $z \gtrsim 0.6$, the BOSS galaxy sample behaves as a flux-limited one (see e.g. Saito et al., 2015), i.e. only intrinsically bright galaxies can be observed at those distances, while intrinsically fainter ones are not in the sample. On the other hand, at $z \lesssim 0.6$, this galaxy sample is much closer to a volume-limited sample, thus practically all galaxies brighter than a certain absolute magnitude M_{lim} have been observed. In practice, this means that
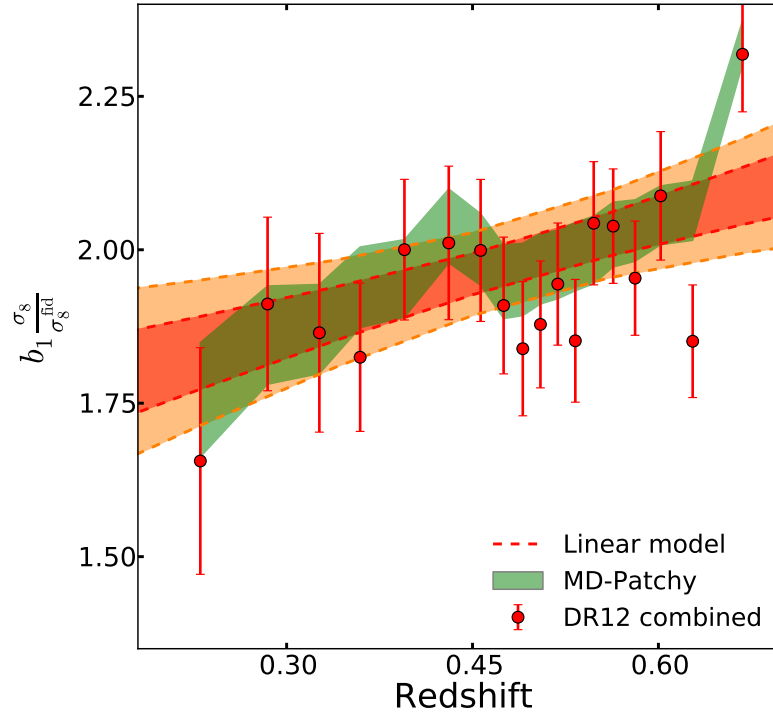
Figure 4.7: Redshift evolution of the linear galaxy bias. Red symbols show individual fits to 18 $\omega(\theta)$ measurements on BOSS. The green band shows the result of performing the same exercise on the mean of the MD-PATCHY mock catalogues. The dashed lines show the 68% and 95% confidence intervals obtained by fitting all clustering measurements simultaneously (excluding the three highest-redshift ones) with the bias model given in equation (4.6).

above $z \gtrsim 0.6$, the effective clustering amplitude is not representative of a given galaxy population, but rather dominated by observational systematics. This is the reason why in chapter 3 we restricted the analysis to the redshift range $0.2 \leq z \leq 0.6$, in order to justify the assumption of a constant number density. This effect has not been observed before in other clustering analyses of BOSS galaxies in redshift bins (Reid et al., 2014; Saito et al., 2015), because the binning in those analyses consisted in much wider redshift-bins, hindering this variation in the amplitude of the clustering signal.

Not being able to reproduce the linear bias, hence the clustering amplitude of these high-redshift measurements, has two important consequences. An incorrect estimation of the linear galaxy bias, for a given redshift shell, implies that all estimates of the covariance in equation (4.9) including this redshift shell will be incorrect. Secondly, the F96 and CGC models depend on the growth factor $D(z)$, which encodes cosmological information. Then,

non-cosmological variations in the linear galaxy-bias could result in biased cosmological constraints. For this reason, and in order to be conservative, we exclude the galaxies above redshift $z = 0.6$ from the rest of the analysis. This means that we do not use the last three high-redshift bins, even though the 16th shell at $z \sim 0.6$ seems to be within the errors.

Figure 4.7 shows the measured linear galaxy bias normalised by the ratio of the corresponding σ_8 of each cosmology and the fiducial one coming from the Planck prior. The individual measurements are shown by the red circles, where error bars correspond to the 1σ marginalised error. The joint fit assuming the linear galaxy-bias evolution of equation (4.6) is shown by the dashed lines, where the different levels correspond to one and two σ confidence levels. We have excluded the last three high-redshift measurements from this fit. The green band shows the 1σ region of the individual fits on the mean of the mock catalogues.

4.3.2   The impact of the bias redshift evolution of BOSS galaxies on cosmological constraints

We test the impact that assuming any of the three models for the redshift evolution of the linear galaxy bias has on the obtained cosmological constraints. For this we combine our measurements of the full shape of $\omega(\theta)$ with Planck, and perform an MCMC analysis. Using each of the three models, we explore an extension of the standard ΛCDM model, allowing for the dark energy equation-of-state parameter, w, assumed to be constant in time, to deviate from the canonical value of -1. The basic cosmological parameters explored are listed in the first block of table 4.2.

Figure 4.8 shows the constraints on the total mass density parameter, Ω_{m}, and w, obtained from the "Planck $+ \omega(\theta)$" combination. The blue dashed line corresponds to the use of the linear model for $b_1(z)$, the red solid line to CGC, and the green dash-dotted line corresponds to the F96 bias model. Unlike what we find in the tests on the mock catalogues in §4.2.5, where different assumptions for the evolution of the linear galaxy-bias result in differences in the final cosmological constraints, the "Planck $+ \omega(\theta)$" combination seems to be robust against the different assumptions within the errors. The three mean values recovered in each case are within $0.16\sigma_{\mathrm{Linear}}$ from the linear bias case and, in both the CGC and the F96 cases, the errors are only about 4% tighter compared to the linear case. Mean values and confidence intervals for the linear case are shown in §4.4.2. Our interpretation is that, firstly, the inclusion of CMB data breaks degeneracies within parameters that are present in the $\omega(\theta)$-only likelihood function, which could solve the 1σ deviation from
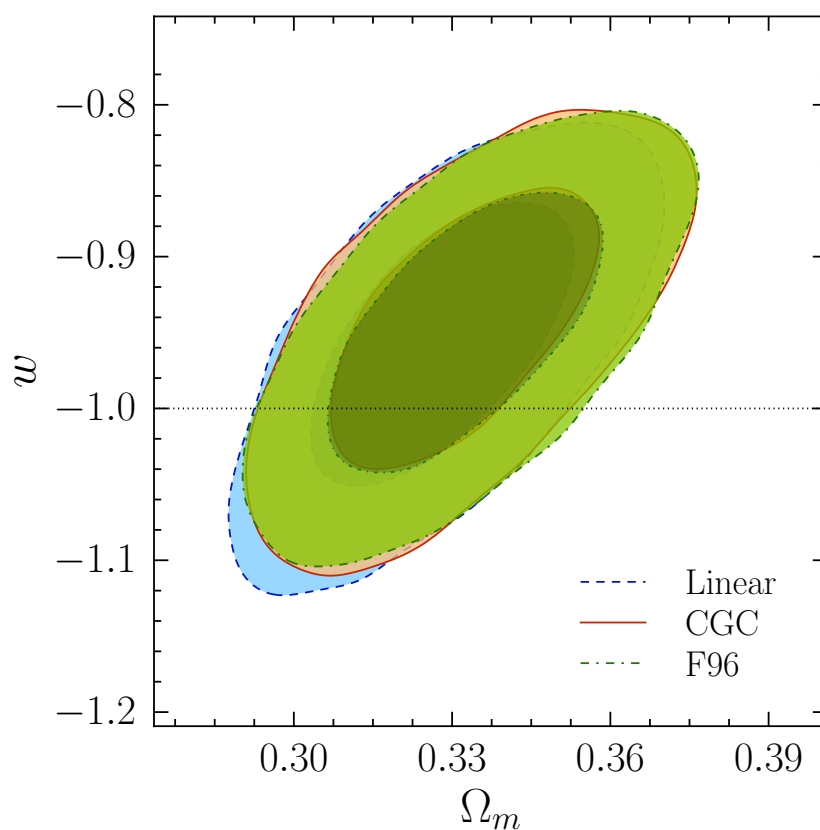
Figure 4.8: Cosmological constraints obtained from the "Planck + $\omega(\theta)$" combination using each of our three models for the redshift-evolution of the linear galaxy-bias. Contours show the 68% and 95% confidence intervals on the $\Omega_{\mathrm{m}} - w$ plane.

the CGC model (assuming that the bias evolution of the mocks represents well that of the data). Secondly, the assumed models for the redshift evolution of the linear galaxy bias are well motivated on the characteristics of BOSS galaxies (see §4.2.2), thus large deviations are not expected.

4.4   Cosmological constraints

In this section we present constraints on cosmological parameters for the standard ΛCDM model, as well as for eight different extensions described in the following subsections. For this purpose we use the July 2015 version of the publicly-available MCMC-code COSMOMC (Lewis and Bridle, 2002), modified to compute the model for $\omega(\theta)$, including non-linearities, bias and redshift-space distortions, described in §4.2.1 and §4.2.2. Although we found in the previous section that, after combining our angular clustering measurements with Planck, the different assumptions for the redshift evolution of the linear galaxy-bias do not have a significant impact on the cosmological constraints, here we take a conservative approach and only use the linear model in equation (4.6).

Table 4.2 displays the cosmological parameters explored in these analyses, the ranges in which they are allowed to vary, and fiducial values in the case that a given parameter is fixed. The first block lists the basic parameters varied in all cases, corresponding to those that characterise the standard ΛCDM cosmological model. The second block in the table lists those parameters that represent extensions of the standard cosmological model explored in this analysis. The last block in table 4.2 displays derived parameters quoted in each case.

As we do in §3.2.4, we assume Gaussian likelihood function of the form $\mathcal{L}(\mathbf{P}) \propto \exp\left(-\chi^2(\mathbf{P})/2\right)$ for our clustering measurements, where χ^2 is computed as in equation (4.19).

Planck CMB constraints are only shown in figures for comparison, and we quote results for the "Planck $+ \omega(\theta)$" and "Planck $+ \omega(\theta) +$ SNIa" cases only. Summary tables are given in appendix B for readability, and in the text we only quote values of the most relevant parameters for each cosmological model. In every case, the values and confidence intervals correspond to those obtained after marginalising over all other parameters.

4.4.1   The standard ΛCDM model

We start out with the basic case: the ΛCDM model. This model has become the standard cosmological model due to its astonishing description and

Parameter	Range	Fiducial value	Description
$\Omega_b h^2$	$[0.005, 0.1]$	-	Physical baryon density
$\Omega_c h^2$	$[0.001, 0.99]$	-	Physical CDM density
$100\theta_{\mathrm{MC}}$	$[0.5, 10]$	-	Approximate angular size of r_{s} at recombination[a]
τ	$[0.01, 0.8]$	-	Optical depth to the reionisation epoch
$\ln(10^{10} A_s)$	$[2, 4]$	-	Scalar spectral amplitude[b]
n_s	$[0.8, 1.2]$	-	Scalar spectral index[b]
w_0	$[-0.3, -3]$	-1	Present-day w_{DE}
w_a	$[-2, 2]$	0	Time dependence of w_{DE}
Ω_{K}	$[-0.3, 0.3]$	0	Curvature contribution to the energy density
Σm_ν	$[0, 2]\mathrm{eV}$	$0.06\mathrm{eV}$	Total sum of neutrino masses
γ	$[0, 2]$	-	Growth index
H_0	$[20, 100]$	-	Hubble constant
Ω_{m}	-	-	Present-day total matter density
Ω_Λ	-	-	Dark energy density
σ_8	-	-	Amplitude of linear-theory density fluctuations in spheres of R = 8Mpc/h
Age/Gyr	-	-	Age of the Universe

Table 4.2: Summary of the cosmological parameters explored in this analysis. Basic ΛCDM parameters are in the first block, while those of extended cosmological models are listed in the second block. The last block shows derived parameters quoted in avery case.
[a] *As defined in the July 2015 version of* COSMOMC.
[b] *Quoted at the pivot $k_0 = 0.05$ (Mpc)$^{-1}$.*
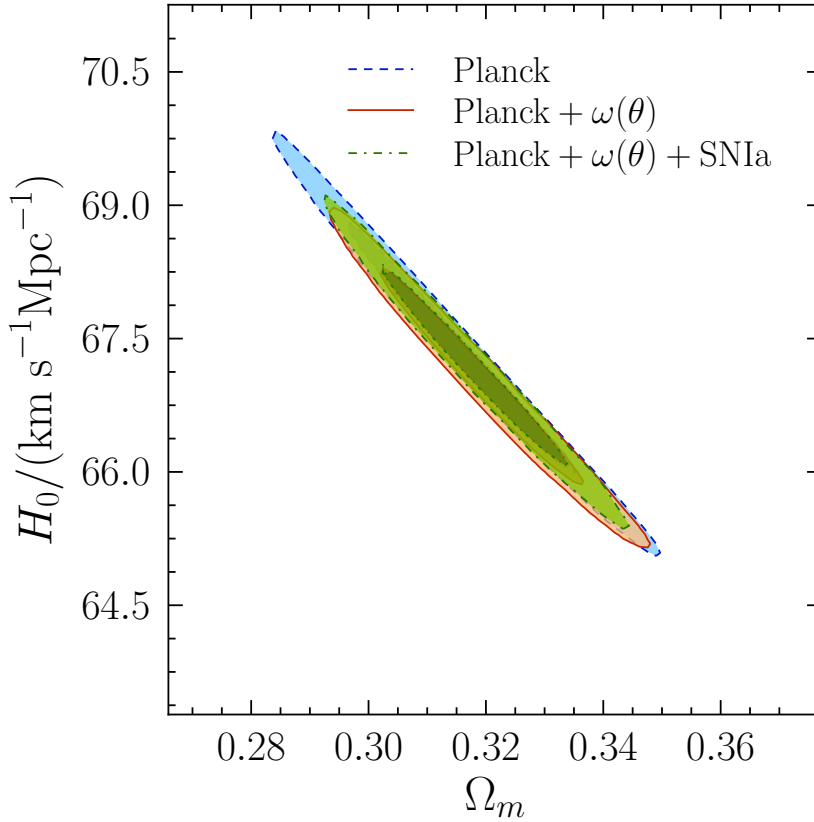
Figure 4.9: Marginalised 68% and 95% confidence interval constraints in the $\Omega_m - H0$ plane. The blue dashed line corresponds to Planck-only constraints, the solid orange line corresponds to the constraints obtained from the Planck$+$ $\omega(\theta)$ combination, and the green dash-dotted line to those obtained combining Planck $+ \omega(\theta) +$ SNIa.

prediction capabilities, regarding a large list of observables.

Figure 4.9 shows the marginalised 68 and 95 per cent confidence interval in the $\Omega_m - H_0$ plane. The blue dashed line corresponds to Planck-only constraints, the solid orange line shows the constraints obtained from the Planck $+ \omega(\theta)$ combination, and the green dash-dotted line those obtained combining Planck $+ \omega(\theta) +$ SNIa. We find that including our angular clustering measurements improves the constraints, and the subsequent addition of SNIa slightly shifts the allowed region toward higher values of H_0 and does not represent a significant improvement. We also find that the Planck $+ \omega(\theta)$ combination selects the highest values of Ω_m allowed by Planck, as opposed to previous 3D clustering analyses on BOSS (see e.g. Sánchez et al., 2013; Anderson et al., 2014b). Nevertheless, our results and those mentioned are consistent

within 1σ. We found $\Omega_{\mathrm{m}} = 0.319 \pm 0.011$ for the Planck$+\omega(\theta)$ combination, and $\Omega_{\mathrm{m}} = 0.317 \pm 0.011$ including SNIa. Table B.1 shows marginalised constraints for all the parameters varied in this case, as well as the derived parameters.

4.4.2   The dark energy equation-of-state w_{DE}
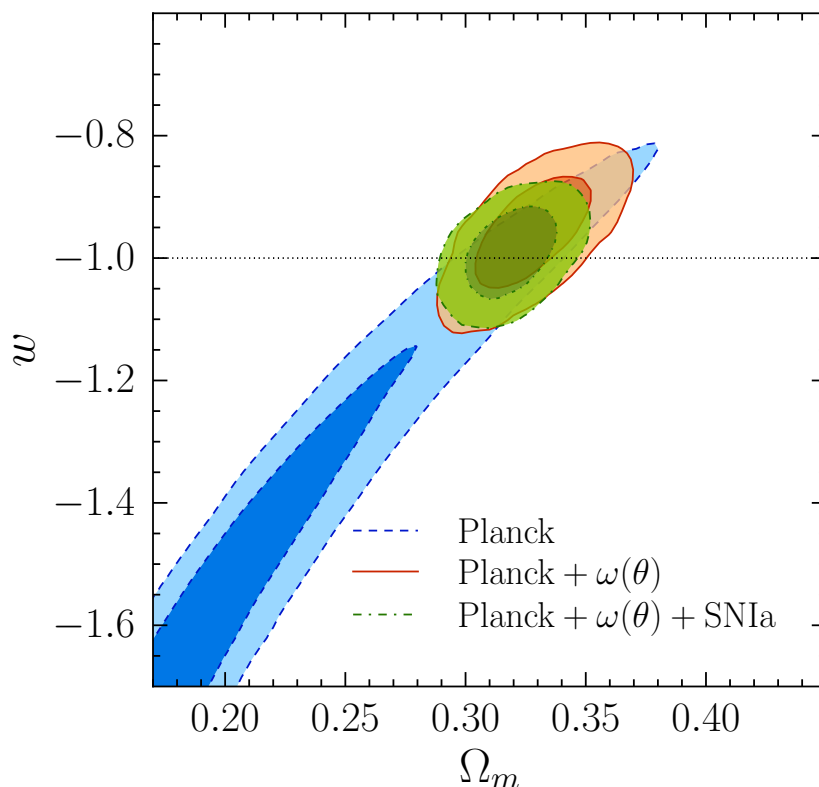
Figure 4.10: Marginalised 68% and 95% confidence interval constraints in the $\Omega_{\mathrm{m}} - w$ plane. The blue dashed line corresponds to Planck-only constraints, the solid orange line corresponds to the constraints obtained from the Planck$+$ $\omega(\theta)$ combination, and the green dash-dotted line to those obtained combining Planck $+ \omega(\theta) +$ SNIa.

Although the standard ΛCDM model is sufficient to describe the expansion history of the Universe, as probed by the CMB power spectrum, galaxy clustering measurements and SNIa, the combination of all these observables allows us to test assumptions and generalisations of it. One of such assumptions is that the dark-energy component of the Universe is characterised by an equation of state $P_{\mathrm{DE}}/\rho_{\mathrm{DE}} \equiv w_{\mathrm{DE}} = -1$ constant in time. Thus the first

tested extension of the standard cosmological model is to treat w_{DE} as a free parameter (wCDM model), assuming it is constant in time.
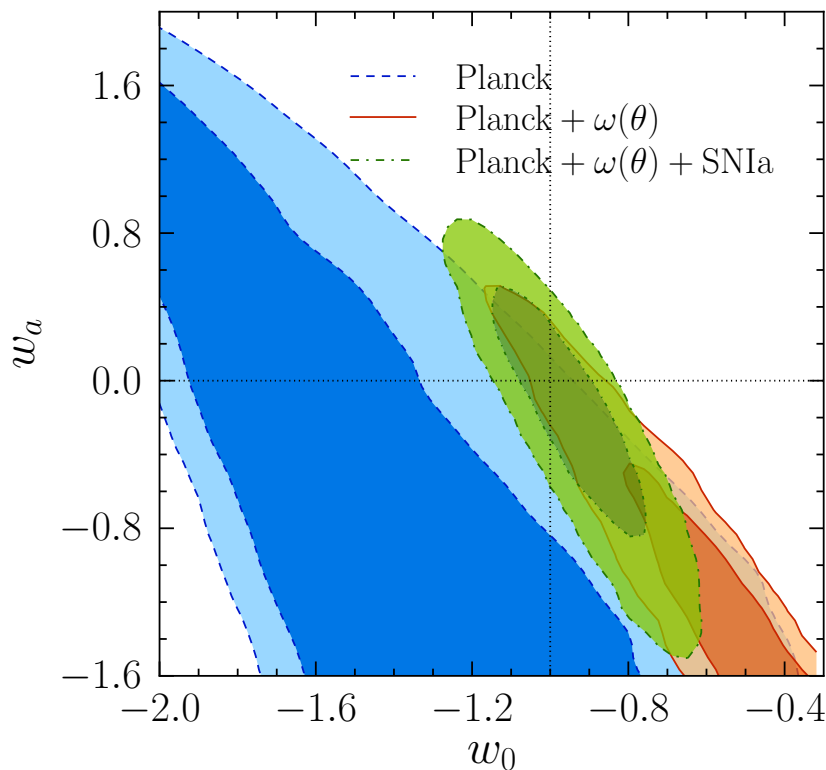
Figure 4.11: Marginalised 68% and 95% confidence interval constraints in the $w_0 - w_a$ plane. The blue dashed line corresponds to Planck-only constraints, the solid orange line corresponds to the constraints obtained from the Planck$+$ $\omega(\theta)$ combination, and the green dash-dotted line to those obtained combining Planck $+ \omega(\theta) +$ SNIa.

Figure 4.10 shows the marginalised 68 and 95 per cent confidence interval constraints in the $\Omega_{\mathrm{m}} - w$ plane. As before, the blue dashed line corresponds to Planck-only constraints, the solid orange line to the results obtained from the Planck $+ \omega(\theta)$ combination, and the green dash-dotted line to those obtained combining Planck$+\omega(\theta)+$SNIa. We find that including our angular clustering measurements significantly improves the constraints obtained by Planck, where we found a value of $\Omega_{\mathrm{m}} = 0.328 \pm 0.016$ and $w = -0.958^{+0.063}_{-0.055}$, in very good agreement with the ΛCDM results. In this case, the Planck $+ \omega(\theta) +$ SNIa combination improves the constraints even more, resulting in $\Omega_{\mathrm{m}} = 0.319 \pm 0.012$ and $w = -0.991 \pm 0.046$, again in very good agreement with the ΛCDM case. A summary of the constraints obtained in this case can be found in table

B.2.
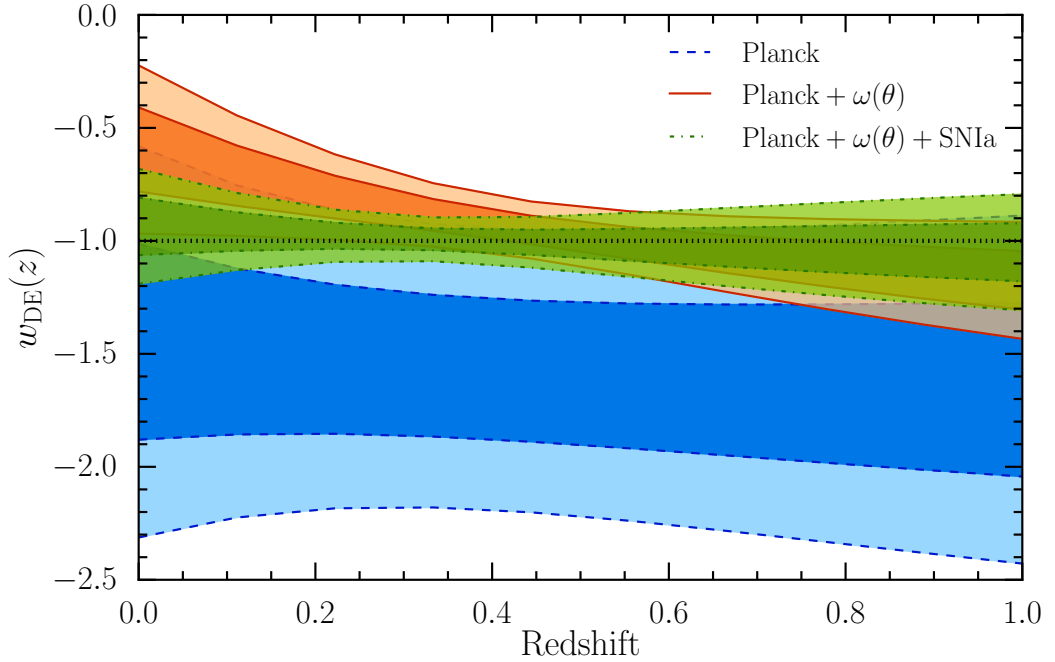
Figure 4.12: Marginalised 68% and 95% confidence interval constraints on the redshift evolution of $w_{DE}(z)$ using the CPL parametisation. The blue dashed line corresponds to Planck-only constraints, the solid orange line corresponds to the constraints obtained from the Planck+$\omega(\theta)$ combination, and the green dash-dotted line to those obtained combining Planck + $\omega(\theta)$ + SNIa.

Next, we allow w_{DE} to vary over time as we did in §3.3 ($w_0 w_a$CDM model), following the standard linear parametrisation of Chevallier and Polarski (2001) and Linder (2003) (CPL), given in equation (3.42). The marginalised 68 and 95 per cent confidence interval constraints, in the $w_0 - w_a$ plane, are shown in figure 4.11. In this case, we see a strong degeneracy between these two parameters for the Planck only and the Planck+$\omega(\theta)$ combinations, where the fiducial ΛCDM values for these parameters, shown by the dotted lines, are only within the 95% confidence interval, suggesting a mild tension with the standard cosmological model. Nevertheless, adding SNIa breaks this degeneracy and eliminates this tension. In this, case we find $w_0 - 0.94 \pm 0.13$ and $w_a = -0.23^{+0.51}_{-0.42}$. Table B.3 summarises the cosmological constraints for this case.
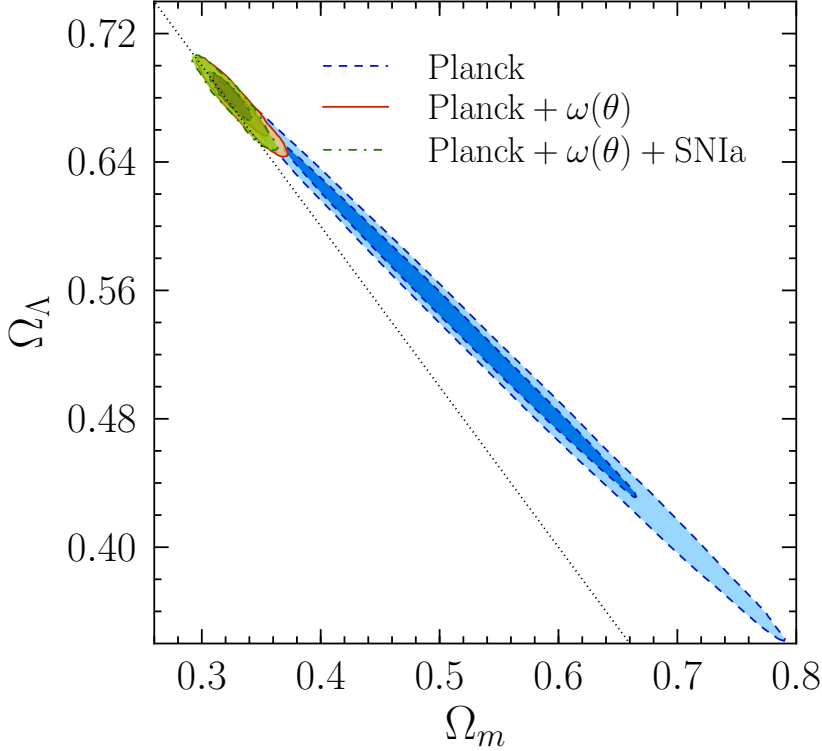
Figure 4.13: Marginalised 68% and 95% confidence interval constraints in the $\Omega_m - \Omega_\Lambda$ plane, relaxing the flat-space condition. The blue dashed line corresponds to Planck-only constraints, the solid orange line corresponds to the constraints obtained from the Planck $+ \omega(\theta)$ combination, and the green dash-dotted line to those obtained combining Planck $+ \omega(\theta) +$ SNIa.

4.4.3   Non spatially-flat Universes

Another assumption of the standard ΛCDM model is that the Universe is spatially flat, which implies that its total energy density is equal to the critical one. In other words, the sum $(\Omega_\Lambda + \Omega_m + \Omega_\gamma) = 1$. We test this assumption of flatness by including the Ω_K parameter, yielding $(\Omega_\Lambda + \Omega_m + \Omega_\gamma) = (1 - \Omega_K)$.

The first case we analyse assumes $w_{DE} \equiv -1$ (oCDM model). Figure 4.13 shows the marginalised 68 and 95 per cent confidence interval constraints in the $\Omega_K - \Omega_\Lambda$ plane, where the dotted diagonal line corresponds to spatially-flat Universes. It can be seen that relaxing the flat-space condition opens a large degeneracy in the CMB-only constraints, and that this degeneracy is broken adding low-redshift measurements of the expansion history of the Universe, greatly improving the constraints. For the Planck $+ \omega(\theta)$ combination we find $\Omega_m = 0.329^{+0.014}_{-0.016}$, $\Omega_\Lambda = 0.676 \pm 0.013$ and $\Omega_K = -0.0043^{+0.0042}_{-0.0035}$, while

for the full Planck + $\omega(\theta)$ + SNIa combination, we find $\Omega_m = 0.324^{+0.011}_{-0.014}$, $\Omega_\Lambda = 0.679^{+0.013}_{-0.009}$ and $\Omega_K = -0.0028 \pm 0.0038$, in excellent agreement with a spatially-flat Universe, as well as with the results for the ΛCDM case. A summary of the constraints obtained in this case can be found in table B.4.
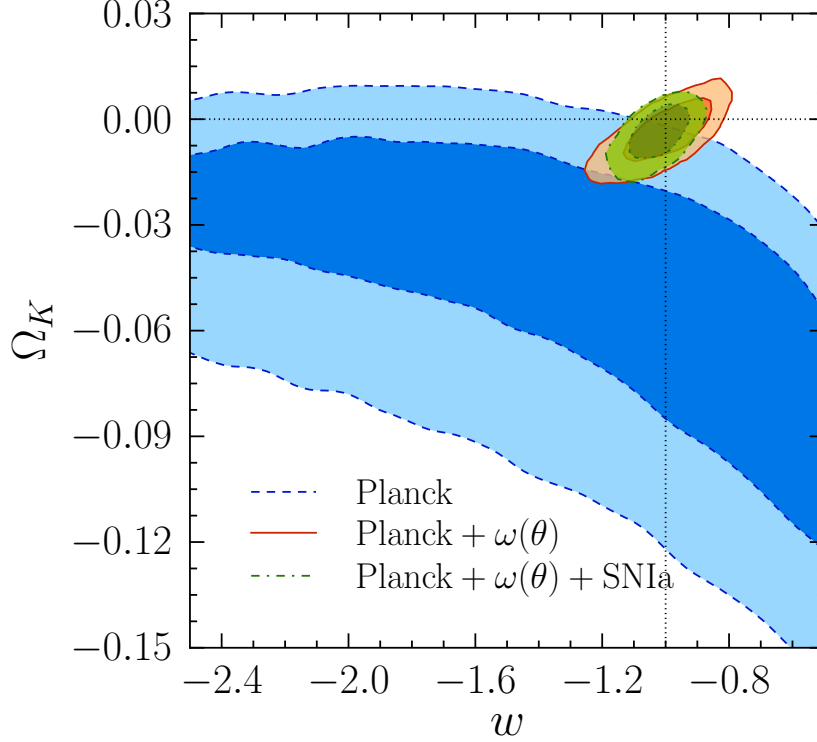
Figure 4.14: Marginalised 68% and 95% confidence interval constraints in the $w - \Omega_K$ plane. The blue dashed line corresponds to Planck-only constraints, the solid orange line corresponds to the constraints obtained from the Planck+ $\omega(\theta)$ combination, and the green dash-dotted line to those obtained combining Planck + $\omega(\theta)$ + SNIa.

We also include w_{DE} as a free parameter in this case, assuming that its value is constant in time (owCDM model). A summary of the constraints for this case can be found in table B.5. Figure 4.14 shows the marginalised 68 and 95 per cent confidence interval constraints in the $w - \Omega_K$ plane. As always, the blue dashed line corresponds to Planck-only constraints, the solid orange line corresponds to the constraints obtained from the Planck + $\omega(\theta)$ combination, and the green dash-dotted line to those obtained combining Planck + $\omega(\theta)$ + SNIa. Again this time, it can be seen that the inclusion of our $\omega(\theta)$ measurements on BOSS, to the CMB-only ones, significantly improves the cosmological constraints, where we find a value of $w = -1.00^{+0.10}_{-0.075}$ and

$\Omega_K = -0.0037^{+0.0057}_{-0.0051}$. Also, including SNIa further tightens the constraints, resulting in $w = -1.025^{+0.064}_{-0.055}$ and $\Omega_K = -0.0040^{+0.0054}_{-0.0041}$, once again, in perfect agreement with the standard cosmological model.

4.4.4   Massive neutrinos

Observations of neutrino oscillations (i.e., a change in neutrino flavour) imply that at least two neutrino species have non-zero mass. This is one of the most significant discoveries in the last decades, providing decisive evidence that the Standard Model (of particle physics) needs to be extended. Actually, it was for this very important discovery (Fukuda et al., 1998; Ahmad et al., 2001, 2002) that Takaaki Kajita and Arthur B. McDonald were awarded the Nobel Prize in Physics last year[1].

Although the fact that neutrinos have mass is well stablished, precise measurements of their mass is a very difficult task. The best upper limits from laboratory experiments, through tritium decay, are $m_{\nu_e} < 2\mathrm{eV}$ for electron neutrinos. Nevertheless, the best constraints in their total-mass sum, including all species, comes from cosmological observations. Relic neutrinos generated in very early Universe are almost as abundant as photons, and they form what is knowns as the cosmic neutrino background ($C\nu B$). At the present, it is not possible to observe the $C\nu B$, but these primordial neutrinos have two important consequences for cosmology. First, they decouple from the other components before photons, free-streaming through the baryon-photon plasma and washing out small-scale anisotropies. Secondly, as we mentioned in §3.3, the effect of massive neutrinos on the expansion rate H is not negligible (see equation (3.37)).

The scales in clustering measurements affected by neutrinos are beyond what we are able to currently model, but we certainly can constrain the effect of neutrinos on the expansion rate. For this, in this section we treat the total sum of neutrino masses, $\sum m_\nu$, as a free parameter, assuming three species of equal mass. We obtain constraints within the ΛCDM and wCDM framework.

Figure 4.15 shows the marginalised 68 and 95 per cent confidence interval constraints in the $\sum m_\nu/\mathrm{eV} - \mathrm{H}_0$ plane, fixing $w_{\mathrm{DE}} \equiv -1$. For the Planck $+ \omega(\theta)$ combination we find $\sum m_\nu/\mathrm{eV} < 0.207(0.400)$ 68%(95%) C.I. upper limits, while for the full Planck $+ \omega(\theta) + $ SNIa combination, we find $\sum m_\nu/\mathrm{eV} < 0.169(0.330)$ 68%(95%) C.I. upper limits, representing one of the tightest constraints at the present. A summary of the constraints obtained in this case can be found in table B.6.

---

[1] "The 2015 Nobel Prize in Physics - Press Release". Nobelprize.org. Nobel Media AB 2014. http://www.nobelprize.org/nobel_prizes/physics/laureates/2015/press.html
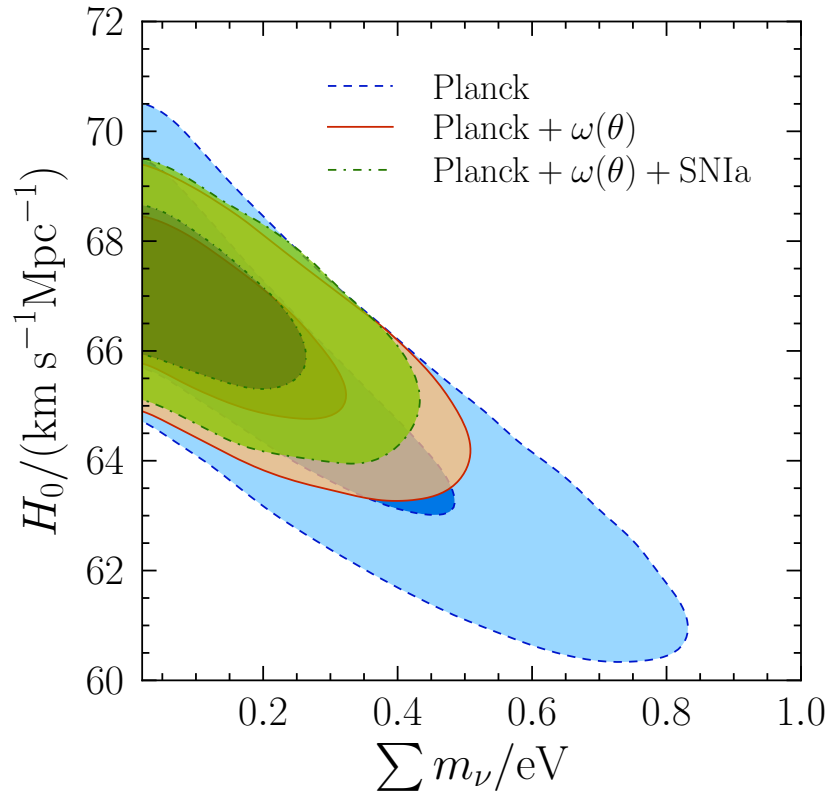
Figure 4.15: Marginalised 68% and 95% confidence interval constraints in the $\sum m_\nu/\text{eV} - \text{H}_0$ plane. The blue dashed line corresponds to Planck-only constraints, the solid orange line corresponds to the constraints obtained from the Planck $+ \omega(\theta)$ combination, and the green dash-dotted line to those obtained combining Planck $+ \omega(\theta) + \text{SNIa}$.
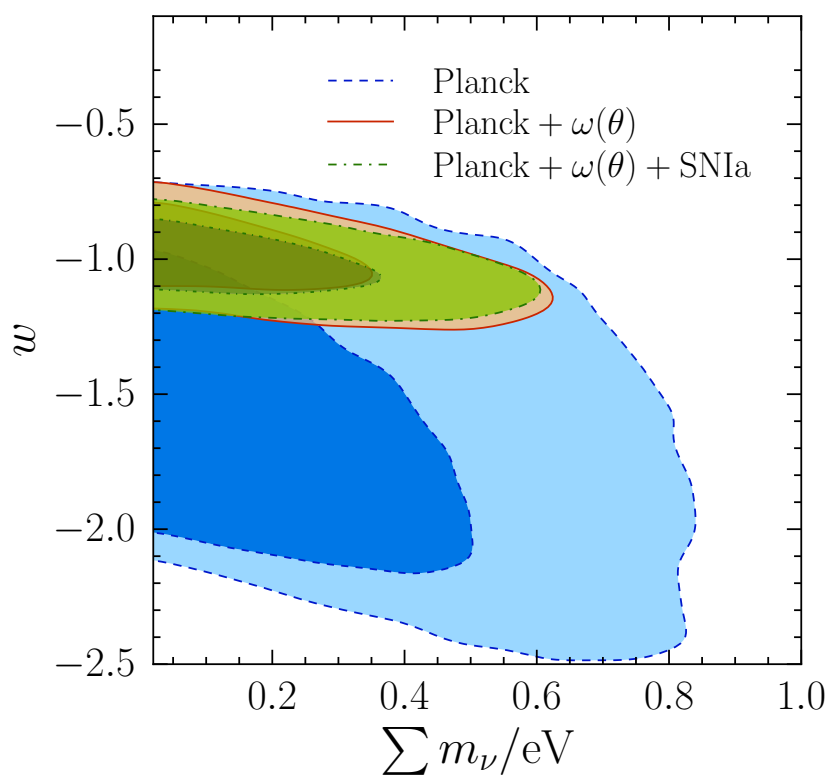
Figure 4.16: Marginalised 68% and 95% confidence interval constraints in the $\sum m_\nu/\text{eV} - w$ plane. The blue dashed line corresponds to Planck-only constraints, the solid orange line corresponds to the constraints obtained from the Planck $+ \omega(\theta)$ combination, and the green dash-dotted line to those obtained combining Planck $+ \omega(\theta) +$ SNIa.

The results of also treating $w_{\rm DE}$ as a free parameter are shown in table B.7. Figure 4.16 shows the marginalised 68 and 95 per cent confidence interval constraints in the $\sum m_\nu/{\rm eV} - w$ plane. In this case, for the Planck $+ \omega(\theta)$ combination we find $\sum m_\nu/{\rm eV} < 0.221(0.486)$ 68%(95%) C.I. upper limits, while for the full Planck $+ \omega(\theta) + $ SNIa combination, we find $\sum m_\nu/{\rm eV} < 0.229(0.474)$ 68%(95%) C.I. upper limits. Note that the inclusion of SNIa increases the 68% C.I. upper limit, decreasing the 95% C.I. one, marginally suggesting non-zero masses, although we cannot claim a detection. Also, including $\sum m_\nu$ as a free parameter does not significantly degrade our constraints in w, resulting in $w = -1.023^{+0.063}_{-0.053}$ for the full Planck $+ \omega(\theta) + $ SNIa combination.

4.4.5 Deviations from General Relativity

The last assumption of the ΛCDM model that we test in this analysis is that of space-time being described by the theory of General Relativity. A thorough analysis of different theories beyond GR requires modifications to our methodology, such as the way the expansion history of the Universe is parametrised, which is out of the scope of this work. However, we perform a simple *null test*, following the parametrisation for linear perturbation growth of Linder (2005), which is decoupled from the expansion history. To a sub per-cent accuracy, the growth rate $f \equiv \frac{\partial \ln D}{\partial \ln a}$ can be approximated as in equation (4.17), where a value of

$$\gamma = 0.55 + 0.05(1 + w_{\rm DE}(z = 1)), \qquad (4.24)$$

for the growth index parameter recovers the prediction of GR. Thus, any deviation from this value, treating γ as a free parameter, would suggest that general relativity should be revised.

First, we assume the standard ΛCDM as the background cosmological model. A summary of the obtained constraints can be found in table B.8. Figure 4.17 shows the marginalised 68 and 95 per cent confidence interval constraints in the $\Omega_{\rm m} - \gamma$ plane. Since CMB cannot be used to measure $f(z)$ and thus constrain γ, Planck-only contours are not shown, and the blue dashed line corresponds to the constraints obtained by the Planck $+ \omega(\theta)$ combination, while the solid orange line line to those obtained combining Planck $+ \omega(\theta) + $ SNIa. For the former we find $\Omega_{\rm m} = 0.317^{+0.011}_{-0.013}$ and $\gamma = 0.67 \pm 0.15$. Then, similar to what we obtain for the ΛCDM results, adding SNIa does not significantly improve the constraints, resulting in $\Omega_{\rm m} = 0.315 \pm 0.011$ and $\gamma = 0.68 \pm 0.14$. Both data-set combinations result in constraints that are in good agreement with GR within 1σ, as well as with our previous results for the basic ΛCDM case.
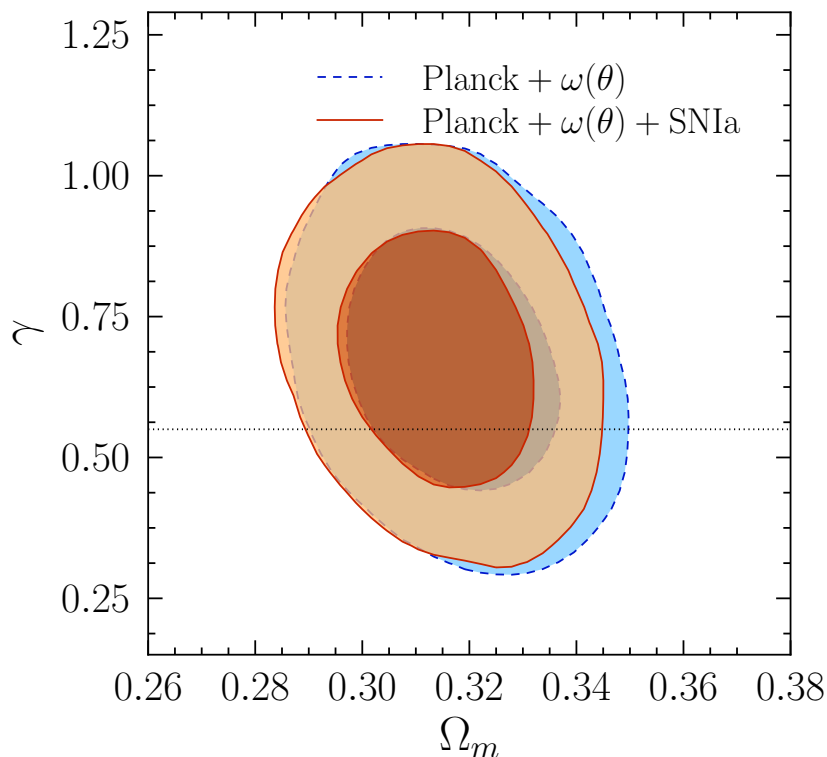
Figure 4.17: Marginalised 68% and 95% confidence interval constraints in the $\Omega_{\rm m} - \gamma$ plane. The blue dashed line corresponds to the constraints obtained by the Planck$+\omega(\theta)$ combination, and the solid orange line line to those obtained combining Planck $+ \omega(\theta) +$ SNIa. The dotted line shows the value of γ that recovers the GR prediction for the growth rate f, following equation (4.24).

Finally, constraints obtained also treating $w_{\rm DE}$ as a free parameter, assuming that it is constant in time, are listed in table B.9. Figure 4.18 shows the marginalised 68 and 95 per cent confidence interval constraints in the $w - \gamma$ plane. The vertical dotted line marks $w = -1$, while the other one follows equation (4.24). Using the Planck $+ \omega(\theta)$ combination, we obtain a value of $w = -0.980 \pm 0.092$ and $\gamma = 0.64^{+0.21}_{-0.23}$. Adding the information from SNIa tightens the constraints, resulting in $w = -1.013^{+0.052}_{-0.047}$ and $\gamma = 0.70^{+0.16}_{-0.18}$. Both sets of constraints are again in good agreement with the standard ΛCDM model and General Relativity.
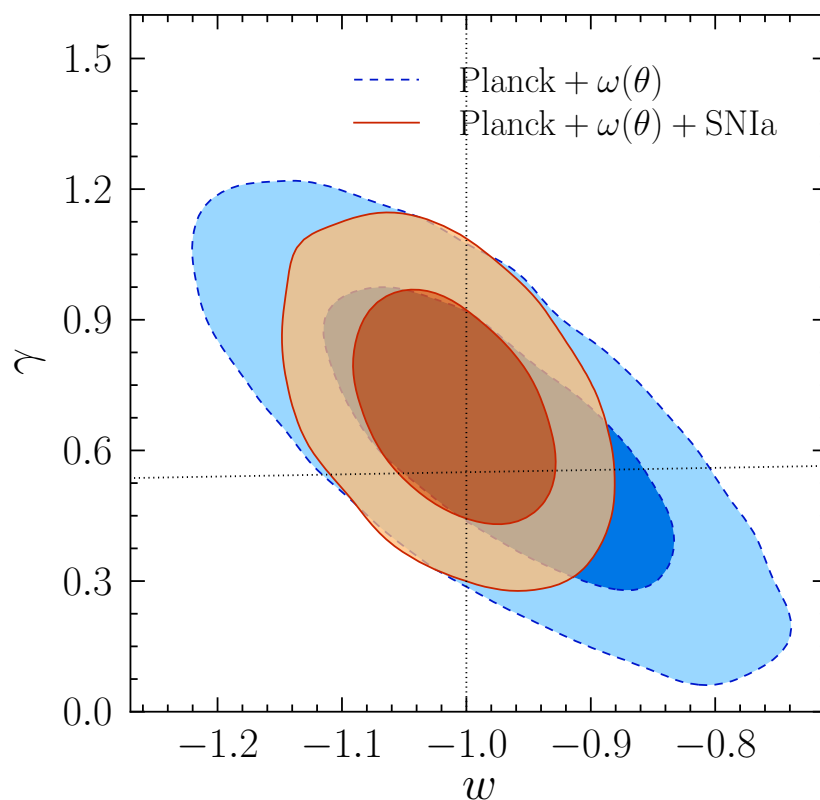
Figure 4.18: Marginalised 68% and 95% confidence interval constraints in the $w - \gamma$ plane. The blue dashed line corresponds to the constraints obtained by the Planck$+\omega(\theta)$ combination, and the solid orange line line to those obtained combining Planck $+ \omega(\theta) +$ SNIa. The (almost) horizontal dotted line shows the value of γ that recovers the GR prediction for the growth rate f, following equation (4.24).

Chapter 5

Conclusions

We tested the implications of applying a tomographic approach to a spectroscopic-redshift galaxy survey through measuring two-point angular correlation functions, $\omega(\theta)$, in thin redshift shells. In contrast with the traditional analysis of galaxy-clustering, which uses the 3D positions of galaxies, this technique avoids the need to assume a fiducial cosmological model in order to transform measured angular positions and redshifts into comoving distances. Also, this technique is able to trace the redshift evolution of the galaxy clustering signal, unlike the usual 3D analysis, which averages large cosmological volumes ignoring the so called *light-cone effects*. In principle, this technique, as it is presented in this work, can be also applied to narrow-band photometric surveys (e.g. PAU survey[1]) without any further consideration, since the accuracy in their photometric-redshifts determination is expected to be $\sim 0.0035(1+z)$.

We first tested the predictions of a model for $\omega(\theta)$ and its covariance matrix, described in §3.2, against measurements made on a set of 160 mock catalogues, and tested its ability to recover the correct value of the dark energy equation of state parameter w_{DE} used to construct these catalogues. For simplicity, we did not include cross-correlations between shells in our analysis, although they add extra information. Our modelling includes effects such as redshift-space distortions (RSD) and non-linear evolution of the density fluctuations, showing that they are absolutely necessary to correctly reproduce the full shape of $\omega(\theta)$. This technique results in an unbiased method to extract cosmological information.

Next, we made a forecast of the accuracy of the cosmological constraints expected from applying this technique to the final Baryon Oscillation Spectroscopic Survey galaxy catalogue, BOSS, in combination with the Planck CMB data. We tested this tomographic approach against the basic ΛCDM model, as

---

[1]http://www.pausurvey.org/

well as two extensions of it for alternative dark energy models. We compared the constraints obtained in these tests with what would result from combining Planck with traditional isotropic BAO measurements post-reconstruction on the same galaxy catalogue. To do so, we chose the best-fit of the base ΛCDM cosmology from Planck as our true cosmology and characterised the BOSS catalogue assuming an area of 10000 $\deg^2$, a constant $n(z)$ within the redshift range $0.2 < z < 0.6$, and the galaxy bias model in equation (3.36). Using the model for the angular correlation function and its covariance matrix, we constructed a synthetic dataset consisting of 16 measurements of $\omega(\theta)$ on the same number of redshift-shells covering the whole redshift range. We also computed the CMB likelihood using distance priors for Planck, and reproduced the likelihood obtained from BAO measurements post-reconstruction on BOSS using equation (3.40) and assuming an error of 2% for LOWZ and 1% for CMASS.

Across these tests, we used two different models for the redshift evolution of the galaxy bias. In one case, we used the same model assumed to construct the synthetic dataset, and in the other case, we used a simple linear model shown in equation (3.23). The different choices showed no biases when constraining cosmological parameters, but different accuracies. The first cosmological model tested was the basic ΛCDM, which resulted in tighter constraints for the combination of Planck and BAO measurements compared to the combination of Planck and $\omega(\theta)$. However, for the other two models tested, where we extended the base parameter-space allowing w_{DE} to deviate from its fiducial value of -1 (wCDM model), assuming it is constant in one case, and allowing a time-dependence in the other, we found that the more freedom we gave to w_{DE} the better performance our technique had. This results in an accuracy comparable to Planck+BAOs when constraining a constant w_{DE}, and in an up to 15% higher Figure-of-Merit (FoM) compared to the combination of Planck and BAO measurements in the case of a time-dependent dark energy equation of state, showing that our tomographic approach to analyse the galaxy clustering is able to put strong constraints on the expansion history of the Universe.

Afterwards, we applied this technique to the final BOSS galaxy sample. For this purpose, we extended our description of the full shape of $\omega(\theta)$ to use state-of-the-art modelling of non-linearities, galaxy bias and RSD. We also extended the analysis to include cross-correlation measurements between redshift shells.

In order to maximise the constraining power of our measurements, we optimised the number of redshift shells used in the analysis, by means of maximising the FoM in the $\Omega_{\mathrm{m}} - w$ plane. We did this exploring three different cases: (i) a Fisher-matrix approach that resulted in an monotonic increase in the FoM as a function of the number of shells; (ii) an MCMC analysis using

synthetic data, where we only varied $\Omega_{\rm m}$ and w, which showed a clear maximum in the FoM; and (iii), an analogous MCMC test, where we also included the nuisance parameters of the model, which resulted in the same behaviour as (ii), but with a smaller value for the FoM. We defined our binning scheme on the basis of the last case, where our final configuration consisted of 18 redshift shells of different widths, containing ~ 70000 galaxies each, plus as many cross-correlations, with subsequent shells, as necessary to surpass the BAO scale in the line of sight.

We tested our methodology against a set of 1000 MD-PATCHY mock catalogues, which are designed to match the characteristics of the final BOSS galaxy sample, following its angular and radial selection function, as well as including the redshift evolution of bias and RSD. Using the mean of the 1000 mock catalogues, we ran an MCMC analysis constraining very general cosmologies, using three different models for the evolution of the linear galaxy-bias. We were able to recover unbiased cosmological information for two of these models, and biased results at the 1σ level for the constant galaxy-clustering (CGC) model. Also, we repeated this test on a subset of 100 mocks using one of the galaxy-bias models that resulted in unbiased constraints, and performed an MCMC analysis on each mock catalogue individually. On these tests we found excellent agreement between the statistical errors and those estimated by our model for the full covariance matrix of $\omega(\theta)$.

Next, we analysed the redshift evolution of the linear bias of BOSS galaxies. Fixing the cosmological parameters to the best-fitting ΛCDM model to the final Planck CMB observations, we fit the linear bias parameter of our model for the galaxy-clustering signal, marginalising over the other nuisance parameters and σ_8 with a Planck prior. Also, using the same three different models for the redshift evolution of the linear galaxy-bias used in the previous tests, we fit the clustering amplitude of $\omega(\theta)$ in all redshift shells simultaneously. We saw that all three models are able to reproduce well the observed redshift evolution of the linear bias up to redshift $z \sim 0.6$, where the BOSS sample is close to a volume-limited one. However, none of them were able to reproduce the observed scatter in the measurements within $0.6 \lesssim z \lesssim 0.7$, where the BOSS sample behaves as flux-limited. For this reason, and because two of the three bias models depend on the linear growth factor $D(z)$, in order to avoid biased cosmological constraints, we decided not to include the measurements in these high-redshift shells in our tomographic analysis. We tested the impact that assuming these three models for the redshift evolution of the linear galaxy-bias has on the obtained constraints on cosmological parameters. Combining our measurements of $\omega(\theta)$ from BOSS with the CMB measurements from Planck, we obtained constraints on the wCDM parameter-space using each of the three

galaxy-bias models, and found no significant difference between them, showing that this analysis provide robust constraints.

Finally, combining the information obtained from the application of our to-mographic approach to the final BOSS galaxy sample, with the latest Planck CMB observations and type Ia supernova (SNIa), we constrain the parameters of the standard ΛCDM cosmological model and its more important extensions, including non-flat universes, more general dark energy models, neutrino masses, and possible deviations from the predictions of general relativity. In general, these constraints are comparable to the most precise present-day cosmological constraints in the literature, showing and consolidating the ΛCDM model as the standard cosmological paradigm.

In particular, in all the cases where we allow w_{DE} to deviate from its fiducial value of -1, either as constant or time-dependent, our final constraints are in good agreement to those cases where w_{DE} is fixed to -1. For the simplest wCDM extension we obtain $w_{\mathrm{DE}} = -0.958^{+0.063}_{-0.055}$ for the combination of our $\omega(\theta)$ measurements with Planck, and $w_{\mathrm{DE}} = -0.991 \pm 0.046$ for the full Planck $+ \omega(\theta) +$ SNIa combination. For models including Ω_{K}, with w fixed to -1 or treated as a free parameter, we find $|\Omega_{\mathrm{K}}| \sim 10^{-3}$, consistent with no curvature. Although we do not find a clear detection for the total sum of neutrino masses, we obtain upper limits that can be considered amongst the tightest ones available at present, where in the $\nu\Lambda$CDM case, we obtain $\sum m_\nu/\mathrm{eV} < 0.207(0.400)$ 68%(95%) confidence interval(C.I.) upper limits for the Planck$+\omega(\theta)$ combination, while for the full Planck$+\omega(\theta)+$SNIa case, we find $\sum m_\nu/\mathrm{eV} < 0.169(0.330)$ 68%(95%) C.I. upper limits. Furthermore, we see no significant deviations from the GR predictions of the linear growth of structures, parametrised by the growth index parameter γ, neither assuming a ΛCDM as the background cosmological model, nor when we also treat w_{DE} as a free parameter.

In summary, the methodology of analysing the large-scale structure of the Universe presented in this work, using angular galaxy-clustering measurements in thin redshift shells, is an excellent alternative to the traditional 3D clustering analysis. It avoids the two main issues of the traditional approach, by using cosmology-independent measurements, and by being able to trace the redshift evolution of the clustering signal. Furthermore, this technique is able to provide precise constraints on cosmological parameters, proving to be a valid and very robust method to analyse present and future large galaxy-surveys.

Appendix A

Overview of Random Variables and Spatial Statistics

In cosmology, the distribution of mass in the Universe can be described as a continuous random variable (random field). On the other hand the distribution of galaxies, which we can actually observe, is better described by a discrete (random) point process. A redshift galaxy survey is essentially a set of positions $\{\mathbf{x}_i\}_{i=1}^N$ of N objects (galaxies) in a volume V, that can be thought of as a realisation of such a random process, connected somehow to the underlying random (mass) field.

The most common statistical tools to study the clustering of galaxies are the two-point central moments, such as the correlation function and the power spectrum, that can be used to extract cosmological information from the observations.

This chapter aims to present the basic concepts required to understand how we use spatial statistics to characterise the large-scale structure of the Universe, and is not meant to be an extensive presentation of probability theory. For a more detailed description of the concepts presented here, two interesting books are Ripley (1981) and Papoulis (1984).

A.1 Probability Spaces

A probability space is a special case of a **measure space**, that is composed of three elements: a set Ω whose elements are called points (e.g. $\mathbb{R}$); a collection of subsets of Ω, Σ, called sigma-algebra (σ-algebra); and a measure μ defined on a σ-algebra. We will briefly describe these components here.

The σ-algebra

A collection Σ of subsets of Ω is called a σ-algebra, if it satisfies the three following axioms:

(i) If $A \in \Sigma$, then its complement $A^c \in \Sigma$, where $A^c = \Omega \cap A$.

(ii) If $\{A_i\}_{i=1}^{\infty}$ is a countable family of sets in Σ, then their union $\bigcup_{i=1}^{\infty} A_i$ also belongs to Σ.

(iii) The space $\Omega \in \Sigma$.

Note that the empty set $\varnothing = \Omega^c$ is also in Σ, which is important to define the measure later.

A special case is the *Borel* σ-algebra $\mathcal{B}$ of $\mathbb{R}^n$, which is the smallest sigma-algebra generated by the open balls of $\mathbb{R}^n$, that is the family of sets of the form

$$B_{\mathbf{x},R} := \{\mathbf{y} \in \mathbb{R}^n : |\mathbf{x} - \mathbf{y}| < R\}. \tag{A.1}$$

Measure, measure spaces and measurable functions

A measure $\mu : \Sigma \to \mathbb{R}_0^+$, defined on a sigma-algebra Σ, is a function from Σ to the non-negative real numbers (including infinity) such that

(i) $\mu(\varnothing) = 0$, and

(ii) If $\{A_i\}_{i=1}^{\infty}$ is a sequence of **disjoint** (i.e. $A_i \cap A_j = \varnothing$ for $i \neq j$) sets in Σ, then

$$\mu\left(\bigcup_{i=1}^{\infty} A_i\right) = \sum_{i=1}^{\infty} \mu(A_i), \tag{A.2}$$

where this last point is called *countable additivity*. Two important consequences of (A.2) for probability theory are that

(i) If $A \subset B$, then $\mu(A) \leq \mu(B)$, and

(ii) $\mu(A_1 \cup A_2) = \mu(A_1) + \mu(A_2) - \mu(A_1 \cap A_2)$.

As we said above then, a **measure space** (Ω, Σ, μ) is composed by three elements: a set Ω, a σ-algebra Σ and a measure μ. Also, a function between two measure spaces is a **measurable function** if the pre-image of each measurable set is also measurable. That is, let (Ω, Σ, μ) and (Ω', Σ', μ') be two measure spaces, then $f : \Sigma \to \Sigma'$ is measurable if

$$f^{-1}(A) := \{\omega \in \Omega : f(\omega) \in A\} \in \Sigma \quad \forall A \in \Sigma'. \tag{A.3}$$

Finally, a **probability space** (Ω, Σ, P) is a measure space, where its (probability) measure P is normalised such that $P(\Omega) = 1$.

A.2 Random Variables

From this point on, we shall restrict our discussion to scalar random variables with domain in $\mathbb{R}^n$, but it can be easily extended to vectors or tensors by treating each component as a scalar random variable. Let $(\mathbb{R}^n, \mathcal{B}, P)$ be a probability space. Let $Y : \mathbb{R}^n \to \mathbb{R}$ be a real single-valued measurable function defined for every $\mathbf{x} \in \mathbb{R}^n$ such that for all $y \in \mathbb{R}$,

$$R_y := \{\mathbf{x} \in \mathbb{R}^n : Y(\mathbf{x}) \leq y\} \tag{A.4}$$

belongs to $\mathcal{B}$. Then, the function $Y(\mathbf{x})$ is called a random variable. We can think of a random variable as being just a mapping with the property that inverse images determined by the random variable are events in the original space. This simple property ensures that the output of the random variable will inherit its own distribution (or probability measure), which we will introduce now.

A **probability distribution**, or cumulative distribution function, $F_Y(y)$, is defined as

$$F_Y(y) := P(\{y \in \mathbb{R} : Y \leq y\}), \tag{A.5}$$

which is usually referred to as *the probability* of Y being less or equal to y, or *the measure* P of the set $\{y \in \mathbb{R} : Y \leq y\}$. If $F_Y(y)$ is differentiable, then the **probability density distribution** exists, and is given by

$$f_Y(y) = \frac{dF_Y(y)}{dy} \quad \Rightarrow \quad F_Y(y) = \int_{-\infty}^{y} dy f_Y(y) \tag{A.6}$$

Using $f(y)$, we may calculate the probability for any interval $y_1 \leq Y \leq y_2$ as

$$P(\{y_1 \in \mathbb{R} : y_1 \leq Y\} \cap \{y_2 \in \mathbb{R} : Y \leq y_2\}) = F_Y(y_2) - F_Y(y1)$$
$$= \int_{y_1}^{y_2} dy f_Y(y). \tag{A.7}$$

For our purposes, we can think of a scalar random field as well as a random point process as a set of random variables as defined above, together with a collection of distribution functions $P(\{y_i \in \mathbb{R} : Y(\mathbf{x}_i) \leq y_i\}_{i=1}^N)$, for any number of points N. They will differ in that we may impose continuity for a random field, while a random point process has to be discrete, in the sense that for any region $A \subset \mathbb{R}^n$, there has to be a finite, countable number of points N_A. The relation between the two can be described by an inhomogeneous Poisson point process with density $n(\mathbf{x})$ as

$$n(\mathbf{x}) = \sum_{i=1}^{N} w_i \delta_D^n(\mathbf{x} - \mathbf{x}_i), \tag{A.8}$$

where $\delta_D^n(\mathbf{x})$ is the Dirac delta function, and w_i is some weight to be defined from the underlying field (e.g. the mass density contrast at $\mathbf{x}_i$). For this reason, in the following we will assume $Y(\mathbf{x})$ is a random continuous random field.

A.3   Spatial correlations

Let us start by defining the expected value of $g(Y)$ as

$$\langle g(Y) \rangle := \int dy g(Y) f_Y(y), \tag{A.9}$$

where $f_Y(y)$ is the probability density function of Y as defined above. Using this, we can define the first moment of a random field $Y(\mathbf{x})$, its mean, as

$$m(\mathbf{x}) = \langle Y(\mathbf{x}) \rangle, \tag{A.10}$$

The second moment is the two-point non-central covariance function $R_2(\mathbf{x}_i, \mathbf{x}_j)$, defined as

$$R_2(\mathbf{x}_i, \mathbf{x}_j) = \langle Y(\mathbf{x}_i)Y(\mathbf{x}_j) \rangle. \tag{A.11}$$

From (A.10) and (A.11) we can define the central two-point covariance function, $\xi(\mathbf{x}_i, \mathbf{x}_j)$, or the **correlation function**, as

$$\xi(\mathbf{x}_i, \mathbf{x}_j) = \langle [Y(\mathbf{x}_i) - m(\mathbf{x}_i)][Y(\mathbf{x}_j) - m(\mathbf{x}_j)] \rangle. \tag{A.12}$$

The correlation functions is positive definite, which is important as it allows us to represent it as a Fourier integral.

Analogously to the two-point covariance function, we can define all the higher-order non-central n-point covariance functions as

$$R_n(\mathbf{x}_1, ..., \mathbf{x}_n) = \langle Y(\mathbf{x}_1)...Y(\mathbf{x}_n) \rangle, \tag{A.13}$$

and the higher-order central n-point covariance functions by

$$\mu_n(\mathbf{x}_1, .., \mathbf{x}_n) = \langle [Y(\mathbf{x}_1) - m(\mathbf{x}_1)]...[Y(\mathbf{x}_n) - m(\mathbf{x}_n)] \rangle. \tag{A.14}$$

These functions contain all the higher-order moments of the one-point probability distributions when its arguments coincide, meaning that the knowledge of all covariance functions is sufficient to completely describe a random field.

At this point, we shall introduce homogeneity and isotropy of a random field in terms of its first and second moments. Homogeneous random fields are those where all distribution functions (and moments) are invariant under

translations. In particular, its mean m will not depend on the position $\mathbf{x}$, and its correlation function will only depend on the separation vector $\mathbf{r} \equiv \mathbf{x}_i - \mathbf{x}_j$, thus

$$\xi(\mathbf{x}_i, \mathbf{x}_j) \equiv \xi(\mathbf{r}). \tag{A.15}$$

Isotropic random fields are defined by requiring that its correlation function does not depend on the direction, that is

$$\xi(\mathbf{x}, \mathbf{x} + \mathbf{r}) \equiv \xi(\mathbf{x}, r), \tag{A.16}$$

where $r = |\mathbf{r}|$. In cosmology, the matter density field of the Universe is thought to be both homogeneous and isotropic (this is known as the cosmological principle), which means that the correlation function will be a function of the separation only $\xi(\mathbf{x}, \mathbf{x} + \mathbf{r}) \equiv \xi(r)$.

A.4 The spectral representation

In linear algebra and functional analysis, the spectral theorem states conditions under which operators can be diagonalisable. In the case of a homogeneous, zero-mean, continuous random field, it can be decomposed as a sum of regular underlying oscillations whose magnitudes are independent (i.e. uncorrelated) random variables, a characteristic that greatly simplifies the study of the random process. Mathematically, we can express it by

$$Y(\mathbf{x}) = \int_{\mathbb{R}^n} dZ(\mathbf{k}) \ e^{-i\mathbf{x}\cdot\mathbf{k}}, \tag{A.17}$$

and in the case that the field $Z(\mathbf{k})$ is differentiable, it can be written in terms of its density as $dZ(\mathbf{k}) = \frac{d^n k}{(2\pi)^n} \tilde{Y}(\mathbf{k})$, reducing $Y(\mathbf{x})$ and $\tilde{Y}(\mathbf{k})$ into a Fourier pair:

$$\begin{aligned} \tilde{Y}(\mathbf{k}) &= \int_{\mathbb{R}^n} d^n x \ Y(\mathbf{x}) e^{-i\mathbf{k}\cdot\mathbf{x}}, \\[6pt] Y(\mathbf{x}) &= \int_{\mathbb{R}^n} \frac{d^n k}{(2\pi)^n} \ \tilde{Y}(\mathbf{k}) e^{i\mathbf{x}\cdot\mathbf{k}}. \end{aligned} \tag{A.18}$$

Given that the field $\tilde{Y}(\mathbf{k})$ is independent, it is possible to express it second moment as

$$\langle \tilde{Y}(\mathbf{k}_i)\tilde{Y}^*(\mathbf{k}_j) \rangle = (2\pi)^n P(\mathbf{k}_i)\delta_D^n(\mathbf{k}_i - \mathbf{k}_j), \tag{A.19}$$

where $P(\mathbf{k})$ is the spectral density function of the field, also called in cosmology **the power spectrum**.

Analogously, the spectral theorem describes regular oscillations within the random fluctuation of a homogeneous stochastic process through such oscillations in its autocorrelation function. In practice, this means that $\xi(\mathbf{r})$ and $P(\mathbf{k})$ are also a Fourier pair, holding

$$\xi(\mathbf{r}) = \int_{\mathbb{R}^n} \frac{d^n k}{(2\pi)^n} \, P(\mathbf{k}) e^{-i\mathbf{r}\cdot\mathbf{k}}. \tag{A.20}$$

This relation can be derived from (A.11) and (A.18) as well.

If the field is also isotropic (its covariance function does not depend on the direction), and if we work on $\mathbb{R}^3$, the relation above can be integrated over the angles resulting in

$$\xi(r) = 4\pi \int_{\mathbb{R}_0^+} \frac{k^2 dk}{(2\pi)^3} \, P(k) \frac{\sin(kr)}{kr}. \tag{A.21}$$

A.5   Gaussian random fields

In the standard theory of cosmological structure formation, the initial mass density fluctuations arise from Gaussian quantum fluctuations of physical fields during inflation, that are naturally real homogenous isotropic random fields. This characteristic is of great importance, since it allows us to infer the statistical properties of the Universe from a single realisation.

Gaussian random fields are those whose probability density functions is a Gaussian (or normal) distribution, given by

$$f_{\mathbf{Y}}(\mathbf{y}) = \frac{1}{\sqrt{(2\pi)^k |\mathsf{C}|}} e^{-\frac{1}{2}(\mathbf{y}-\langle\mathbf{Y}\rangle)^T \mathsf{C}^{-1}(\mathbf{y}-\langle\mathbf{Y}\rangle)}, \tag{A.22}$$

where $\mathbf{Y}(\mathbf{x})$ is a k-dimensional (column) random vector, and $|\mathsf{C}|$ is the determinant of the covariance matrix C given by $C_{ij} = \xi(\mathbf{x}_i, \mathbf{x}_j)$.

Gaussian random fields have useful properties. One of them is that, if $\mathbf{Y}(\mathbf{x})$ is a Gaussian random field, then its Fourier pair $\tilde{\mathbf{Y}}(\mathbf{k})$ is Gaussian as well. Another important property of Gaussian random fields is that all odd higher-order central moments are zero, while even higher-order central moments are completely determined by the second-order central moment.

A.6   Ergodicity

In cosmology, since we only have a single realisation of the Universe, we usually need to assume the *fair sample hypothesis* (as in Peebles, 1980), that implies

homogeneity, isotropy (the cosmological principle) and **ergodicity**. A stochastic process is called ergodic if its statistical properties can be obtained from a sufficiently large random sample. In other words, averages taken over a large number of events tend to the ensemble average. For instance, consider a set $\{Y_i\}_{i=1}^N$ of N random variables with mean $\langle Y \rangle = \mu$, such that their average is

$$\frac{1}{N} \sum_{i=1}^N Y_i = \mu + \varepsilon. \tag{A.23}$$

Then, the process will be ergodic on the mean, if $\varepsilon \to 0$ for $N \to \infty$. In particular, Gaussian random fields are ergodic if their spectral density (or power spectrum in cosmology) is everywhere continuous. Equivalently, the condition that the covariance function $R_2(\mathbf{r}) \to 0$ for $r \to \infty$ implies ergodicity.

Appendix B

Tables

This section contains the summary tables from chapter 4. It includes tables displaying the cosmological parameters explored, that have been removed from the body of this work for readability, as well as tables describing the redshift-binning scheme used for the analysis of the final BOSS galaxy catalogue.

Parameter	CMB + $\omega(\theta)$	CMB + $\omega(\theta)$ + SNIa
$\Omega_b h^2$	0.02215 ± 0.00021	0.02217 ± 0.00021
$\Omega_c h^2$	0.1204 ± 0.0019	0.1200 ± 0.0018
$100\theta_{\mathrm{MC}}$	1.04078 ± 0.00045	1.04080 ± 0.00043
τ	0.070 ± 0.018	0.072 ± 0.018
$\ln(10^{10} A_s)$	3.075 ± 0.034	3.077 ± 0.035
n_s	0.9631 ± 0.0053	0.9637 ± 0.0053
H_0	66.98 ± 0.80	67.14 ± 0.77
Ω_Λ	0.681 ± 0.011	0.683 ± 0.011
Ω_{m}	0.319 ± 0.011	0.317 ± 0.011
σ_8	0.825 ± 0.014	0.825 ± 0.014
Age/Gyr	13.826 ± 0.033	13.822 ± 0.032

Table B.1: Marginalised constraints on the cosmological parameters for the ΛCDM model. Values correspond to the mean and 68% confidence interval. The first block corresponds to varied parameters in the analysis, while the second block are derived parameters.

Parameter	CMB + $\omega(\theta)$	CMB + $\omega(\theta)$ + SNIa
$\Omega_b h^2$	0.02220 ± 0.00022	0.02219 ± 0.00022
$\Omega_c h^2$	0.1198 ± 0.0021	0.1199 ± 0.0021
$100\theta_{\mathrm{MC}}$	1.04087 ± 0.00045	1.04085 ± 0.00046
τ	0.076 ± 0.019	0.074 ± 0.019
w	$-0.958^{+0.063}_{-0.055}$	-0.991 ± 0.046
$\ln(10^{10}A_s)$	3.087 ± 0.037	3.081 ± 0.036
n_s	0.9647 ± 0.0059	0.9645 ± 0.0059
H_0	66.0 ± 1.5	66.9 ± 1.1
Ω_Λ	0.672 ± 0.016	$0.681^{+0.013}_{-0.011}$
Ω_{m}	0.328 ± 0.016	0.319 ± 0.012
σ_8	0.816 ± 0.020	0.823 ± 0.019
Age/Gyr	13.844 ± 0.040	13.825 ± 0.034

Table B.2: Marginalised constraints on the cosmological parameters for the wCDM model. Values correspond to the mean and 68% confidence interval. The first block corresponds to varied parameters in the analysis, while the second block are derived parameters.

Parameter	CMB + $\omega(\theta)$	CMB + $\omega(\theta)$ + SNIa
$\Omega_b h^2$	0.02220 ± 0.00022	0.02216 ± 0.00022
$\Omega_c h^2$	0.1199 ± 0.0022	0.1199 ± 0.0021
$100\theta_{\mathrm{MC}}$	1.04084 ± 0.00048	1.04084 ± 0.00044
τ	0.076 ± 0.019	0.074 ± 0.019
w_0	$-0.60^{+0.24}_{-0.10}$	-0.94 ± 0.13
w_a	< -0.965	$-0.23^{+0.51}_{-0.42}$
$\ln(10^{10}A_s)$	3.087 ± 0.036	3.082 ± 0.036
n_s	0.9647 ± 0.0061	0.9637 ± 0.0060
H_0	$64.3^{+1.3}_{-1.8}$	67.0 ± 1.2
Ω_Λ	$0.654^{+0.017}_{-0.019}$	0.681 ± 0.012
Ω_{m}	$0.346^{+0.019}_{-0.017}$	0.319 ± 0.012
σ_8	0.806 ± 0.021	0.825 ± 0.018
Age/Gyr	13.790 ± 0.046	$13.811^{+0.047}_{-0.055}$

Table B.3: Marginalised constraints on the cosmological parameters for the w_0w_aCDM model. Values correspond to the mean and 68% confidence interval. The first block corresponds to varied parameters in the analysis, while the second block are derived parameters.

Parameter	CMB $+\ \omega(\theta)$	CMB $+\ \omega(\theta)$ + SNIa
$\Omega_b h^2$	0.02230 ± 0.00026	0.02229 ± 0.00026
$\Omega_c h^2$	0.1189 ± 0.0022	$0.1192^{+0.0022}_{-0.0026}$
$100\theta_{\mathrm{MC}}$	1.04100 ± 0.00049	$1.04102^{+0.00055}_{-0.00049}$
τ	0.076 ± 0.020	$0.074^{+0.016}_{-0.021}$
Ω_{K}	$-0.0043^{+0.0042}_{-0.0035}$	-0.0028 ± 0.0038
$\ln(10^{10} A_s)$	3.085 ± 0.039	$3.080^{+0.032}_{-0.038}$
n_s	$0.9671^{+0.0059}_{-0.0073}$	$0.9663^{+0.0071}_{-0.0061}$
H_0	$65.7^{+1.5}_{-1.3}$	66.3 ± 1.2
Ω_Λ	0.676 ± 0.013	$0.679^{+0.013}_{-0.0093}$
Ω_{m}	$0.329^{+0.014}_{-0.016}$	$0.324^{+0.011}_{-0.014}$
σ_8	0.823 ± 0.015	0.822 ± 0.014
Age/Gyr	$13.99^{+0.14}_{-0.17}$	13.93 ± 0.14

Table B.4: Marginalised constraints on the cosmological parameters for the oCDM model. Values correspond to the mean and 68% confidence interval. The first block corresponds to varied parameters in the analysis, while the second block are derived parameters.

Parameter	CMB $+\ \omega(\theta)$	CMB $+\ \omega(\theta)$ + SNIa
$\Omega_b h^2$	0.02227 ± 0.00025	0.02230 ± 0.00024
$\Omega_c h^2$	0.1193 ± 0.0022	0.1187 ± 0.0022
$100\theta_{\mathrm{MC}}$	1.04095 ± 0.00045	1.04097 ± 0.00049
τ	0.076 ± 0.019	0.073 ± 0.019
Ω_{K}	$-0.0037^{+0.0057}_{-0.0051}$	$-0.0040^{+0.0054}_{-0.0041}$
w	$-1.00^{+0.10}_{-0.075}$	$-1.025^{+0.064}_{-0.055}$
$\ln(10^{10} A_s)$	3.084 ± 0.037	3.077 ± 0.036
n_s	0.9657 ± 0.0064	0.9675 ± 0.0063
H_0	$65.7^{+1.3}_{-1.5}$	66.5 ± 1.3
Ω_Λ	0.673 ± 0.017	0.684 ± 0.013
Ω_{m}	0.330 ± 0.016	0.320 ± 0.014
σ_8	0.822 ± 0.023	0.825 ± 0.019
Age/Gyr	$13.99^{+0.17}_{-0.22}$	$13.98^{+0.16}_{-0.21}$

Table B.5: Marginalised constraints on the cosmological parameters for the woCDM model. Values correspond to the mean and 68% confidence interval. The first block corresponds to varied parameters in the analysis, while the second block are derived parameters.

Parameter	CMB + $\omega(\theta)$	CMB + $\omega(\theta)$ + SNIa
$\Omega_b h^2$	0.02214 ± 0.00021	0.02219 ± 0.00021
$\Omega_c h^2$	0.1200 ± 0.0020	0.1197 ± 0.0019
$100\theta_{\mathrm{MC}}$	1.04079 ± 0.00044	1.04085 ± 0.00045
τ	0.076 ± 0.019	0.077 ± 0.019
$\Sigma m_\nu/\mathrm{eV}$	$< 0.400(95\%\mathrm{C.I.})$	$< 0.330(95\%\mathrm{C.I.})$
$\ln(10^{10}A_s)$	3.086 ± 0.037	3.087 ± 0.037
n_s	0.9633 ± 0.0055	0.9643 ± 0.0054
H_0	$66.2^{+1.2}_{-1.0}$	$66.6^{+1.1}_{-0.93}$
Ω_Λ	$0.671^{+0.017}_{-0.013}$	$0.677^{+0.015}_{-0.012}$
Ω_{m}	$0.329^{+0.013}_{-0.017}$	$0.323^{+0.012}_{-0.015}$
σ_8	$0.804^{+0.031}_{-0.023}$	$0.810^{+0.028}_{-0.019}$
Age/Gyr	$13.876^{+0.051}_{-0.071}$	$13.854^{+0.047}_{-0.062}$

Table B.6: Marginalised constraints on the cosmological parameters for the $\nu\Lambda$CDM model. Values correspond to the mean and 68% confidence interval (C.I.), except for the sum of neutrino masses where 95% C.I. upper limits are shown (for 68% C.I. see text). The first block corresponds to varied parameters in the analysis, while the second block are derived parameters.

Parameter	CMB + $\omega(\theta)$	CMB + $\omega(\theta)$ + SNIa
$\Omega_b h^2$	0.02216 ± 0.00023	0.02215 ± 0.00022
$\Omega_c h^2$	0.1199 ± 0.0021	0.1198 ± 0.0021
$100\theta_{\mathrm{MC}}$	1.04081 ± 0.00048	1.04080 ± 0.00047
τ	0.078 ± 0.019	0.077 ± 0.019
$\Sigma m_\nu/\mathrm{eV}$	$< 0.486(95\%\mathrm{C.I.})$	$< 0.474(95\%\mathrm{C.I.})$
w	$-0.998^{+0.097}_{-0.064}$	$-1.023^{+0.063}_{-0.053}$
$\ln(10^{10}A_s)$	3.090 ± 0.037	3.086 ± 0.036
n_s	0.9636 ± 0.0064	0.9635 ± 0.0060
H_0	$66.1^{+1.5}_{-1.7}$	66.7 ± 1.1
Ω_Λ	0.670 ± 0.017	$0.676^{+0.015}_{-0.013}$
Ω_{m}	0.330 ± 0.017	$0.324^{+0.013}_{-0.015}$
σ_8	$0.801^{+0.028}_{-0.024}$	$0.805^{+0.030}_{-0.024}$
Age/Gyr	$13.882^{+0.054}_{-0.067}$	$13.871^{+0.051}_{-0.072}$

Table B.7: Marginalised constraints on the cosmological parameters for the νwCDM model. Values correspond to the mean and 68% confidence interval (C.I.), except for the sum of neutrino masses where 95% C.I. upper limits are shown (for 68% C.I. see text). The first block corresponds to varied parameters in the analysis, while the second block are derived parameters.

Parameter	CMB + $\omega(\theta)$	CMB + $\omega(\theta)$ + SNIa
$\Omega_b h^2$	0.02219 ± 0.00022	0.02221 ± 0.00021
$\Omega_c h^2$	0.1201 ± 0.0020	0.1197 ± 0.0019
$100\theta_{\mathrm{MC}}$	1.04084 ± 0.00046	1.04088 ± 0.00045
τ	0.075 ± 0.019	0.077 ± 0.019
$\ln(10^{10}A_s)$	3.084 ± 0.036	3.086 ± 0.036
n_s	0.9641 ± 0.0057	0.9650 ± 0.0055
γ	0.67 ± 0.15	0.68 ± 0.14
H_0	67.15 ± 0.87	67.33 ± 0.82
Ω_Λ	$0.683^{+0.013}_{-0.011}$	0.685 ± 0.011
Ω_{m}	$0.317^{+0.011}_{-0.013}$	0.315 ± 0.011
σ_8	0.828 ± 0.014	0.828 ± 0.015
Age/Gyr	13.819 ± 0.036	13.813 ± 0.034

Table B.8: Marginalised constraints on the cosmological parameters for the $\gamma\Lambda$CDM model. Values correspond to the mean and 68% confidence interval. The first block corresponds to varied parameters in the analysis, while the second block are derived parameters.

Parameter	CMB + $\omega(\theta)$	CMB + $\omega(\theta)$ + SNIa
$\Omega_b h^2$	0.02220 ± 0.00022	0.02220 ± 0.00022
$\Omega_c h^2$	0.1199 ± 0.0021	0.1200 ± 0.0020
$100\theta_{\mathrm{MC}}$	1.04086 ± 0.00046	1.04088 ± 0.00045
τ	0.076 ± 0.019	0.076 ± 0.019
w	-0.980 ± 0.092	$-1.013^{+0.052}_{-0.047}$
$\ln(10^{10} A_s)$	3.086 ± 0.037	3.086 ± 0.036
n_s	0.9644 ± 0.0060	0.9643 ± 0.0059
γ	$0.64^{+0.21}_{-0.23}$	$0.70^{+0.16}_{-0.18}$
H_0	66.6 ± 2.5	67.6 ± 1.3
Ω_Λ	$0.677^{+0.027}_{-0.022}$	0.687 ± 0.013
Ω_{m}	$0.323^{+0.022}_{-0.027}$	0.313 ± 0.013
σ_8	0.822 ± 0.030	0.832 ± 0.020
Age/Gyr	$13.832^{+0.053}_{-0.064}$	13.809 ± 0.037

Table B.9: Marginalised constraints on the cosmological parameters for the γwCDM model. Values correspond to the mean and 68% confidence interval. The first block corresponds to varied parameters in the analysis, while the second block are derived parameters.

$z_{\min}$	$z_{\max}$	Δz	used
0.20000	0.25841	0.05841	yes
0.25841	0.30813	0.04972	yes
0.30813	0.34266	0.03453	yes
0.34266	0.37622	0.03356	yes
0.37622	0.41421	0.03799	yes
0.41421	0.44550	0.03129	yes
0.44550	0.46670	0.02121	yes
0.46670	0.48305	0.01635	yes
0.48305	0.49783	0.01478	yes
0.49783	0.51177	0.01394	yes
0.51177	0.52580	0.01403	yes
0.52580	0.54021	0.01442	yes
0.54021	0.55550	0.01529	yes
0.55550	0.57185	0.01635	yes
0.57185	0.59103	0.01918	yes
0.59103	0.61356	0.02253	no
0.61356	0.64375	0.03018	no
0.64375	0.75000	0.10625	no

Table B.10: Redshift limits and Δz of the 18 z-shells found to be the optimal binning scheme for this tomographic analysis of this paper, form which the three higher redshift were not used. In all the figures, the redshift limits are shown only to three decimal points.

	1	2	3	4	5	6	7	8	9	10	11	12	13	14	15
1	×														
2		×													
3			×	×											
4				×	×										
5					×	×									
6						×	×								
7							×	×	×	×					
8								×	×	×	×				
9									×	×	×	×			
10										×	×	×	×		
11											×	×	×	×	
12												×	×	×	×
13													×	×	×
14														×	×
15															×

Table B.11: Configuration matrix of the auto- and cross-correlation functions used in the analysis of the cosmological implications of $\omega(\theta)$ measured on BOSS. Crosses indicate the measurements used, where the diagonal terms are the auto-correlations, and off-diagonal terms correspond to the cross-correlations included.

Bibliography

Abazajian, K. N., Adelman-McCarthy, J. K., Agüeros, M. A., Allam, S. S., Allende Prieto, C., An, D., Anderson, K. S. J., Anderson, S. F., Annis, J., Bahcall, N. A., and et al. (2009). The Seventh Data Release of the Sloan Digital Sky Survey. *ApJS*, 182:543–558. 26

Ahmad, Q. R., Allen, R. C., Andersen, T. C., Anglin, J. D., Barton, J. C., Beier, E. W., Bercovitch, M., Bigu, J., Biller, S. D., Black, R. A., Blevis, I., Boardman, R. J., Boger, J., Bonvin, E., Boulay, M. G., Bowler, M. G., Bowles, T. J., Brice, S. J., Browne, M. C., Bullard, T. V., Bühler, G., Cameron, J., Chan, Y. D., Chen, H. H., Chen, M., Chen, X., Cleveland, B. T., Clifford, E. T., Cowan, J. H., Cowen, D. F., Cox, G. A., Dai, X., Dalnoki-Veress, F., Davidson, W. F., Doe, P. J., Doucas, G., Dragowsky, M. R., Duba, C. A., Duncan, F. A., Dunford, M., Dunmore, J. A., Earle, E. D., Elliott, S. R., Evans, H. C., Ewan, G. T., Farine, J., Fergani, H., Ferraris, A. P., Ford, R. J., Formaggio, J. A., Fowler, M. M., Frame, K., Frank, E. D., Frati, W., Gagnon, N., Germani, J. V., Gil, S., Graham, K., Grant, D. R., Hahn, R. L., Hallin, A. L., Hallman, E. D., Hamer, A. S., Hamian, A. A., Handler, W. B., Haq, R. U., Hargrove, C. K., Harvey, P. J., Hazama, R., Heeger, K. M., Heintzelman, W. J., Heise, J., Helmer, R. L., Hepburn, J. D., Heron, H., Hewett, J., Hime, A., Howe, M., Hykawy, J. G., Isaac, M. C., Jagam, P., Jelley, N. A., Jillings, C., Jonkmans, G., Kazkaz, K., Keener, P. T., Klein, J. R., Knox, A. B., Komar, R. J., Kouzes, R., Kutter, T., Kyba, C. C., Law, J., Lawson, I. T., Lay, M., Lee, H. W., Lesko, K. T., Leslie, J. R., Levine, I., Locke, W., Luoma, S., Lyon, J., Majerus, S., Mak, H. B., Maneira, J., Manor, J., Marino, A. D., McCauley, N., McDonald, A. B., McDonald, D. S., McFarlane, K., McGregor, G., Meijer Drees, R., Mifflin, C., Miller, G. G., Milton, G., Moffat, B. A., Moorhead, M., Nally, C. W., Neubauer, M. S., Newcomer, F. M., Ng, H. S., Noble, A. J., Norman, E. B., Novikov, V. M., O'Neill, M., Okada, C. E., Ollerhead, R. W., Omori, M., Orrell, J. L., Oser, S. M., Poon, A. W., Radcliffe, T. J., Roberge, A., Robertson, B. C., Robertson, R. G., Rosendahl, S. S., Rowley, J. K.,

Rusu, V. L., Saettler, E., Schaffer, K. K., Schwendener, M. H., Schülke, A., Seifert, H., Shatkay, M., Simpson, J. J., Sims, C. J., Sinclair, D., Skensved, P., Smith, A. R., Smith, M. W., Spreitzer, T., Starinsky, N., Steiger, T. D., Stokstad, R. G., Stonehill, L. C., Storey, R. S., Sur, B., Tafirout, R., Tagg, N., Tanner, N. W., Taplin, R. K., Thorman, M., Thornewell, P. M., Trent, P. T., Tserkovnyak, Y. I., van Berg, R., van de Water, R. G., Virtue, C. J., Waltham, C. E., Wang, J.-X., Wark, D. L., West, N., Wilhelmy, J. B., Wilkerson, J. F., Wilson, J. R., Wittich, P., Wouters, J. M., and Yeh, M. (2002). Direct Evidence for Neutrino Flavor Transformation from Neutral-Current Interactions in the Sudbury Neutrino Observatory. *Physical Review Letters*, 89(1):011301. 74

Ahmad, Q. R., Allen, R. C., Andersen, T. C., Anglin, J. D., Bühler, G., Barton, J. C., Beier, E. W., Bercovitch, M., Bigu, J., Biller, S., Black, R. A., Blevis, I., Boardman, R. J., Boger, J., Bonvin, E., Boulay, M. G., Bowler, M. G., Bowles, T. J., Brice, S. J., Browne, M. C., Bullard, T. V., Burritt, T. H., Cameron, K., Cameron, J., Chan, Y. D., Chen, M., Chen, H. H., Chen, X., Chon, M. C., Cleveland, B. T., Clifford, E. T., Cowan, J. H., Cowen, D. F., Cox, G. A., Dai, Y., Dai, X., Dalnoki-Veress, F., Davidson, W. F., Doe, P. J., Doucas, G., Dragowsky, M. R., Duba, C. A., Duncan, F. A., Dunmore, J., Earle, E. D., Elliott, S. R., Evans, H. C., Ewan, G. T., Farine, J., Fergani, H., Ferraris, A. P., Ford, R. J., Fowler, M. M., Frame, K., Frank, E. D., Frati, W., Germani, J. V., Gil, S., Goldschmidt, A., Grant, D. R., Hahn, R. L., Hallin, A. L., Hallman, E. D., Hamer, A., Hamian, A. A., Haq, R. U., Hargrove, C. K., Harvey, P. J., Hazama, R., Heaton, R., Heeger, K. M., Heintzelman, W. J., Heise, J., Helmer, R. L., Hepburn, J. D., Heron, H., Hewett, J., Hime, A., Howe, M., Hykawy, J. G., Isaac, M. C., Jagam, P., Jelley, N. A., Jillings, C., Jonkmans, G., Karn, J., Keener, P. T., Kirch, K., Klein, J. R., Knox, A. B., Komar, R. J., Kouzes, R., Kutter, T., Kyba, C. C., Law, J., Lawson, I. T., Lay, M., Lee, H. W., Lesko, K. T., Leslie, J. R., Levine, I., Locke, W., Lowry, M. M., Luoma, S., Lyon, J., Majerus, S., Mak, H. B., Marino, A. D., McCauley, N., McDonald, A. B., McDonald, D. S., McFarlane, K., McGregor, G., McLatchie, W., Drees, R. M., Mes, H., Mifflin, C., Miller, G. G., Milton, G., Moffat, B. A., Moorhead, M., Nally, C. W., Neubauer, M. S., Newcomer, F. M., Ng, H. S., Noble, A. J., Norman, E. B., Novikov, V. M., O'Neill, M., Okada, C. E., Ollerhead, R. W., Omori, M., Orrell, J. L., Oser, S. M., Poon, A. W., Radcliffe, T. J., Roberge, A., Robertson, B. C., Robertson, R. G., Rowley, J. K., Rusu, V. L., Saettler, E., Schaffer, K. K., Schuelke, A., Schwendener, M. H., Seifert, H., Shatkay, M., Simpson, J. J., Sinclair, D., Skensved, P., Smith, A. R., Smith, M. W., Starinsky, N., Steiger, T. D., Stokstad, R. G.,

Storey, R. S., Sur, B., Tafirout, R., Tagg, N., Tanner, N. W., Taplin, R. K., Thorman, M., Thornewell, P., Trent, P. T., Tserkovnyak, Y. I., van Berg, R., van de Water, R. G., Virtue, C. J., Waltham, C. E., Wang, J.-X., Wark, D. L., West, N., Wilhelmy, J. B., Wilkerson, J. F., Wilson, J., Wittich, P., Wouters, J. M., and Yeh, M. (2001). Measurement of the Rate of $\nu_e + d \rightarrow$ p + p + e$^-$ Interactions Produced by ^{8}B Solar Neutrinos at the Sudbury Neutrino Observatory. *Physical Review Letters*, 87(7):071301. 74

Alam, S., Albareti, F. D., Allende Prieto, C., Anders, F., Anderson, S. F., Anderton, T., Andrews, B. H., Armengaud, E., Aubourg, É., Bailey, S., and et al. (2015). The Eleventh and Twelfth Data Releases of the Sloan Digital Sky Survey: Final Data from SDSS-III. *ApJS*, 219:12. 49

Albrecht, A., Bernstein, G., Cahn, R., Freedman, W. L., Hewitt, J., Hu, W., Huth, J., Kamionkowski, M., Kolb, E. W., Knox, L., Mather, J. C., Staggs, S., and Suntzeff, N. B. (2006). Report of the Dark Energy Task Force. *ArXiv Astrophysics e-prints*. 47

Almeida, C., Baugh, C. M., Wake, D. A., Lacey, C. G., Benson, A. J., Bower, R. G., and Pimbblet, K. (2008). Luminous red galaxies in hierarchical cosmologies. *MNRAS*, 386:2145–2160. 44

Anderson, L., Aubourg, É., Bailey, S., Beutler, F., Bhardwaj, V., Blanton, M., Bolton, A. S., Brinkmann, J., Brownstein, J. R., Burden, A., Chuang, C.-H., Cuesta, A. J., Dawson, K. S., Eisenstein, D. J., Escoffier, S., Gunn, J. E., Guo, H., Ho, S., Honscheid, K., Howlett, C., Kirkby, D., Lupton, R. H., Manera, M., Maraston, C., McBride, C. K., Mena, O., Montesano, F., Nichol, R. C., Nuza, S. E., Olmstead, M. D., Padmanabhan, N., Palanque-Delabrouille, N., Parejko, J., Percival, W. J., Petitjean, P., Prada, F., Price-Whelan, A. M., Reid, B., Roe, N. A., Ross, A. J., Ross, N. P., Sabiu, C. G., Saito, S., Samushia, L., Sánchez, A. G., Schlegel, D. J., Schneider, D. P., Scoccola, C. G., Seo, H.-J., Skibba, R. A., Strauss, M. A., Swanson, M. E. C., Thomas, D., Tinker, J. L., Tojeiro, R., Magaña, M. V., Verde, L., Wake, D. A., Weaver, B. A., Weinberg, D. H., White, M., Xu, X., Yèche, C., Zehavi, I., and Zhao, G.-B. (2014a). The clustering of galaxies in the SDSS-III Baryon Oscillation Spectroscopic Survey: baryon acoustic oscillations in the Data Releases 10 and 11 Galaxy samples. *MNRAS*, 441:24–62. 42

Anderson, L., Aubourg, E., Bailey, S., Beutler, F., Bolton, A. S., Brinkmann, J., Brownstein, J. R., Chuang, C.-H., Cuesta, A. J., Dawson, K. S., Eisenstein, D. J., Ho, S., Honscheid, K., Kazin, E. A., Kirkby, D., Manera, M., McBride, C. K., Mena, O., Nichol, R. C., Olmstead, M. D., Padmanabhan,

N., Palanque-Delabrouille, N., Percival, W. J., Prada, F., Ross, A. J., Ross, N. P., Sánchez, A. G., Samushia, L., Schlegel, D. J., Schneider, D. P., Seo, H.-J., Strauss, M. A., Thomas, D., Tinker, J. L., Tojeiro, R., Verde, L., Wake, D., Weinberg, D. H., Xu, X., and Yeche, C. (2014b). The clustering of galaxies in the SDSS-III Baryon Oscillation Spectroscopic Survey: measuring D_A and H at z = 0.57 from the baryon acoustic peak in the Data Release 9 spectroscopic Galaxy sample. *MNRAS*, 439:83–101. xiii, 3, 11, 12, 49, 68

Angulo, R., Fasiello, M., Senatore, L., and Vlah, Z. (2015a). On the statistics of biased tracers in the Effective Field Theory of Large Scale Structures. *Journal of Cosmology and Astroparticle Physics (JCAP)*, 9:029. 19

Angulo, R. E., Foreman, S., Schmittfull, M., and Senatore, L. (2015b). The one-loop matter bispectrum in the Effective Field Theory of Large Scale Structures. *Journal of Cosmology and Astroparticle Physics (JCAP)*, 10:039. 19

Asorey, J., Crocce, M., and Gaztañaga, E. (2014). Redshift-space distortions from the cross-correlation of photometric populations. *MNRAS*, 445:2825–2835. 25

Asorey, J., Crocce, M., Gaztañaga, E., and Lewis, A. (2012). Recovering 3D clustering information with angular correlations. *MNRAS*, 427:1891–1902. 25, 28

Astier, P., Guy, J., Regnault, N., Pain, R., Aubourg, E., Balam, D., Basa, S., Carlberg, R. G., Fabbro, S., Fouchez, D., Hook, I. M., Howell, D. A., Lafoux, H., Neill, J. D., Palanque-Delabrouille, N., Perrett, K., Pritchet, C. J., Rich, J., Sullivan, M., Taillet, R., Aldering, G., Antilogus, P., Arsenijevic, V., Balland, C., Baumont, S., Bronder, J., Courtois, H., Ellis, R. S., Filiol, M., Gonçalves, A. C., Goobar, A., Guide, D., Hardin, D., Lusset, V., Lidman, C., McMahon, R., Mouchet, M., Mourao, A., Perlmutter, S., Ripoche, P., Tao, C., and Walton, N. (2006). The Supernova Legacy Survey: measurement of Ω_M, Ω and w from the first year data set. *A&A*, 447:31–48. 51

Baugh, C. M., Benson, A. J., Cole, S., Frenk, C. S., and Lacey, C. G. (1999). Modelling the evolution of galaxy clustering. *MNRAS*, 305:L21–L25. 36, 44

Bennett, C. L., Banday, A. J., Gorski, K. M., Hinshaw, G., Jackson, P., Keegstra, P., Kogut, A., Smoot, G. F., Wilkinson, D. T., and Wright, E. L.

(1996). Four-Year COBE DMR Cosmic Microwave Background Observations: Maps and Basic Results. *ApJ*, 464:L1. 3

Berlind, A. A. and Weinberg, D. H. (2002). The Halo Occupation Distribution: Toward an Empirical Determination of the Relation between Galaxies and Mass. *ApJ*, 575:587–616. 26

Betoule, M., Kessler, R., Guy, J., Mosher, J., Hardin, D., Biswas, R., Astier, P., El-Hage, P., Konig, M., Kuhlmann, S., Marriner, J., Pain, R., Regnault, N., Balland, C., Bassett, B. A., Brown, P. J., Campbell, H., Carlberg, R. G., Cellier-Holzem, F., Cinabro, D., Conley, A., D'Andrea, C. B., DePoy, D. L., Doi, M., Ellis, R. S., Fabbro, S., Filippenko, A. V., Foley, R. J., Frieman, J. A., Fouchez, D., Galbany, L., Goobar, A., Gupta, R. R., Hill, G. J., Hlozek, R., Hogan, C. J., Hook, I. M., Howell, D. A., Jha, S. W., Le Guillou, L., Leloudas, G., Lidman, C., Marshall, J. L., Möller, A., Mourão, A. M., Neveu, J., Nichol, R., Olmstead, M. D., Palanque-Delabrouille, N., Perlmutter, S., Prieto, J. L., Pritchet, C. J., Richmond, M., Riess, A. G., Ruhlmann-Kleider, V., Sako, M., Schahmaneche, K., Schneider, D. P., Smith, M., Sollerman, J., Sullivan, M., Walton, N. A., and Wheeler, C. J. (2014). Improved cosmological constraints from a joint analysis of the SDSS-II and SNLS supernova samples. *A&A*, 568:A22. 51

Beutler, F., Blake, C., Colless, M., Jones, D. H., Staveley-Smith, L., Campbell, L., Parker, Q., Saunders, W., and Watson, F. (2011). The 6dF Galaxy Survey: baryon acoustic oscillations and the local Hubble constant. *MNRAS*, 416:3017–3032. xiii, 12

Beutler, F., Saito, S., Brownstein, J. R., Chuang, C.-H., Cuesta, A. J., Percival, W. J., Ross, A. J., Ross, N. P., Schneider, D. P., Samushia, L., Sánchez, A. G., Seo, H.-J., Tinker, J. L., Wagner, C., and Weaver, B. A. (2014). The clustering of galaxies in the SDSS-III Baryon Oscillation Spectroscopic Survey: signs of neutrino mass in current cosmological data sets. *MNRAS*, 444:3501–3516. 49

Blake, C., Kazin, E. A., Beutler, F., Davis, T. M., Parkinson, D., Brough, S., Colless, M., Contreras, C., Couch, W., Croom, S., Croton, D., Drinkwater, M. J., Forster, K., Gilbank, D., Gladders, M., Glazebrook, K., Jelliffe, B., Jurek, R. J., Li, I.-H., Madore, B., Martin, D. C., Pimbblet, K., Poole, G. B., Pracy, M., Sharp, R., Wisnioski, E., Woods, D., Wyder, T. K., and Yee, H. K. C. (2011). The WiggleZ Dark Energy Survey: mapping the distance-redshift relation with baryon acoustic oscillations. *MNRAS*, 418:1707–1724. xiii, 3, 12

Blas, D., Lesgourgues, J., and Tram, T. (2011). The Cosmic Linear Anisotropy Solving System (CLASS). Part II: Approximation schemes. *Journal of Cosmology and Astroparticle Physics (JCAP)*, 7:034. 9, 55

Bolton, A. S., Schlegel, D. J., Aubourg, É., Bailey, S., Bhardwaj, V., Brownstein, J. R., Burles, S., Chen, Y.-M., Dawson, K., Eisenstein, D. J., Gunn, J. E., Knapp, G. R., Loomis, C. P., Lupton, R. H., Maraston, C., Muna, D., Myers, A. D., Olmstead, M. D., Padmanabhan, N., Pâris, I., Percival, W. J., Petitjean, P., Rockosi, C. M., Ross, N. P., Schneider, D. P., Shu, Y., Strauss, M. A., Thomas, D., Tremonti, C. A., Wake, D. A., Weaver, B. A., and Wood-Vasey, W. M. (2012). Spectral Classification and Redshift Measurement for the SDSS-III Baryon Oscillation Spectroscopic Survey. *AJ*, 144:144. 49

Bond, J. R. and Efstathiou, G. (1984). Cosmic background radiation anisotropies in universes dominated by nonbaryonic dark matter. *ApJ*, 285:L45–L48. 9

Campbell, H., D'Andrea, C. B., Nichol, R. C., Sako, M., Smith, M., Lampeitl, H., Olmstead, M. D., Bassett, B., Biswas, R., Brown, P., Cinabro, D., Dawson, K. S., Dilday, B., Foley, R. J., Frieman, J. A., Garnavich, P., Hlozek, R., Jha, S. W., Kuhlmann, S., Kunz, M., Marriner, J., Miquel, R., Richmond, M., Riess, A., Schneider, D. P., Sollerman, J., Taylor, M., and Zhao, G.-B. (2013). Cosmology with Photometrically Classified Type Ia Supernovae from the SDSS-II Supernova Survey. *ApJ*, 763:88. 51

Carrasco, J. J. M., Hertzberg, M. P., and Senatore, L. (2012). The effective field theory of cosmological large scale structures. *Journal of High Energy Physics*, 9:82. 19

Chan, K. C. and Scoccimarro, R. (2012). Halo sampling, local bias, and loop corrections. *Phys.Rev.D*, 86(10):103519. 22

Chan, K. C., Scoccimarro, R., and Sheth, R. K. (2012). Gravity and large-scale nonlocal bias. *Phys.Rev.D*, 85(8):083509. 22

Chevallier, M. and Polarski, D. (2001). Accelerating Universes with Scaling Dark Matter. *International Journal of Modern Physics D*, 10:213–223. 44, 71

Clerkin, L., Kirk, D., Lahav, O., Abdalla, F. B., and Gaztañaga, E. (2015). A prescription for galaxy biasing evolution as a nuisance parameter. *MNRAS*, 448:1389–1401. 62

Cohn, J. D. (2006). Power spectrum and correlation function errors: Poisson vs. Gaussian shot noise. *New Astronomy*, 11:226–239. 38

Cole, S., Fisher, K. B., and Weinberg, D. H. (1995). Constraints on Omega from the IRAS redshift surveys. *MNRAS*, 275:515–526. 21

Cole, S., Percival, W. J., Peacock, J. A., Norberg, P., Baugh, C. M., Frenk, C. S., Baldry, I., Bland-Hawthorn, J., Bridges, T., Cannon, R., Colless, M., Collins, C., Couch, W., Cross, N. J. G., Dalton, G., Eke, V. R., De Propris, R., Driver, S. P., Efstathiou, G., Ellis, R. S., Glazebrook, K., Jackson, C., Jenkins, A., Lahav, O., Lewis, I., Lumsden, S., Maddox, S., Madgwick, D., Peterson, B. A., Sutherland, W., and Taylor, K. (2005). The 2dF Galaxy Redshift Survey: power-spectrum analysis of the final data set and cosmological implications. *MNRAS*, 362:505–534. 3, 11

Colless, M., Dalton, G., Maddox, S., Sutherland, W., Norberg, P., Cole, S., Bland-Hawthorn, J., Bridges, T., Cannon, R., Collins, C., Couch, W., Cross, N., Deeley, K., De Propris, R., Driver, S. P., Efstathiou, G., Ellis, R. S., Frenk, C. S., Glazebrook, K., Jackson, C., Lahav, O., Lewis, I., Lumsden, S., Madgwick, D., Peacock, J. A., Peterson, B. A., Price, I., Seaborne, M., and Taylor, K. (2001). The 2dF Galaxy Redshift Survey: spectra and redshifts. *MNRAS*, 328:1039–1063. 2

Conley, A., Guy, J., Sullivan, M., Regnault, N., Astier, P., Balland, C., Basa, S., Carlberg, R. G., Fouchez, D., Hardin, D., Hook, I. M., Howell, D. A., Pain, R., Palanque-Delabrouille, N., Perrett, K. M., Pritchet, C. J., Rich, J., Ruhlmann-Kleider, V., Balam, D., Baumont, S., Ellis, R. S., Fabbro, S., Fakhouri, H. K., Fourmanoit, N., González-Gaitán, S., Graham, M. L., Hudson, M. J., Hsiao, E., Kronborg, T., Lidman, C., Mourao, A. M., Neill, J. D., Perlmutter, S., Ripoche, P., Suzuki, N., and Walker, E. S. (2011). Supernova Constraints and Systematic Uncertainties from the First Three Years of the Supernova Legacy Survey. *ApJS*, 192:1. 51

Crocce, M., Cabré, A., and Gaztañaga, E. (2011a). Modelling the angular correlation function and its full covariance in photometric galaxy surveys. *MNRAS*, 414:329–349. 25, 37

Crocce, M., Gaztañaga, E., Cabré, A., Carnero, A., and Sánchez, E. (2011b). Clustering of photometric luminous red galaxies - I. Growth of structure and baryon acoustic feature. *MNRAS*, 417:2577–2591. 25

Crocce, M. and Scoccimarro, R. (2006). Renormalized cosmological perturbation theory. *Phys.Rev.D*, 73(6):063519. 19, 20

Crocce, M. and Scoccimarro, R. (2008). Nonlinear evolution of baryon acoustic oscillations. *Phys.Rev.D*, 77(2):023533. 17

Crocce, M., Scoccimarro, R., and Bernardeau, F. (2012). MPTBREEZE: a fast renormalized perturbative scheme. *MNRAS*, 427:2537–2551. 21

Cuesta, A. J., Vargas-Magaña, M., Beutler, F., Bolton, A. S., Brownstein, J. R., Eisenstein, D. J., Gil-Marín, H., Ho, S., McBride, C. K., Maraston, C., Padmanabhan, N., Percival, W. J., Reid, B. A., Ross, A. J., Ross, N. P., Sánchez, A. G., Schlegel, D. J., Schneider, D. P., Thomas, D., Tinker, J., Tojeiro, R., Verde, L., and White, M. (2016). The clustering of galaxies in the SDSS-III Baryon Oscillation Spectroscopic Survey: baryon acoustic oscillations in the correlation function of LOWZ and CMASS galaxies in Data Release 12. *MNRAS*, 457:1770–1785. 49

Davis, M., Efstathiou, G., Frenk, C. S., and White, S. D. M. (1985). The evolution of large-scale structure in a universe dominated by cold dark matter. *ApJ*, 292:371–394. 26

Dawson, K. S., Schlegel, D. J., Ahn, C. P., Anderson, S. F., Aubourg, É., Bailey, S., Barkhouser, R. H., Bautista, J. E., Beifiori, A., Berlind, A. A., Bhardwaj, V., Bizyaev, D., Blake, C. H., Blanton, M. R., Blomqvist, M., Bolton, A. S., Borde, A., Bovy, J., Brandt, W. N., Brewington, H., Brinkmann, J., Brown, P. J., Brownstein, J. R., Bundy, K., Busca, N. G., Carithers, W., Carnero, A. R., Carr, M. A., Chen, Y., Comparat, J., Connolly, N., Cope, F., Croft, R. A. C., Cuesta, A. J., da Costa, L. N., Davenport, J. R. A., Delubac, T., de Putter, R., Dhital, S., Ealet, A., Ebelke, G. L., Eisenstein, D. J., Escoffier, S., Fan, X., Filiz Ak, N., Finley, H., Font-Ribera, A., Génova-Santos, R., Gunn, J. E., Guo, H., Haggard, D., Hall, P. B., Hamilton, J.-C., Harris, B., Harris, D. W., Ho, S., Hogg, D. W., Holder, D., Honscheid, K., Huehnerhoff, J., Jordan, B., Jordan, W. P., Kauffmann, G., Kazin, E. A., Kirkby, D., Klaene, M. A., Kneib, J.-P., Le Goff, J.-M., Lee, K.-G., Long, D. C., Loomis, C. P., Lundgren, B., Lupton, R. H., Maia, M. A. G., Makler, M., Malanushenko, E., Malanushenko, V., Mandelbaum, R., Manera, M., Maraston, C., Margala, D., Masters, K. L., McBride, C. K., McDonald, P., McGreer, I. D., McMahon, R. G., Mena, O., Miralda-Escudé, J., Montero-Dorta, A. D., Montesano, F., Muna, D., Myers, A. D., Naugle, T., Nichol, R. C., Noterdaeme, P., Nuza, S. E., Olmstead, M. D., Oravetz, A., Oravetz, D. J., Owen, R., Padmanabhan, N., Palanque-Delabrouille, N., Pan, K., Parejko, J. K., Pâris, I., Percival, W. J., Pérez-Fournon, I., Pérez-Ràfols, I., Petitjean, P., Pfaffenberger, R., Pforr, J., Pieri, M. M., Prada, F., Price-Whelan, A. M., Raddick, M. J., Rebolo, R., Rich, J., Richards,

G. T., Rockosi, C. M., Roe, N. A., Ross, A. J., Ross, N. P., Rossi, G., Rubiño-Martin, J. A., Samushia, L., Sánchez, A. G., Sayres, C., Schmidt, S. J., Schneider, D. P., Scóccola, C. G., Seo, H.-J., Shelden, A., Sheldon, E., Shen, Y., Shu, Y., Slosar, A., Smee, S. A., Snedden, S. A., Stauffer, F., Steele, O., Strauss, M. A., Streblyanska, A., Suzuki, N., Swanson, M. E. C., Tal, T., Tanaka, M., Thomas, D., Tinker, J. L., Tojeiro, R., Tremonti, C. A., Vargas Magaña, M., Verde, L., Viel, M., Wake, D. A., Watson, M., Weaver, B. A., Weinberg, D. H., Weiner, B. J., West, A. A., White, M., Wood-Vasey, W. M., Yeche, C., Zehavi, I., Zhao, G.-B., and Zheng, Z. (2013). The Baryon Oscillation Spectroscopic Survey of SDSS-III. *AJ*, 145:10. 3, 49

de Simoni, F., Sobreira, F., Carnero, A., Ross, A. J., Camacho, H. O., Rosenfeld, R., Lima, M., da Costa, L. A. N., and Maia, M. A. G. (2013). Large-scale analysis of the SDSS-III DR8 photometric luminous galaxies angular correlation function. *MNRAS*, 435:3017–3027. 25

Di Dio, E., Montanari, F., Durrer, R., and Lesgourgues, J. (2014). Cosmological parameter estimation with large scale structure observations. *Journal of Cosmology and Astroparticle Physics (JCAP)*, 1:042. 25, 28, 55

Dodelson, S. and Schneider, M. D. (2013). The effect of covariance estimator error on cosmological parameter constraints. *Phys.Rev.D*, 88(6):063537. 36

Drinkwater, M. J., Jurek, R. J., Blake, C., Woods, D., Pimbblet, K. A., Glazebrook, K., Sharp, R., Pracy, M. B., Brough, S., Colless, M., Couch, W. J., Croom, S. M., Davis, T. M., Forbes, D., Forster, K., Gilbank, D. G., Gladders, M., Jelliffe, B., Jones, N., Li, I.-H., Madore, B., Martin, D. C., Poole, G. B., Small, T., Wisnioski, E., Wyder, T., and Yee, H. K. C. (2010). The WiggleZ Dark Energy Survey: survey design and first data release. *MNRAS*, 401:1429–1452. 3

Einstein, A. (1916). Die Grundlage der allgemeinen Relativitätstheorie. *Annalen der Physik*, 354:769–822. 1

Eisenstein, D. J. and Hu, W. (1999). Power Spectra for Cold Dark Matter and Its Variants. *ApJ*, 511:5–15. 9

Eisenstein, D. J., Weinberg, D. H., Agol, E., Aihara, H., Allende Prieto, C., Anderson, S. F., Arns, J. A., Aubourg, É., Bailey, S., Balbinot, E., and et al. (2011). SDSS-III: Massive Spectroscopic Surveys of the Distant Universe, the Milky Way, and Extra-Solar Planetary Systems. *AJ*, 142:72. 49

Eisenstein, D. J., Zehavi, I., Hogg, D. W., Scoccimarro, R., Blanton, M. R., Nichol, R. C., Scranton, R., Seo, H.-J., Tegmark, M., Zheng, Z., Anderson, S. F., Annis, J., Bahcall, N., Brinkmann, J., Burles, S., Castander, F. J., Connolly, A., Csabai, I., Doi, M., Fukugita, M., Frieman, J. A., Glazebrook, K., Gunn, J. E., Hendry, J. S., Hennessy, G., Ivezić, Z., Kent, S., Knapp, G. R., Lin, H., Loh, Y.-S., Lupton, R. H., Margon, B., McKay, T. A., Meiksin, A., Munn, J. A., Pope, A., Richmond, M. W., Schlegel, D., Schneider, D. P., Shimasaku, K., Stoughton, C., Strauss, M. A., SubbaRao, M., Szalay, A. S., Szapudi, I., Tucker, D. L., Yanny, B., and York, D. G. (2005). Detection of the Baryon Acoustic Peak in the Large-Scale Correlation Function of SDSS Luminous Red Galaxies. *ApJ*, 633:560–574. 3, 11, 25

Fosalba, P., Crocce, M., Gaztañaga, E., and Castander, F. J. (2015). The MICE grand challenge lightcone simulation - I. Dark matter clustering. *MNRAS*, 448:2987–3000. 31

Frieman, J. A., Bassett, B., Becker, A., Choi, C., Cinabro, D., DeJongh, F., Depoy, D. L., Dilday, B., Doi, M., Garnavich, P. M., Hogan, C. J., Holtzman, J., Im, M., Jha, S., Kessler, R., Konishi, K., Lampeitl, H., Marriner, J., Marshall, J. L., McGinnis, D., Miknaitis, G., Nichol, R. C., Prieto, J. L., Riess, A. G., Richmond, M. W., Romani, R., Sako, M., Schneider, D. P., Smith, M., Takanashi, N., Tokita, K., van der Heyden, K., Yasuda, N., Zheng, C., Adelman-McCarthy, J., Annis, J., Assef, R. J., Barentine, J., Bender, R., Blandford, R. D., Boroski, W. N., Bremer, M., Brewington, H., Collins, C. A., Crotts, A., Dembicky, J., Eastman, J., Edge, A., Edmondson, E., Elson, E., Eyler, M. E., Filippenko, A. V., Foley, R. J., Frank, S., Goobar, A., Gueth, T., Gunn, J. E., Harvanek, M., Hopp, U., Ihara, Y., Ivezić, Ž., Kahn, S., Kaplan, J., Kent, S., Ketzeback, W., Kleinman, S. J., Kollatschny, W., Kron, R. G., Krzesiński, J., Lamenti, D., Leloudas, G., Lin, H., Long, D. C., Lucey, J., Lupton, R. H., Malanushenko, E., Malanushenko, V., McMillan, R. J., Mendez, J., Morgan, C. W., Morokuma, T., Nitta, A., Ostman, L., Pan, K., Rockosi, C. M., Romer, A. K., Ruiz-Lapuente, P., Saurage, G., Schlesinger, K., Snedden, S. A., Sollerman, J., Stoughton, C., Stritzinger, M., Subba Rao, M., Tucker, D., Vaisanen, P., Watson, L. C., Watters, S., Wheeler, J. C., Yanny, B., and York, D. (2008). The Sloan Digital Sky Survey-II Supernova Survey: Technical Summary. *AJ*, 135:338–347. 51

Fry, J. N. (1996). The Evolution of Bias. *ApJ*, 461:L65. xv, 41, 43, 52

Fukuda, Y., Hayakawa, T., Ichihara, E., Inoue, K., Ishihara, K., Ishino, H., Itow, Y., Kajita, T., Kameda, J., Kasuga, S., Kobayashi, K., Kobayashi,

Y., Koshio, Y., Miura, M., Nakahata, M., Nakayama, S., Okada, A., Okumura, K., Sakurai, N., Shiozawa, M., Suzuki, Y., Takeuchi, Y., Totsuka, Y., Yamada, S., Earl, M., Habig, A., Kearns, E., Messier, M. D., Scholberg, K., Stone, J. L., Sulak, L. R., Walter, C. W., Goldhaber, M., Barszczxak, T., Casper, D., Gajewski, W., Halverson, P. G., Hsu, J., Kropp, W. R., Price, L. R., Reines, F., Smy, M., Sobel, H. W., Vagins, M. R., Ganezer, K. S., Keig, W. E., Ellsworth, R. W., Tasaka, S., Flanagan, J. W., Kibayashi, A., Learned, J. G., Matsuno, S., Stenger, V. J., Takemori, D., Ishii, T., Kanzaki, J., Kobayashi, T., Mine, S., Nakamura, K., Nishikawa, K., Oyama, Y., Sakai, A., Sakuda, M., Sasaki, O., Echigo, S., Kohama, M., Suzuki, A. T., Haines, T. J., Blaufuss, E., Kim, B. K., Sanford, R., Svoboda, R., Chen, M. L., Conner, Z., Goodman, J. A., Sullivan, G. W., Hill, J., Jung, C. K., Martens, K., Mauger, C., McGrew, C., Sharkey, E., Viren, B., Yanagisawa, C., Doki, W., Miyano, K., Okazawa, H., Saji, C., Takahata, M., Nagashima, Y., Takita, M., Yamaguchi, T., Yoshida, M., Kim, S. B., Etoh, M., Fujita, K., Hasegawa, A., Hasegawa, T., Hatakeyama, S., Iwamoto, T., Koga, M., Maruyama, T., Ogawa, H., Shirai, J., Suzuki, A., Tsushima, F., Koshiba, M., Nemoto, M., Nishijima, K., Futagami, T., Hayato, Y., Kanaya, Y., Kaneyuki, K., Watanabe, Y., Kielczewska, D., Doyle, R. A., George, J. S., Stachyra, A. L., Wai, L. L., Wilkes, R. J., and Young, K. K. (1998). Evidence for Oscillation of Atmospheric Neutrinos. *Physical Review Letters*, 81:1562–1567. 74

Górski, K. M., Hivon, E., Banday, A. J., Wandelt, B. D., Hansen, F. K., Reinecke, M., and Bartelmann, M. (2005). HEALPix: A Framework for High-Resolution Discretization and Fast Analysis of Data Distributed on the Sphere. *ApJ*, 622:759–771. 124

Grieb, J. N., Sánchez, A. G., Salazar-Albornoz, S., and Dalla Vecchia, C. (2016). Gaussian covariance matrices for anisotropic galaxy clustering measurements. *MNRAS*, 457:1577–1592. xiii, 17, 18

Gunn, J. E., Siegmund, W. A., Mannery, E. J., Owen, R. E., Hull, C. L., Leger, R. F., Carey, L. N., Knapp, G. R., York, D. G., Boroski, W. N., Kent, S. M., Lupton, R. H., Rockosi, C. M., Evans, M. L., Waddell, P., Anderson, J. E., Annis, J., Barentine, J. C., Bartoszek, L. M., Bastian, S., Bracker, S. B., Brewington, H. J., Briegel, C. I., Brinkmann, J., Brown, Y. J., Carr, M. A., Czarapata, P. C., Drennan, C. C., Dombeck, T., Federwitz, G. R., Gillespie, B. A., Gonzales, C., Hansen, S. U., Harvanek, M., Hayes, J., Jordan, W., Kinney, E., Klaene, M., Kleinman, S. J., Kron, R. G., Kresinski, J., Lee, G., Limmongkol, S., Lindenmeyer, C. W., Long, D. C., Loomis, C. L., McGehee, P. M., Mantsch, P. M., Neilsen, Jr., E. H., Neswold, R. M., Newman, P. R.,

Nitta, A., Peoples, Jr., J., Pier, J. R., Prieto, P. S., Prosapio, A., Rivetta, C., Schneider, D. P., Snedden, S., and Wang, S.-i. (2006). The 2.5 m Telescope of the Sloan Digital Sky Survey. *AJ*, 131:2332–2359. 49

Guo, H., Zehavi, I., Zheng, Z., Weinberg, D. H., Berlind, A. A., Blanton, M., Chen, Y., Eisenstein, D. J., Ho, S., Kazin, E., Manera, M., Maraston, C., McBride, C. K., Nuza, S. E., Padmanabhan, N., Parejko, J. K., Percival, W. J., Ross, A. J., Ross, N. P., Samushia, L., Sánchez, A. G., Schlegel, D. J., Schneider, D. P., Skibba, R. A., Swanson, M. E. C., Tinker, J. L., Tojeiro, R., Wake, D. A., White, M., Bahcall, N. A., Bizyaev, D., Brewington, H., Bundy, K., da Costa, L. N. A., Ebelke, G., Malanushenko, E., Malanushenko, V., Oravetz, D., Rossi, G., Simmons, A., Snedden, S., Streblyanska, A., and Thomas, D. (2013). The Clustering of Galaxies in the SDSS-III Baryon Oscillation Spectroscopic Survey: Luminosity and Color Dependence and Redshift Evolution. *ApJ*, 767:122. 41

Hamilton, A. J. S. (1997). Towards optimal measurement of power spectra - II. A basis of positive, compact, statistically orthogonal kernels. *MNRAS*, 289:295–304. 17

Hamilton, A. J. S. (1998). Linear Redshift Distortions: a Review. In Hamilton, D., editor, *The Evolving Universe*, volume 231 of *Astrophysics and Space Science Library*, page 185. 16

Heitmann, K., Higdon, D., White, M., Habib, S., Williams, B. J., Lawrence, E., and Wagner, C. (2009). The Coyote Universe. II. Cosmological Models and Precision Emulation of the Nonlinear Matter Power Spectrum. *ApJ*, 705:156–174. 19

Heitmann, K., White, M., Wagner, C., Habib, S., and Higdon, D. (2010). The Coyote Universe. I. Precision Determination of the Nonlinear Matter Power Spectrum. *ApJ*, 715:104–121. 19

Hill, G. J., Gebhardt, K., Komatsu, E., Drory, N., MacQueen, P. J., Adams, J., Blanc, G. A., Koehler, R., Rafal, M., Roth, M. M., Kelz, A., Gronwall, C., Ciardullo, R., and Schneider, D. P. (2008). The Hobby-Eberly Telescope Dark Energy Experiment (HETDEX): Description and Early Pilot Survey Results. In Kodama, T., Yamada, T., and Aoki, K., editors, *Panoramic Views of Galaxy Formation and Evolution*, volume 399 of *Astronomical Society of the Pacific Conference Series*, page 115. 3

Hubble, E. (1929). A Relation between Distance and Radial Velocity among Extra-Galactic Nebulae. *Proceedings of the National Academy of Science*, 15:168–173. 1

Huchra, J., Davis, M., Latham, D., and Tonry, J. (1983). A survey of galaxy redshifts. IV - The data. *ApJS*, 52:89–119. 1

Hütsi, G. (2006). Acoustic oscillations in the SDSS DR4 luminous red galaxy sample power spectrum. *A&A*, 449:891–902. 3

Kaiser, N. (1987). Clustering in real space and in redshift space. *MNRAS*, 227:1–21. 15, 16

Kauffmann, G., Colberg, J. M., Diaferio, A., and White, S. D. M. (1999). Clustering of galaxies in a hierarchical universe - II. Evolution to high redshift. *MNRAS*, 307:529–536. 36, 44

Kazin, E. A., Koda, J., Blake, C., Padmanabhan, N., Brough, S., Colless, M., Contreras, C., Couch, W., Croom, S., Croton, D. J., Davis, T. M., Drinkwater, M. J., Forster, K., Gilbank, D., Gladders, M., Glazebrook, K., Jelliffe, B., Jurek, R. J., Li, I.-h., Madore, B., Martin, D. C., Pimbblet, K., Poole, G. B., Pracy, M., Sharp, R., Wisnioski, E., Woods, D., Wyder, T. K., and Yee, H. K. C. (2014). The WiggleZ Dark Energy Survey: improved distance measurements to z = 1 with reconstruction of the baryonic acoustic feature. *MNRAS*, 441:3524–3542. xiii, 12

Kazin, E. A., Sánchez, A. G., and Blanton, M. R. (2012). Improving measurements of H(z) and D$_A$ (z) by analysing clustering anisotropies. *MNRAS*, 419:3223–3243. xiii, 14

Kessler, R., Becker, A. C., Cinabro, D., Vanderplas, J., Frieman, J. A., Marriner, J., Davis, T. M., Dilday, B., Holtzman, J., Jha, S. W., Lampeitl, H., Sako, M., Smith, M., Zheng, C., Nichol, R. C., Bassett, B., Bender, R., Depoy, D. L., Doi, M., Elson, E., Filippenko, A. V., Foley, R. J., Garnavich, P. M., Hopp, U., Ihara, Y., Ketzeback, W., Kollatschny, W., Konishi, K., Marshall, J. L., McMillan, R. J., Miknaitis, G., Morokuma, T., Mörtsell, E., Pan, K., Prieto, J. L., Richmond, M. W., Riess, A. G., Romani, R., Schneider, D. P., Sollerman, J., Takanashi, N., Tokita, K., van der Heyden, K., Wheeler, J. C., Yasuda, N., and York, D. (2009). First-Year Sloan Digital Sky Survey-II Supernova Results: Hubble Diagram and Cosmological Parameters. *ApJS*, 185:32–84. 51

Kitaura, F.-S., Rodríguez-Torres, S., Chuang, C.-H., Zhao, C., Prada, F., Gil-Marín, H., Guo, H., Yepes, G., Klypin, A., Scóccola, C. G., Tinker, J., McBride, C., Reid, B., Sánchez, A. G., Salazar-Albornoz, S., Grieb, J. N., Vargas-Magana, M., Cuesta, A. J., Neyrinck, M., Beutler, F., Comparat, J., Percival, W. J., and Ross, A. (2016). The clustering of galaxies in the SDSS-III Baryon Oscillation Spectroscopic Survey: mock galaxy catalogues for the BOSS Final Data Release. *MNRAS*, 456:4156–4173. 50

Komatsu, E., Smith, K. M., Dunkley, J., Bennett, C. L., Gold, B., Hinshaw, G., Jarosik, N., Larson, D., Nolta, M. R., Page, L., Spergel, D. N., Halpern, M., Hill, R. S., Kogut, A., Limon, M., Meyer, S. S., Odegard, N., Tucker, G. S., Weiland, J. L., Wollack, E., and Wright, E. L. (2011). Seven-year Wilkinson Microwave Anisotropy Probe (WMAP) Observations: Cosmological Interpretation. *ApJS*, 192:18. 41

Landy, S. D. and Szalay, A. S. (1993). Bias and variance of angular correlation functions. *ApJ*, 412:64–71. 28, 49

Laureijs, R., Amiaux, J., Arduini, S., Auguères, J. ., Brinchmann, J., Cole, R., Cropper, M., Dabin, C., Duvet, L., Ealet, A., and et al. (2011). Euclid Definition Study Report. *ArXiv e-prints*. 3

Leauthaud, A., Bundy, K., Saito, S., Tinker, J., Maraston, C., Tojeiro, R., Huang, S., Brownstein, J. R., Schneider, D. P., and Thomas, D. (2016). The Stripe 82 Massive Galaxy Project - II. Stellar mass completeness of spectroscopic galaxy samples from the Baryon Oscillation Spectroscopic Survey. *MNRAS*, 457:4021–4037. 52

Levi, M., Bebek, C., Beers, T., Blum, R., Cahn, R., Eisenstein, D., Flaugher, B., Honscheid, K., Kron, R., Lahav, O., McDonald, P., Roe, N., Schlegel, D., and representing the DESI collaboration (2013). The DESI Experiment, a whitepaper for Snowmass 2013. *ArXiv e-prints*. 3

Lewis, A. and Bridle, S. (2002). Cosmological parameters from CMB and other data: A Monte Carlo approach. *Phys.Rev.D*, 66(10):103511. 66

Lewis, A., Challinor, A., and Lasenby, A. (2000). Efficient Computation of Cosmic Microwave Background Anisotropies in Closed Friedmann-Robertson-Walker Models. *ApJ*, 538:473–476. 9, 41

Linder, E. V. (2003). Exploring the Expansion History of the Universe. *Physical Review Letters*, 90(9):091301. 44, 71

Linder, E. V. (2005). Cosmic growth history and expansion history. *Phys.Rev.D*, 72(4):043529. 59, 77

Liske, J. (2000). On the cosmological distance and redshift between any two objects. *MNRAS*, 319:557–561. 33

LSST Science Collaboration, Abell, P. A., Allison, J., Anderson, S. F., Andrew, J. R., Angel, J. R. P., Armus, L., Arnett, D., Asztalos, S. J., Axelrod, T. S., and et al. (2009). LSST Science Book, Version 2.0. *ArXiv e-prints*. 3

McBride, C., Berlind, A., Scoccimarro, R., Wechsler, R., Busha, M., Gardner, J., and van den Bosch, F. (2009). LasDamas Mock Galaxy Catalogs for SDSS. In *American Astronomical Society Meeting Abstracts #213*, volume 41 of *Bulletin of the American Astronomical Society*, page 253. xiii, 14, 26

Miller, A. D., Caldwell, R., Devlin, M. J., Dorwart, W. B., Herbig, T., Nolta, M. R., Page, L. A., Puchalla, J., Torbet, E., and Tran, H. T. (1999). A Measurement of the Angular Power Spectrum of the Cosmic Microwave Background from L = 100 to 400. *ApJ*, 524:L1–L4. 3

Montesano, F., Sánchez, A. G., and Phleps, S. (2010). A new model for the full shape of the large-scale power spectrum. *MNRAS*, 408:2397–2412. 21

Montesano, F., Sánchez, A. G., and Phleps, S. (2012). Cosmological implications from the full shape of the large-scale power spectrum of the SDSS DR7 luminous red galaxies. *MNRAS*, 421:2656–2681. 21, 26

Nock, K., Percival, W. J., and Ross, A. J. (2010). The effect of redshift-space distortions on projected two-point clustering measurements. *MNRAS*, 407:520–532. 31

Padmanabhan, N., Schlegel, D. J., Seljak, U., Makarov, A., Bahcall, N. A., Blanton, M. R., Brinkmann, J., Eisenstein, D. J., Finkbeiner, D. P., Gunn, J. E., Hogg, D. W., Ivezić, Ž., Knapp, G. R., Loveday, J., Lupton, R. H., Nichol, R. C., Schneider, D. P., Strauss, M. A., Tegmark, M., and York, D. G. (2007). The clustering of luminous red galaxies in the Sloan Digital Sky Survey imaging data. *MNRAS*, 378:852–872. 25

Papoulis, A. (1984). *Probability, random variables and stochastic processes.* McGraw-Hill. 85

Park, C., Vogeley, M. S., Geller, M. J., and Huchra, J. P. (1994). Power spectrum, correlation function, and tests for luminosity bias in the CfA redshift survey. *ApJ*, 431:569–585. 21

Peacock, J. A. (1999). *Cosmological Physics*. Cambridge University Press. 33

Peacock, J. A. and Smith, R. E. (2000). Halo occupation numbers and galaxy bias. *MNRAS*, 318:1144–1156. 12, 26

Peebles, P. J. E. (1973). Statistical Analysis of Catalogs of Extragalactic Objects. I. Theory. *ApJ*, 185:413–440. 31

Peebles, P. J. E. (1980). *The large-scale structure of the universe*. Princeton University Press. 90

Peebles, P. J. E. and Yu, J. T. (1970). Primeval Adiabatic Perturbation in an Expanding Universe. *ApJ*, 162:815. 3

Penzias, A. A. and Wilson, R. W. (1965). A Measurement of Excess Antenna Temperature at 4080 Mc/s. *ApJ*, 142:419–421. 1

Percival, W. J., Nichol, R. C., Eisenstein, D. J., Weinberg, D. H., Fukugita, M., Pope, A. C., Schneider, D. P., Szalay, A. S., Vogeley, M. S., Zehavi, I., Bahcall, N. A., Brinkmann, J., Connolly, A. J., Loveday, J., and Meiksin, A. (2007). Measuring the Matter Density Using Baryon Oscillations in the SDSS. *ApJ*, 657:51–55. 3

Percival, W. J., Ross, A. J., Sánchez, A. G., Samushia, L., Burden, A., Crittenden, R., Cuesta, A. J., Magana, M. V., Manera, M., Beutler, F., Chuang, C.-H., Eisenstein, D. J., Ho, S., McBride, C. K., Montesano, F., Padmanabhan, N., Reid, B., Saito, S., Schneider, D. P., Seo, H.-J., Tojeiro, R., and Weaver, B. A. (2014). The clustering of Galaxies in the SDSS-III Baryon Oscillation Spectroscopic Survey: including covariance matrix errors. *MNRAS*, 439:2531–2541. 36

Perlmutter, S., Aldering, G., della Valle, M., Deustua, S., Ellis, R. S., Fabbro, S., Fruchter, A., Goldhaber, G., Groom, D. E., Hook, I. M., Kim, A. G., Kim, M. Y., Knop, R. A., Lidman, C., McMahon, R. G., Nugent, P., Pain, R., Panagia, N., Pennypacker, C. R., Ruiz-Lapuente, P., Schaefer, B., and Walton, N. (1998). Discovery of a supernova explosion at half the age of the universe. *Nature*, 391:51. 1

Planck Collaboration XIII (2015). Planck 2015 results. XIII. Cosmological parameters. *ArXiv e-prints*. 8, 50, 51

Planck Collaboration XVI (2014). Planck 2013 results. XVI. Cosmological parameters. *A&A*, 571:A16. xiii, 12, 41

Reid, B., Ho, S., Padmanabhan, N., Percival, W. J., Tinker, J., Tojeiro, R., White, M., Eisenstein, D. J., Maraston, C., Ross, A. J., Sánchez, A. G., Schlegel, D., Sheldon, E., Strauss, M. A., Thomas, D., Wake, D., Beutler, F., Bizyaev, D., Bolton, A. S., Brownstein, J. R., Chuang, C.-H., Dawson, K., Harding, P., Kitaura, F.-S., Leauthaud, A., Masters, K., McBride, C. K., More, S., Olmstead, M. D., Oravetz, D., Nuza, S. E., Pan, K., Parejko, J., Pforr, J., Prada, F., Rodríguez-Torres, S., Salazar-Albornoz, S., Samushia, L., Schneider, D. P., Scóccola, C. G., Simmons, A., and Vargas-Magana, M. (2016). SDSS-III Baryon Oscillation Spectroscopic Survey Data Release 12: galaxy target selection and large-scale structure catalogues. *MNRAS*, 455:1553–1573. 49

Reid, B. A., Percival, W. J., Eisenstein, D. J., Verde, L., Spergel, D. N., Skibba, R. A., Bahcall, N. A., Budavari, T., Frieman, J. A., Fukugita, M., Gott, J. R., Gunn, J. E., Ivezić, Ž., Knapp, G. R., Kron, R. G., Lupton, R. H., McKay, T. A., Meiksin, A., Nichol, R. C., Pope, A. C., Schlegel, D. J., Schneider, D. P., Stoughton, C., Strauss, M. A., Szalay, A. S., Tegmark, M., Vogeley, M. S., Weinberg, D. H., York, D. G., and Zehavi, I. (2010). Cosmological constraints from the clustering of the Sloan Digital Sky Survey DR7 luminous red galaxies. *MNRAS*, 404:60–85. 3, 49

Reid, B. A., Seo, H.-J., Leauthaud, A., Tinker, J. L., and White, M. (2014). A 2.5 per cent measurement of the growth rate from small-scale redshift space clustering of SDSS-III CMASS galaxies. *MNRAS*, 444:476–502. 52, 63

Riess, A. G., Filippenko, A. V., Challis, P., Clocchiatti, A., Diercks, A., Garnavich, P. M., Gilliland, R. L., Hogan, C. J., Jha, S., Kirshner, R. P., Leibundgut, B., Phillips, M. M., Reiss, D., Schmidt, B. P., Schommer, R. A., Smith, R. C., Spyromilio, J., Stubbs, C., Suntzeff, N. B., and Tonry, J. (1998). Observational Evidence from Supernovae for an Accelerating Universe and a Cosmological Constant. *AJ*, 116:1009–1038. 1

Riess, A. G., Strolger, L.-G., Casertano, S., Ferguson, H. C., Mobasher, B., Gold, B., Challis, P. J., Filippenko, A. V., Jha, S., Li, W., Tonry, J., Foley, R., Kirshner, R. P., Dickinson, M., MacDonald, E., Eisenstein, D., Livio, M., Younger, J., Xu, C., Dahlén, T., and Stern, D. (2007). New Hubble Space Telescope Discoveries of Type Ia Supernovae at z >= 1: Narrowing Constraints on the Early Behavior of Dark Energy. *ApJ*, 659:98–121. 51

Ripley, B. D. (1981). *Spatial statistics*. Wiley. 85

Ross, A. J., Percival, W. J., Crocce, M., Cabré, A., and Gaztañaga, E. (2011).
   Measuring redshift-space distortions using photometric surveys. *MNRAS*,
   415:2193–2204. 25, 31

Saito, S., Leauthaud, A., Hearin, A. P., Bundy, K., Zentner, A. R., Behroozi,
   P. S., Reid, B. A., Sinha, M., Coupon, J., Tinker, J. L., White, M., and
   Schneider, D. P. (2015). Connecting Massive Galaxies to Dark Matter Halos
   in BOSS. I: Is Galaxy Color a Stochastic Process in High Mass Halos? *ArXiv
   e-prints*. 52, 62, 63

Salazar-Albornoz, S., Sánchez, A. G., Padilla, N. D., and Baugh, C. M. (2014).
   Clustering tomography: measuring cosmological distances through angular
   clustering in thin redshift shells. *MNRAS*, 443:3612–3623. 25, 26

Samushia, L., Reid, B. A., White, M., Percival, W. J., Cuesta, A. J., Lom-
   briser, L., Manera, M., Nichol, R. C., Schneider, D. P., Bizyaev, D., Brew-
   ington, H., Malanushenko, E., Malanushenko, V., Oravetz, D., Pan, K.,
   Simmons, A., Shelden, A., Snedden, S., Tinker, J. L., Weaver, B. A., York,
   D. G., and Zhao, G.-B. (2013). The clustering of galaxies in the SDSS-
   III DR9 Baryon Oscillation Spectroscopic Survey: testing deviations from
   Λ and general relativity using anisotropic clustering of galaxies. *MNRAS*,
   429:1514–1528. 3

Samushia, L., Reid, B. A., White, M., Percival, W. J., Cuesta, A. J., Zhao,
   G.-B., Ross, A. J., Manera, M., Aubourg, É., Beutler, F., Brinkmann, J.,
   Brownstein, J. R., Dawson, K. S., Eisenstein, D. J., Ho, S., Honscheid,
   K., Maraston, C., Montesano, F., Nichol, R. C., Roe, N. A., Ross, N. P.,
   Sánchez, A. G., Schlegel, D. J., Schneider, D. P., Streblyanska, A., Thomas,
   D., Tinker, J. L., Wake, D. A., Weaver, B. A., and Zehavi, I. (2014). The
   clustering of galaxies in the SDSS-III Baryon Oscillation Spectroscopic Sur-
   vey: measuring growth rate and geometry with anisotropic clustering. *MN-
   RAS*, 439:3504–3519. 49

Sánchez, A. G., Baugh, C. M., and Angulo, R. E. (2008). What is the best
   way to measure baryonic acoustic oscillations? *MNRAS*, 390:1470–1490. 21,
   38

Sánchez, A. G., Crocce, M., Cabré, A., Baugh, C. M., and Gaztañaga, E.
   (2009). Cosmological parameter constraints from SDSS luminous red galax-
   ies: a new treatment of large-scale clustering. *MNRAS*, 400:1643–1664. 3,
   21, 25

Sánchez, A. G., Kazin, E. A., Beutler, F., Chuang, C.-H., Cuesta, A. J., Eisenstein, D. J., Manera, M., Montesano, F., Nichol, R. C., Padmanabhan, N., Percival, W., Prada, F., Ross, A. J., Schlegel, D. J., Tinker, J., Tojeiro, R., Weinberg, D. H., Xu, X., Brinkmann, J., Brownstein, J. R., Schneider, D. P., and Thomas, D. (2013). The clustering of galaxies in the SDSS-III Baryon Oscillation Spectroscopic Survey: cosmological constraints from the full shape of the clustering wedges. *MNRAS*, 433:1202–1222. 3, 21, 49, 68

Sánchez, A. G., Montesano, F., Kazin, E. A., Aubourg, E., Beutler, F., Brinkmann, J., Brownstein, J. R., Cuesta, A. J., Dawson, K. S., Eisenstein, D. J., Ho, S., Honscheid, K., Manera, M., Maraston, C., McBride, C. K., Percival, W. J., Ross, A. J., Samushia, L., Schlegel, D. J., Schneider, D. P., Skibba, R., Thomas, D., Tinker, J. L., Tojeiro, R., Wake, D. A., Weaver, B. A., White, M., and Zehavi, I. (2014). The clustering of galaxies in the SDSS-III Baryon Oscillation Spectroscopic Survey: cosmological implications of the full shape of the clustering wedges in the data release 10 and 11 galaxy samples. *MNRAS*, 440:2692–2713. 3, 21, 49

Sánchez, A. G., Scóccola, C. G., Ross, A. J., Percival, W., Manera, M., Montesano, F., Mazzalay, X., Cuesta, A. J., Eisenstein, D. J., Kazin, E., McBride, C. K., Mehta, K., Montero-Dorta, A. D., Padmanabhan, N., Prada, F., Rubiño-Martín, J. A., Tojeiro, R., Xu, X., Magaña, M. V., Aubourg, E., Bahcall, N. A., Bailey, S., Bizyaev, D., Bolton, A. S., Brewington, H., Brinkmann, J., Brownstein, J. R., Gott, J. R., Hamilton, J. C., Ho, S., Honscheid, K., Labatie, A., Malanushenko, E., Malanushenko, V., Maraston, C., Muna, D., Nichol, R. C., Oravetz, D., Pan, K., Ross, N. P., Roe, N. A., Reid, B. A., Schlegel, D. J., Shelden, A., Schneider, D. P., Simmons, A., Skibba, R., Snedden, S., Thomas, D., Tinker, J., Wake, D. A., Weaver, B. A., Weinberg, D. H., White, M., Zehavi, I., and Zhao, G. (2012). The clustering of galaxies in the SDSS-III Baryon Oscillation Spectroscopic Survey: cosmological implications of the large-scale two-point correlation function. *MNRAS*, 425:415–437. 21

Sánchez, E., Carnero, A., García-Bellido, J., Gaztañaga, E., de Simoni, F., Crocce, M., Cabré, A., Fosalba, P., and Alonso, D. (2011). Tracing the sound horizon scale with photometric redshift surveys. *MNRAS*, 411:277–288. 25

Scherrer, R. J. and Bertschinger, E. (1991). Statistics of primordial density perturbations from discrete seed masses. *ApJ*, 381:349–360. 12

Schneider, A. and Teyssier, R. (2015). A new method to quantify the effects of baryons on the matter power spectrum. *Journal of Cosmology and Astroparticle Physics (JCAP)*, 12:049. 24

Seljak, U. (2000). Analytic model for galaxy and dark matter clustering. *MNRAS*, 318:203–213. 12

Smee, S. A., Gunn, J. E., Uomoto, A., Roe, N., Schlegel, D., Rockosi, C. M., Carr, M. A., Leger, F., Dawson, K. S., Olmstead, M. D., Brinkmann, J., Owen, R., Barkhouser, R. H., Honscheid, K., Harding, P., Long, D., Lupton, R. H., Loomis, C., Anderson, L., Annis, J., Bernardi, M., Bhardwaj, V., Bizyaev, D., Bolton, A. S., Brewington, H., Briggs, J. W., Burles, S., Burns, J. G., Castander, F. J., Connolly, A., Davenport, J. R. A., Ebelke, G., Epps, H., Feldman, P. D., Friedman, S. D., Frieman, J., Heckman, T., Hull, C. L., Knapp, G. R., Lawrence, D. M., Loveday, J., Mannery, E. J., Malanushenko, E., Malanushenko, V., Merrelli, A. J., Muna, D., Newman, P. R., Nichol, R. C., Oravetz, D., Pan, K., Pope, A. C., Ricketts, P. G., Shelden, A., Sandford, D., Siegmund, W., Simmons, A., Smith, D. S., Snedden, S., Schneider, D. P., SubbaRao, M., Tremonti, C., Waddell, P., and York, D. G. (2013). The Multi-object, Fiber-fed Spectrographs for the Sloan Digital Sky Survey and the Baryon Oscillation Spectroscopic Survey. *AJ*, 146:32. 49

Smith, R. E., Peacock, J. A., Jenkins, A., White, S. D. M., Frenk, C. S., Pearce, F. R., Thomas, P. A., Efstathiou, G., and Couchman, H. M. P. (2003). Stable clustering, the halo model and non-linear cosmological power spectra. *MNRAS*, 341:1311–1332. 19

Smith, R. E., Scoccimarro, R., and Sheth, R. K. (2008). Motion of the acoustic peak in the correlation function. *Phys.Rev.D*, 77(4):043525. 38

Spergel, D. N., Bean, R., Doré, O., Nolta, M. R., Bennett, C. L., Dunkley, J., Hinshaw, G., Jarosik, N., Komatsu, E., Page, L., Peiris, H. V., Verde, L., Halpern, M., Hill, R. S., Kogut, A., Limon, M., Meyer, S. S., Odegard, N., Tucker, G. S., Weiland, J. L., Wollack, E., and Wright, E. L. (2007). Three-Year Wilkinson Microwave Anisotropy Probe (WMAP) Observations: Implications for Cosmology. *ApJS*, 170:377–408. 3

Sullivan, M., Guy, J., Conley, A., Regnault, N., Astier, P., Balland, C., Basa, S., Carlberg, R. G., Fouchez, D., Hardin, D., Hook, I. M., Howell, D. A., Pain, R., Palanque-Delabrouille, N., Perrett, K. M., Pritchet, C. J., Rich, J., Ruhlmann-Kleider, V., Balam, D., Baumont, S., Ellis, R. S., Fabbro, S., Fakhouri, H. K., Fourmanoit, N., González-Gaitán, S., Graham, M. L.,

Hudson, M. J., Hsiao, E., Kronborg, T., Lidman, C., Mourao, A. M., Neill, J. D., Perlmutter, S., Ripoche, P., Suzuki, N., and Walker, E. S. (2011). SNLS3: Constraints on Dark Energy Combining the Supernova Legacy Survey Three-year Data with Other Probes. *ApJ*, 737:102. 51

Suzuki, N., Rubin, D., Lidman, C., Aldering, G., Amanullah, R., Barbary, K., Barrientos, L. F., Botyanszki, J., Brodwin, M., Connolly, N., Dawson, K. S., Dey, A., Doi, M., Donahue, M., Deustua, S., Eisenhardt, P., Ellingson, E., Faccioli, L., Fadeyev, V., Fakhouri, H. K., Fruchter, A. S., Gilbank, D. G., Gladders, M. D., Goldhaber, G., Gonzalez, A. H., Goobar, A., Gude, A., Hattori, T., Hoekstra, H., Hsiao, E., Huang, X., Ihara, Y., Jee, M. J., Johnston, D., Kashikawa, N., Koester, B., Konishi, K., Kowalski, M., Linder, E. V., Lubin, L., Melbourne, J., Meyers, J., Morokuma, T., Munshi, F., Mullis, C., Oda, T., Panagia, N., Perlmutter, S., Postman, M., Pritchard, T., Rhodes, J., Ripoche, P., Rosati, P., Schlegel, D. J., Spadafora, A., Stanford, S. A., Stanishev, V., Stern, D., Strovink, M., Takanashi, N., Tokita, K., Wagner, M., Wang, L., Yasuda, N., Yee, H. K. C., and Supernova Cosmology Project, T. (2012). The Hubble Space Telescope Cluster Supernova Survey. V. Improving the Dark-energy Constraints above z > 1 and Building an Early-type-hosted Supernova Sample. *ApJ*, 746:85. 51

Taylor, A. and Joachimi, B. (2014). Estimating cosmological parameter covariance. *MNRAS*, 442:2728–2738. 36

Taylor, A., Joachimi, B., and Kitching, T. (2013). Putting the precision in precision cosmology: How accurate should your data covariance matrix be? *MNRAS*, 432:1928–1946. 36

The Dark Energy Survey Collaboration (2005). The Dark Energy Survey. *ArXiv Astrophysics e-prints*. 3

Torbet, E., Devlin, M. J., Dorwart, W. B., Herbig, T., Miller, A. D., Nolta, M. R., Page, L., Puchalla, J., and Tran, H. T. (1999). A Measurement of the Angular Power Spectrum of the Microwave Background Made from the High Chilean Andes. *ApJ*, 521:L79–L82. 3

Wang, Y. (2008). Figure of merit for dark energy constraints from current observational data. *Phys.Rev.D*, 77(12):123525. 47

Wang, Y. and Wang, S. (2013). Distance priors from Planck and dark energy constraints from current data. *Phys.Rev.D*, 88(4):043522. 42

York, D. G., Adelman, J., Anderson, Jr., J. E., Anderson, S. F., Annis, J., Bahcall, N. A., Bakken, J. A., Barkhouser, R., Bastian, S., Berman, E., Boroski, W. N., Bracker, S., Briegel, C., Briggs, J. W., Brinkmann, J., Brunner, R., Burles, S., Carey, L., Carr, M. A., Castander, F. J., Chen, B., Colestock, P. L., Connolly, A. J., Crocker, J. H., Csabai, I., Czarapata, P. C., Davis, J. E., Doi, M., Dombeck, T., Eisenstein, D., Ellman, N., Elms, B. R., Evans, M. L., Fan, X., Federwitz, G. R., Fiscelli, L., Friedman, S., Frieman, J. A., Fukugita, M., Gillespie, B., Gunn, J. E., Gurbani, V. K., de Haas, E., Haldeman, M., Harris, F. H., Hayes, J., Heckman, T. M., Hennessy, G. S., Hindsley, R. B., Holm, S., Holmgren, D. J., Huang, C.-h., Hull, C., Husby, D., Ichikawa, S.-I., Ichikawa, T., Ivezić, Ž., Kent, S., Kim, R. S. J., Kinney, E., Klaene, M., Kleinman, A. N., Kleinman, S., Knapp, G. R., Korienek, J., Kron, R. G., Kunszt, P. Z., Lamb, D. Q., Lee, B., Leger, R. F., Limmongkol, S., Lindenmeyer, C., Long, D. C., Loomis, C., Loveday, J., Lucinio, R., Lupton, R. H., MacKinnon, B., Mannery, E. J., Mantsch, P. M., Margon, B., McGehee, P., McKay, T. A., Meiksin, A., Merelli, A., Monet, D. G., Munn, J. A., Narayanan, V. K., Nash, T., Neilsen, E., Neswold, R., Newberg, H. J., Nichol, R. C., Nicinski, T., Nonino, M., Okada, N., Okamura, S., Ostriker, J. P., Owen, R., Pauls, A. G., Peoples, J., Peterson, R. L., Petravick, D., Pier, J. R., Pope, A., Pordes, R., Prosapio, A., Rechenmacher, R., Quinn, T. R., Richards, G. T., Richmond, M. W., Rivetta, C. H., Rockosi, C. M., Ruthmansdorfer, K., Sandford, D., Schlegel, D. J., Schneider, D. P., Sekiguchi, M., Sergey, G., Shimasaku, K., Siegmund, W. A., Smee, S., Smith, J. A., Snedden, S., Stone, R., Stoughton, C., Strauss, M. A., Stubbs, C., SubbaRao, M., Szalay, A. S., Szapudi, I., Szokoly, G. P., Thakar, A. R., Tremonti, C., Tucker, D. L., Uomoto, A., Vanden Berk, D., Vogeley, M. S., Waddell, P., Wang, S.-i., Watanabe, M., Weinberg, D. H., Yanny, B., Yasuda, N., and SDSS Collaboration (2000). The Sloan Digital Sky Survey: Technical Summary. *AJ*, 120:1579–1587. 2

Acknowledgements

I would like to acknowledge those people along the road, those that helped to shape who I am today, or even those simply making things happen around me. However, it is absolutely impossible that I can fit (or remember) each person that has influenced this work. So, with the certainty of being a vastly incomplete list, I would like to thank Alessandro, Carlton, Daniel, Fabrizzio, Francesco, Jan, Jiamin, Manuel, Martha, Michael, Nelson, Nicolás, Ricardo, Rodrigo, and the OPINAS group at MPE. I would like to particularly thank my family, always present being more that 12000 km away; also Ximena and especially Ariel... it is hard not to fall short expressing my gratitude to Ariel. But, above all, I would like to thank Tatiana and Javiera, truly essential parts of absolutely everithing, I mean, **everything!**